Low-dimensional systems under extreme pressure conditions : environment and stability

Riccardo Galafassi

To cite this version:

Riccardo Galafassi. Low-dimensional systems under extreme pressure conditions : environment and stability. Physics [physics]. Université Claude Bernard - Lyon I, 2023. English. NNT : 2023LYO10145 . tel-04614541

HAL Id: tel-04614541
https://theses.hal.science/tel-04614541

Submitted on 17 Jun 2024

THÈSE de DOCTORAT DE
L'UNIVERSITÉ CLAUDE BERNARD LYON 1

École Doctorale 52
Physique et Astrophysique

Discipline : Physique

Soutenue publiquement le 22/09/2023, par:
Riccardo Galafassi

Low-dimensional systems under extreme pressure conditions: environment and stability

---

Devant le jury composé de :

Alvarez, Laurent, Maître de Conférences, Université de Montpellier	Rapporteur
Bendiab, Nedjma, Professeure, Université Grenoble Alpes	Rapporteure
Dunstan, David, Professeur, Queen Mary University of London	Examinateur
Gomes de Souza Filho, Antonio, Professeur, Universidade Federal do Ceará	Examinateur
Journet, Catherine, Professeure, Université Lyon 1	Présidente

San Miguel, Alfonso, Professeur, Université Lyon 1	Directeur de thèse
Vialla, Fabien, Maître de Conférences, Université Lyon 1	Co-directeur de thèse
Berthelot, Alice, Maître de Conférences, Université Lyon 1	Co-directeur de thèse

Pischedda, Vittoria, Professeure, Université Lyon 1	Invitée

Contents

Introduction

In the era of rapid scientific advancements, low-dimensional materials have emerged as a captivating field of study, revolutionizing our understanding of fundamental physics, enabling novel device functionalities and promising breakthroughs in various technological applications. Their success resides in their outstanding electronic[1, 2, 3, 4], optical[5, 6, 7] and thermal[8, 9] properties derived from their low-dimensional nature. This thrilling mix is complemented by their nanometric size resulting in extremely light materials, while preserving exceptional mechanical properties[10, 11, 12].

Extensive studies have also been directed into the possibility of tuning their properties. Temperature[13, 14], magnetic[15, 16] and electric field[17, 18, 19] are commonly used whilst pressure is often overlooked. The latter can act on those materials in various ways. Pressure affects the material structure bringing atoms closer and enhancing interactions. The electronic structure can be extensively altered leading to modification of the optical properties[20, 21, 22], with closing and opening of the band gap[23, 24, 25]. When critical densities are reached phase transitions occur, drastically modifying the materials properties[23, 26]. In the same line of thinking, novel hybrid structures can be synthesised by applying pressure to nanomaterials intercalated with external molecules, inducting the formation of bonds between the host and guest molecules as well as enhancing their mutual interaction[27, 28, 29].

While those considerations may also apply to bulk materials, when looking to low-dimensional systems, further effects can result from their reduced dimensionality. By construction, the majority or totality of their atoms constitute surface atoms. They are, thus, extremely sensitive to the surrounding environment. Pressure affects the environment increasing the electronic density and amplifying the interactions between the material and its environment. Environmental effects on low-dimensional materials in high pressure experiments are thus thoroughly studied focusing on two main elements: the substrate and the so called pressure transmitting medium. The substrate is a fundamental element of low-dimensional materials providing their support. Additionally, it is a source of mechanical strain[30, 31] and doping[32, 33]. The second element, the pressure transmitting medium, is an essential component of high pressure experiments as it is used to transfer pressure from a compression system to the sample. It therefore surrounds the studied sample and interacts with it[34, 35, 36]. The rich physics involved in high pressure experiments allows to finely combine those two elements, i.e. the substrate and the pressure transmitting medium, in order to explore a wide range of phenomena.

In the present work we focused on the study of carbon nanotubes and graphene, and how to tune their properties by engineering the environment and applying pressure. Both those materials are constituted of carbon atoms arranged in an hexagonal lattice but differing in the structural organization of the crystal. Graphene is a single atomic thick plane of carbon atoms. The confinement of the atoms in one of the spatial dimensions makes it an ideal model for a two dimensional system and it was theoretically hypothesised to be unstable for thermodynamic reasons[37, 38]. It was finally synthesised and characterized by Andre Geim and Konstantin Novoselov using simple scotch tape to mechanically exfoliate bulk graphite[1]. The two-dimensional existence paradox was resolved by integrating graphene in a three-dimensional matrix[39]. Carbon nanotubes can be formed by rolling up graphene into a cylindrical shape, ulteriorly confining them in a spatial direction, thus resulting in idealized one-dimensional systems[40].

The first chapter of this thesis will be dedicated to the introduction of the theoretical foundations and recent studies on the description and characterization of those two systems. Initially, we will describe their structure and the way to access to their properties using Raman spectroscopy. Then we will show how this technique can be used to probe environmental effects. Finally, at the end of the chapter, we will describe the state-of-the-art high pressure studies on those systems.

The technical details concerning the instrumentation involved in our experiments will make the subject of chapter two. We will focus on the description of the high pressure devices and the adjustments that have been necessary for our studies. Major attention was dedicated to the improvements of sapphire technologies for high pressure experiments. Then we will list the developments that have been realized for the preparation of samples of two-dimensional materials and their transfer into the diamond anvil cell. To conclude we will illustrate the custom made Raman spectrometer used in the majority of the experiments and the novel integration of a mapping system adapted to high pressure studies.

With the described technology we performed two main branches of experiments. The first, extending across chapter three, was devoted to the study of single walled carbon nanotubes. Carbon nanotubes are found to undergo a geometrical phase transition that transform their tube like cross section into a flattened shape when under high pressure[41, 42]. Their properties are largely modified by this transition which alter their electronic and optical properties[24, 25]. The large potential for applications calls for a detailed characterization of those transitions. The most accessible way to identify the tubes' collapse at high pressure is by using *in-situ* Raman spectroscopy. Previous studies have been performed on a large number of tubes simultaneously and they determined the collapse pressure by using indirect signatures[41, 43]. Whilst accurate, those features may partially miss the finest details associated with the transition. In this work we improved the characterization of the collapse of carbon nanotubes by using a novel spectroscopic signature which is compatible with high pressure experiments. We studied carbon nanotube bundles testing the effect of different environments by changing the pressure transmitting medium. Moreover, we disentangle the nanotubes collapse signature from eventual collective bundle effects by successfully study individualized carbon nanotubes.

The second main explored part of this work, described in chapter four, was dedicated to the study of environmental effects on graphene's response to high pressure. A strong interaction with the pressure transmitting medium has been observed when it is compressed. Depending on the nature and the physical state, the medium can strongly interact both chemically as well as mechanically with graphene, resulting in doping effects[34, 44], strain[45] and medium assisted phase transitions[23, 46]. When the substrate is also involved the observed behaviour is ulteriorly enriched with a substrate dependent response to high pressure[45]. In order to disentangle these two contributions and study the pure contribution of the pressure transmitting medium, a minimal number of experiments have been performed using suspended graphene in liquid solution[47, 48]. Those experiments showed that when graphene suspended in liquid solution is compressed it behaves similarly to graphite in opposition to what it is found when supported on a substrate[45]. Those interesting results motivated us to find new pathways for studying substrate effects on graphene at high pressure. We thus engineered dedicated suspending structures adapted to high pressure experiments which allowed us to compare simultaneously suspended and supported samples. We performed experiments both on graphene and few-layer graphene samples by measuring the effects of the environment and evaluating the outcome of adopting different pressure transmitting media. To further explore the effects of the environment on few-layer graphene, in another series of experiments we investigated the role of changing the type of substrate to therefore tune the water mediated phase transitions of graphene.

Chapter 1

Low-dimensional systems at high pressure: theoretical background and state-of-art

This chapter will cover the main theoretical aspects and the state-of-art that will support the experimental results and discussions presented in this thesis. We will focus on carbon-based low-dimensional systems giving prominence to single walled carbon nanotubes (SWCNT), graphene and graphene stacking. The theoretical foundations backing up the experimental results are centred on describing the crystallographic, electronic and vibrational structures of those systems. A section on how to characterize those systems using Raman spectroscopy will follow. We will conclude with the state-of-art for environmental and high pressure effect on low-dimensional systems.

1.1 Crystallographic Structure

Carbon-based low-dimensional systems are a remarkably vast and variate family of materials. They are characterized by sp^2 bonds, connecting carbon atoms that can be arranged to form 0D, 1D and 2D structures[49]. In order of increasing dimensionality those structures are called fullerenes[50], carbon nanotubes (CNT)[51] and graphene[52], with the last two being the object of study of this work. Despite having the same chemical composition their physical properties are completely different due to their difference in geometrical arrangement of the atoms. Carbon nanotubes can be both semi-conductors and metallic with the former having a band gap of the order of the eV[7]. Graphene is a zero-gap semiconductor exhibiting outstanding electric conductivity that made it one of the most attractive materials in nowadays material research[1]. Moreover, both materials exhibit excellent mechanical, optical and thermal conductivity properties[1, 7, 53]. In order to deeply understand the underlying mechanisms that make those materials so unique it is necessary to formally describe their crystallographic structure. We will discuss for simplicity the two materials separately in the following sections.

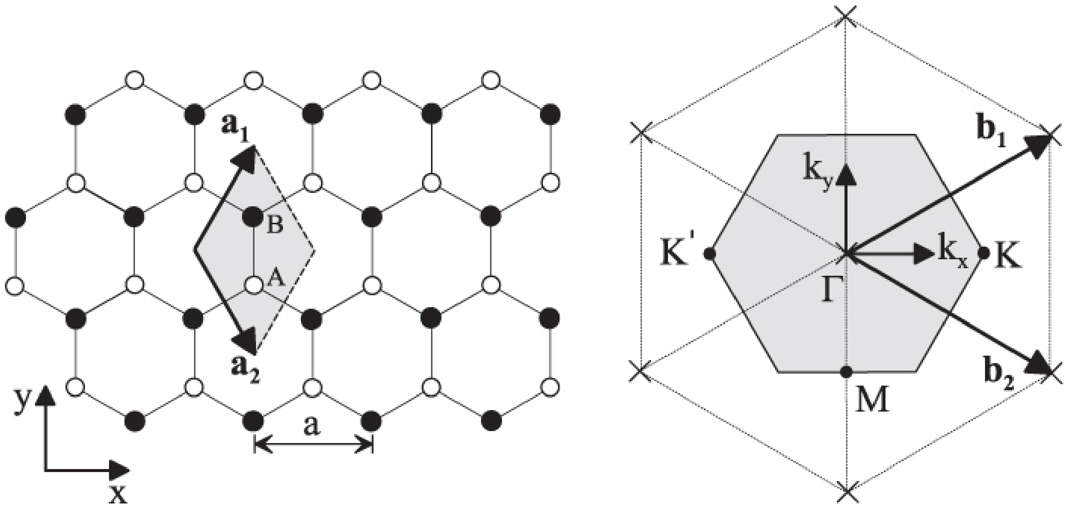

(a) (b)

Figure 1.1: (a) Schematization of graphene's crystal structure. A and B are the two non-equivalent carbon atoms in the unit cell. $\boldsymbol{a_1}$ and $\boldsymbol{a_2}$ are the lattice vectors of length a. The corresponding first Brillouin zone in reciprocal space is highlighted by the grey area in (b). Figures adapted from [54]

1.1.1 Graphene and graphite

For both CNT and graphene the crystallographic structure can be obtained considering a 2D honeycomb lattice. Two lattice vectors $\boldsymbol{a_1}$ and $\boldsymbol{a_2}$ describe the two-dimensional hexagonal structure:

$$\boldsymbol{a_1} = a(\frac{1}{2}, \frac{\sqrt{3}}{2})$$
$$\boldsymbol{a_2} = a(\frac{1}{2}, -\frac{\sqrt{3}}{2})$$
$$|\boldsymbol{a_1}| = |\boldsymbol{a_2}| = a = 2.46\text{Å}$$

A schematic representation of the lattice is shown in Figure 1.1a. Two non-equivalent carbon atoms, A and B in Figure 1.1a, compose the unit cell of the crystal, completing the description of graphene's structure in real space. The interatomic separation between neighbouring atoms a_{CC} is 1.42 Å.

In reciprocal space the first Brillouin zone is also described by an hexagonal lattice. The two primitive reciprocal lattice vectors $\boldsymbol{b_1}$ and $\boldsymbol{b_2}$ can be obtained using the identity $\boldsymbol{a_i} \cdot \boldsymbol{b_j} = 2\pi\delta_{ij}$:

$$\boldsymbol{b_1} = \frac{2\pi}{a}(1, \frac{1}{\sqrt{3}})$$
$$\boldsymbol{b_2} = \frac{2\pi}{a}(1, -\frac{1}{\sqrt{3}})$$
$$|\boldsymbol{b_1}| = |\boldsymbol{b_2}| = 2.95\text{Å}^{-1}$$

The resulting first Brillouin zone is shown in Figure 1.1b. There are four high symmetry points that result from it. The point Γ, the first Brillouin zone centre,

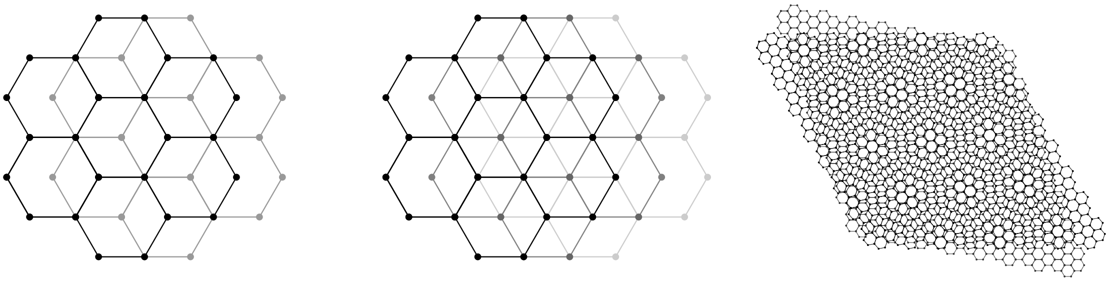

(a) AB (Bernal) **(b)** ABC **(c)** Turbostratic

Figure 1.2: Different patterns obtained by stacking graphene layers.

two non-equivalent corners of the first Brillouin zone K and K' and the centre of the sides M.

The two-dimensional one-atom-thick structure we described is the structure of graphene. Graphene sheets can be stacked together in order to form different structures depending on the number of layer and their relative orientation in the stacking. In the limit of great number of layers we obtain the well known graphite. Its stacking can be of two kind AB (Figure 1.2a) or ABC (Figure 1.2b), the former, also called Bernal stacking, being its most stable structure. The interlayer distance is 3.34 Å. More exotic stacking patterns appear when we reduce the number of layers to few units. An important case is given by a number of layers equal to two with the so-called bilayer graphene. Arbitrary stacking orientations are found to be stable in this case with bilayer graphene's properties being dependent on the relative angle between the layers (Figure 1.2c). This kind of stacking is referred as twisted bilayer or turbostratic graphene in the literature. A remarkable case is when the two layers of graphene are mismatched by $\sim 1.1°$. At this angle the twisted bilayer exhibit a superconducting behaviour at low temperature[55].

1.1.2 Nanotubes

The structure of single-wall carbon nanotubes can be obtained taking the structure of a graphene sheet and *rolling* it into a cylinder-like shape. The direction of graphene's folding will define the so called chiral vector $\boldsymbol{C_h}$ using two integer indices (n,m) associated with one of graphene's crystallographic directions:

$$\boldsymbol{C_h} = n\boldsymbol{a_1} + m\boldsymbol{a_2} \tag{1.1}$$

where $\boldsymbol{a_1}$ and $\boldsymbol{a_2}$ are the lattice vectors of graphene introduced in the previous section. The tube axis is orthogonal to $\boldsymbol{C_h}$ and its diameter is defined by:

$$d_t = |\boldsymbol{C_h}|/\pi = \sqrt{3}a_{CC}\sqrt{m^2 + mn + n^2}/\pi \tag{1.2}$$

Figure 1.3 show an example of construction of the chiral vector of a tube with (n,m) = (4,2) from graphene's honeycomb lattice[56]. Defining a second vector (OB in Figure 1.3) as the shortest distance along the tube's axis that repeats the structure the unit cell will be defined by the rectangle OAB'B in Figure 1.3. The

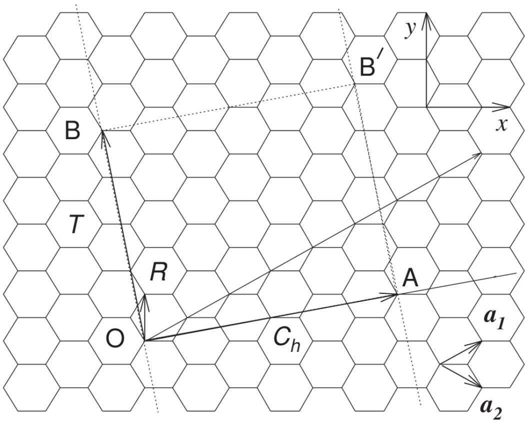

Figure 1.3: Example of definition of the chiral vector C_h and the unit cell in carbon nanotubes from graphene's lattice. This particular case is associated to a nanotube of chirality (4,2). Figure adapted from [56].

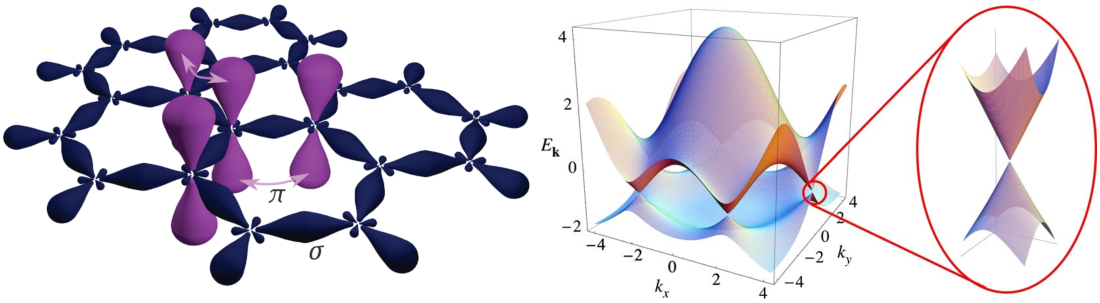

(a) **(b)**

Figure 1.4: (a) Schematic arrangement of carbon's σ and π orbitals in graphene. (b) 3D plotting of the energy of the valence and conductions bands originated by the π orbitals as a function of the electron momentum. Circled in red a zoom on the linear dispersion relation at the point K around the Fermi level. Figures taken from [57] and [58]

number of atoms in the unit cell will depend on the chirality. The chirality of nanotubes characterize their physical properties and allows us to distinguish three categories:

- zig-zag tubes when $m = 0$
- armchair tubes when $n = m$
- chiral tubes for all other values

1.2 Electronic structure

Carbon atoms in graphene are hybridized sp^2. The hybridization process gives origin to three σ orbitals that are responsible of the strong in-plane bonds and a remaining p_z orbital which is oriented orthogonally with respect to the graphene's plane and forming π bonds (Figure 1.4a). Its electronic band structure can be obtain using a tight binding model approximation calculating separately the bands originated by the p_z and σ orbitals. For the p_z orbitals the calculated bands are shown in Figure 1.4b. A common approximation also consider as zero the overlap integral of the p_z orbitals. The resulting 2D dispersion relation for a given electron momentum $\boldsymbol{k} = (\boldsymbol{k_x}, \boldsymbol{k_y})$ is given by [59]:

$$E(\boldsymbol{k}) = \pm t \left(1 + 4\cos\left(\frac{\sqrt{3}k_x a}{2}\right)\cos\left(\frac{k_y a}{2}\right) + 4\cos^2\left(\frac{k_y a}{2}\right)\right)^{1/2} \tag{1.3}$$

where a is the lattice constant and $t \sim 2.8$ eV is the nearest-neighbour hopping energy. The plus and minus signs refer respectively to the valence and conduction energy bands. The Fermi level in graphene is situated at the high symmetry points K and K' where the conduction and valence bands come to join, making graphene a zero-gap semiconductor. Moreover, around this point we find that the energy is linear with the momentum[60] (red circle in Figure 1.4b) and can be described as:

$$E = \hbar \nu_F \sqrt{k_x^2 + k_y^2} \tag{1.4}$$

with $\hbar$ the reduce Plank constant and ν_F graphene's Fermi velocity. This peculiarity is at the origin of multiple quantum effects that make graphene unique as the room temperature quantum Hall effect and Hall conductivity[60].

When stacking different graphene layers the band structure is also modified by the interlayer interaction. The electronic bands split starting from the introduction of one layer in bilayer graphene. Increasing the number of layers increases the complexity of the band structure up to 10 layer where we recover the band structure of graphite [61]. Figure 1.5 shows the evolution of the band structure around K for one, two and few layers graphene, and graphite.

The band structure of carbon nanotubes can also be derived from that of graphene. Due to the tube's confinement in the direction of the chiral vector $\boldsymbol{C_h}$ we can use periodic boundaries conditions obtaining the quantization of the momentum in the direction associated with $\boldsymbol{C_h}$. The direction corresponding to the tube axis remains continuous[59]. Imposing this condition on the momentum results in the quantization of the energy shown as cutting lines in the 2D band structure of graphene thus reducing the allowed energy states[56]. Figure 1.6a show an example of cutting lines calculated for a tube (4,2). The resulting bands are shown in Figure 1.6b. The position of the cutting lines in the first Brillouin zone will determine the metallic or semiconducting nature of the tubes based on whether a line cuts the high symmetry point K of graphene's Brillouin zone or not. It is possible to know when this happens computing the relation, $MOD(2n + m, 3)$. We can distinguish two cases: when $MOD(2n + m, 3) = 1$ or 2 we observe a semiconducting behaviour with a diameter dependent band gap. In the case $MOD(2n + m, 3) = 0$, where we find allowed $\boldsymbol{k}$ vectors crossing the K point, we have the closure of the band gap and a metallic behaviour[56].

In addition to the shape of the electronic bands, nanotubes electronic and optical properties are derived by their electronic density of states. In CNTs the

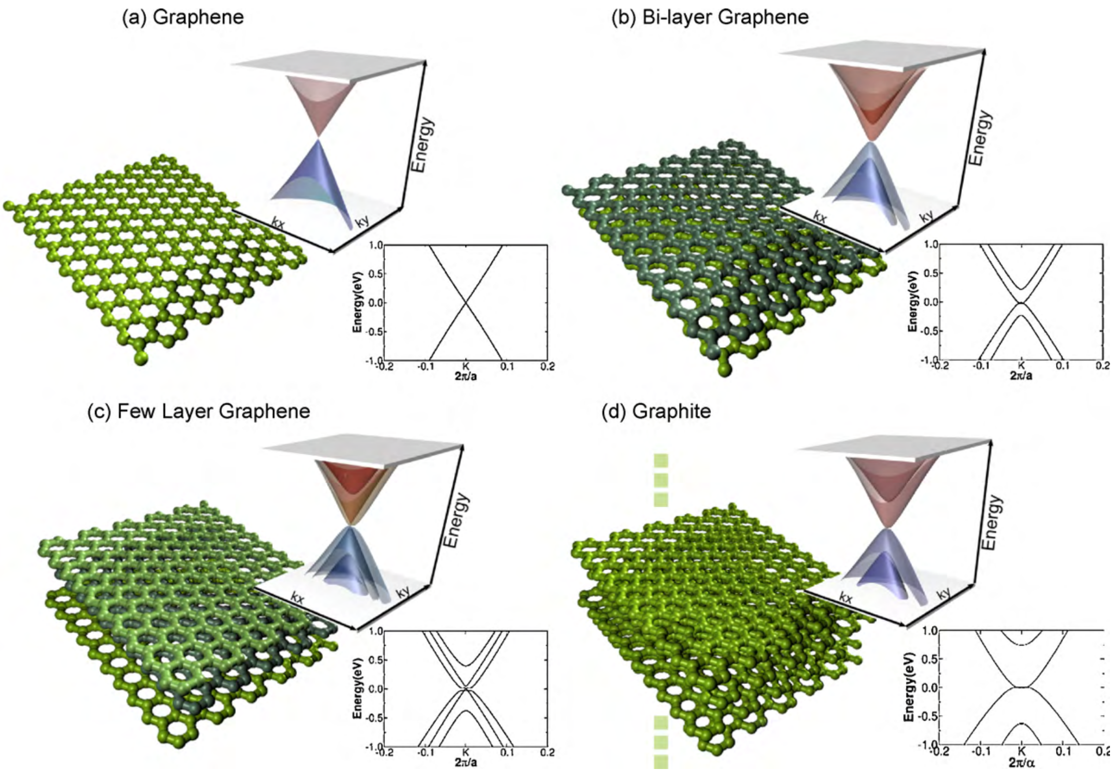

Figure 1.5: DFT calculations of graphene and graphene stacking dispersion relations around K close to the Fermi level plotted in three dimensions. The projection on k_x is also plotted in two dimensions. Figure taken from[62]

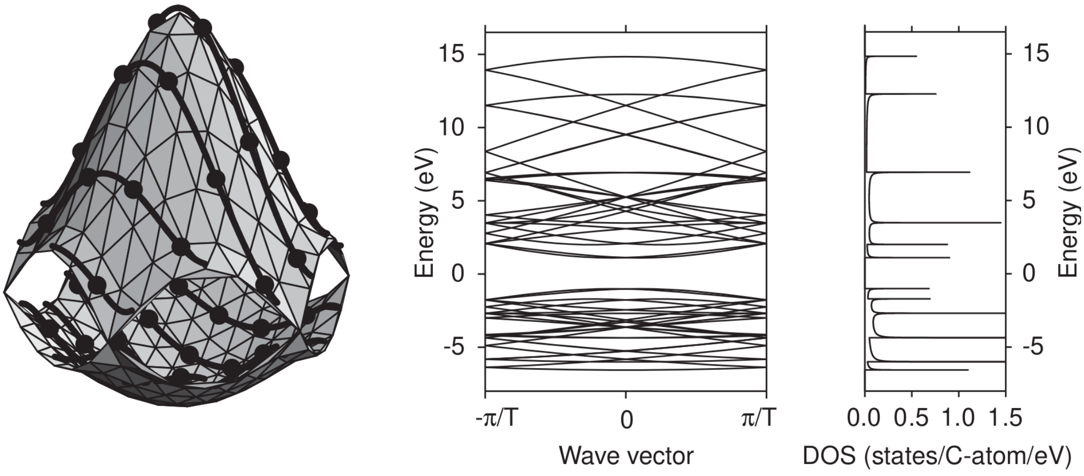

(a) **(b)** **(c)**

Figure 1.6: (a) Cutting lines (thick black lines) imposed on graphene's conduction and valence π-band energy contour for a tube (4,2). (b) for the same tube the electronic band structure obtain by zone folding and (c) the corresponding density of states. Figures taken from [56]

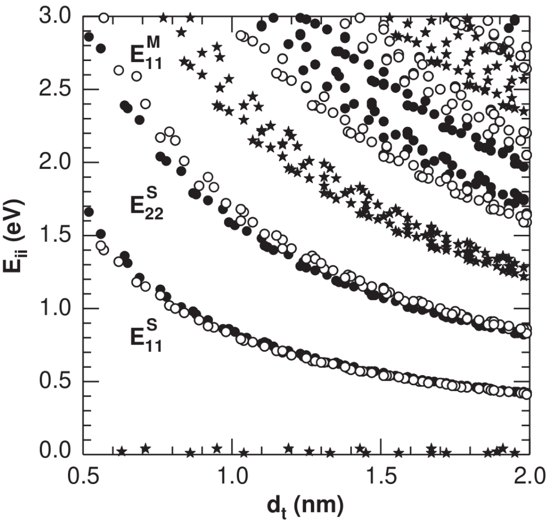

Figure 1.7: Partial Kataura plot showing the electronic transitions E_{ii} in SWCNT as a function of the tube's diameter calculated by first-neighbour tight binding method. Black stars correspond to metallic tubes. Filled and empty circles correspond to respectively to $MOD(2n+m,3) = 1$ and 2 semiconducting tubes. Figure taken from [56].

density of state presents van Hove singularities (vHSs) due to their quasi-1D character. This is shown by the presence of peaks in the density of state at energies corresponding to critical points in the electronic bands. Figure 1.6c shows the density of state as a function of energy for a (4,2) tube. Electronic transitions at energies corresponding to vHSs will be strongly enhanced by the high density of states. Due to the dependency of vHSs on the nanotubes diameter and chirality it is possible to assign a set of transition energies between valence and conduction bands to each nanotube allowing for the identification of the nanotube's chirality using optical techniques[56]. Each transition of the set is identified by an integer index $i = 1, 2, 3\dots$ and the corresponding energy is labelled as E_{ii}, with the transitions ordered by increasing energy magnitude. The transitions E_{ij} between the ith singularity in the valence band to the jth in the conduction one occur with a much smaller probability in one photon processes due to symmetry reasons[63]. The collection of computed values of the sets of E_{ii} can be plotted in the so-called Kataura plot[7]. Figure 1.7 displays a fraction of the Kataura plot for nanotubes of diameter between 0.5 and 2 nm and electronic transition energies up to 3 eV.

1.3 Phonons

Graphene crystals are formed using two carbon atoms as a base for the crystal lattice. This results in six phonon branches, three acoustic and three optical. At the centre of the Brillouin zone we have four normal modes, two of them doubly degenerate: $A_{2u}+B_{2g}+E_{1u}+E_{2g}$[64]. The two optical modes B_{2g} and E_{2g} describe respectively the out-of-plane and in-plane vibration with E_{2g} doubly degenerate. A_{2u} and E_{1u} correspond to the acoustic branches. One A_{2u} mode for the

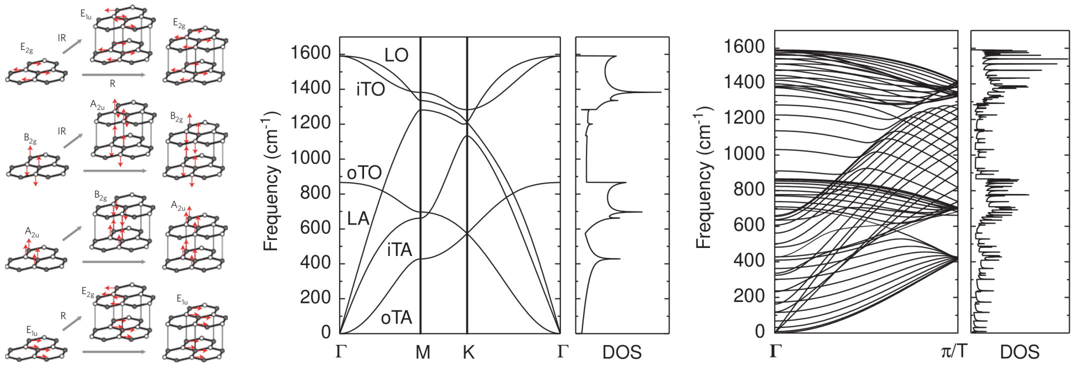

(a) **(b)** **(c)**

Figure 1.8: (a) Vibrational modes in graphene and graphite at the centre of the Brillouin zone Γ. Red arrows indicate the atomic displacements. The duplication of modes in graphite from the graphene ones is shown by the grey arrows. (b) Computed phonon bands and DOS for graphene and (c) a (10,10) SWCNT. Figures taken from [64] and [56]

out-of-plane vibrations and two degenerate in-plane E$_{1u}$ modes[65]. Figure 1.8a shows a schematic representation of the corresponding vibrations at Γ. If we consider a phonon momentum different from zero we can obtain the complete phonon dispersion relation. In Figure 1.8b we can observe the phonon modes evolution along the major symmetry direction of graphene[56]. In order to obtain graphite's phonon modes in a Bernal stacking we need to consider the two additional atoms composing the unit cell doubling the number of phonon modes to 12. Each graphene mode splits into two modes corresponding to in-phase and out-of-phase oscillations between neighbouring planes. Due to the weak Van der Waals forces bonding the layers the difference in energy induces a very weak degeneracy splitting (less then 10cm^{-1})[66]. The resulting set of normal modes at Γ is given by 2(A$_{2u}$+B$_{2g}$+E$_{1u}$+E$_{2g}$)[64]. Figure 1.8a show the described splitting of graphene's modes into the graphitic ones.

Phonon modes for carbon nanotubes can, once again, be derived using graphene as a starting point and following a similar folding procedure to that performed when we obtained their electronic band structure[56]. The higher number of atoms in the unit cell will result in a greater number of phonon branches revealing a much more complex phonon structure compared to that of graphene. Figure 1.8c shows an example of calculated phonon dispersion relation obtained using the folding procedure for a (10,10) SWCNT[56]. The density of state is also computed and shown in Figure 1.8c.

1.4 Characterization of low-dimensional systems using Raman spectroscopy

Low-dimensional system's unique optical properties open up to a vast range of techniques for their characterization that allow us to probe those materials despite

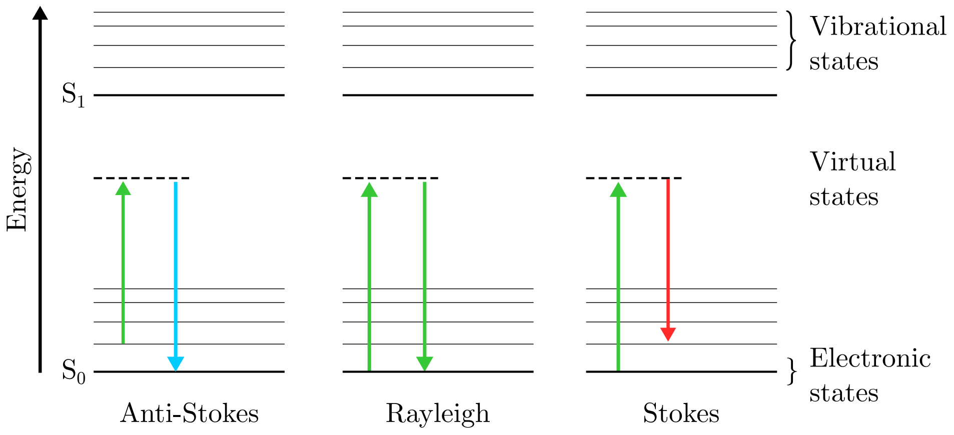

Figure 1.9: Schematic representation of Rayleigh and Raman scattering processes. Coloured arrows indicate the electronic transitions involved in the processes.

the extremely low quantity of matter they are composed of. Very widely used are optical absorption, photoluminescence and Raman spectroscopy. In this work we will focus on Raman spectroscopy as it has been thoroughly exploited throughout the experiments and thus it will make object of this theoretical introduction.

1.4.1 Raman spectroscopy principles

Raman spectroscopy is a commonly used technique for probing low-dimensional materials. It is a vibrational spectroscopy technique that is based on inelastic photons scattering with the production/annihilation of one or multiple phonons. The scattering process involves the excitation of an electron from the valence to an excited state creating an electron-hole pair, the absorption or emission of phonons and the de-excitation of the electron to the valence band emitting a new photon. In this process the re-emitted photon will have an energy which will differ from the incoming photon energy by the absorbed and emitted phonons' energy[56]. We can distinguish three types of scattering: (i) Rayleigh elastic scattering where a photon is scattered without any changes in energy, (ii) inelastic anti-Stokes where one or multiple phonons are absorbed in the process and the emitted photon will be at higher energy than the incoming one and (iii) inelastic Stokes where phonons are created with a loss in energy of the photon. Those three processes are schematized in Figure 1.9. The cross section of the inelastic scattering process is much lower then its elastic counter part. However, a enhancement can be achieved when we involve resonance processes. In order to better understand this phenomenon we can look in more details into the theory of Raman spectroscopy.

The Raman effect can be studied starting from a classical description in terms of oscillating dipoles. Assuming an incident electric field amplitude $\boldsymbol{E} = \boldsymbol{E_0} \cos(\boldsymbol{k} \cdot \boldsymbol{r} - \omega t)$ oscillating at a frequency ω we can describe the induced dipole moment $\boldsymbol{P}$ of a molecule as:

$$\boldsymbol{P} = \alpha \boldsymbol{E} \tag{1.5}$$

The polarizability α can be expressed in general by a tensor α_{ij} of rank two but we will consider a scalar polarizability α assuming an isotropic medium for simplicity. We can simplify the dynamics of the molecular displacements induced by this dipole considering only the position of the nuclei due to the much faster electronic dynamics. When considering small nuclear displacements we can expand the polarizability in a Taylor series around the equilibrium positions obtaining:

$$\alpha = \alpha_0 + \sum_i^N \left(\frac{\partial \alpha}{\partial \boldsymbol{Q_i}} \right)_0 \boldsymbol{Q_i} \tag{1.6}$$

where N is the number of nuclei, α_0 is the polarizability at the equilibrium position and $\boldsymbol{Q_i}$ are the normal coordinates of the nuclear displacements. For vibrations of small amplitude we can also approximate the normal coordinates with:

$$\boldsymbol{Q_i}(r,t) = \boldsymbol{Q_{i0}} \cos\left(\boldsymbol{q_i} \cdot \boldsymbol{r} - \omega_i t\right) \tag{1.7}$$

with $\boldsymbol{Q_{i0}}$, $\boldsymbol{q_i}$ and ω_i the amplitude, the wavevector and the frequency of the ith normal vibration. Injecting Equation 1.6 and Equation 1.7 into Equation 1.5 we obtain the resulting polarization:

$$\begin{aligned} \boldsymbol{P} = \alpha_0 \boldsymbol{E_0} \cos\left(\boldsymbol{k} \cdot \boldsymbol{r} - \omega t\right) &+ \frac{1}{2} \boldsymbol{Q_{i0}} \boldsymbol{E_0} \sum_i^N \left(\frac{\partial \alpha}{\partial \boldsymbol{q_i}} \right)_0 \cos\left((\boldsymbol{k} - \boldsymbol{q_i}) \cdot \boldsymbol{r} - (\omega - \omega_i)t\right) \\ &+ \frac{1}{2} \boldsymbol{Q_{i0}} \boldsymbol{E_0} \sum_i^N \left(\frac{\partial \alpha}{\partial \boldsymbol{q_i}} \right)_0 \cos\left((\boldsymbol{k} + \boldsymbol{q_i}) \cdot \boldsymbol{r} - (\omega + \omega_i)t\right) \end{aligned} \tag{1.8}$$

The three terms we obtained describe respectively the Rayleigh elastic scattering, Raman Stokes and Raman anti-Stokes inelastic scattering processes shown in Figure 1.9. The frequencies and momenta of the inelastically scattered photons are $\omega \pm \omega_i$ and $\boldsymbol{k} \pm \boldsymbol{q_i}$ with the minus and plus signs referring respectively to the Stokes and anti-Stokes processes.

While a classical description of the field allows to outline Raman frequencies and phenomena, a quantum mechanical description is necessary in order to extract Raman lines intensities. We will discuss now of some results that can be obtain using quantum mechanics without giving their thorough derivation. More rigorous treatments can be found in reference[67].

The intensity of Raman lines can be obtained through the computation of the transition probabilities for a given Raman process. The Hamiltonian that describes the scattering process is composed of three elements:

1. an electron-radiation Hamiltonian H_{e-r} describing the excitation of an electron from an initial state $|i\rangle$ to an intermediate state $|n\rangle$ creating an electron-hole pair

2. an electron-phonon Hamiltonian H_{e-ion} for the scattering of the electron-hole pair into another state $|n'\rangle$ emitting a phonon

3. the electron-hole recombines radiatively via the interaction of H_{e-r}

The shape of H_{e-r} can be obtained using a semi-classical approach. The incoming electromagnetic field describing the radiation can be written in term of the vector potential $\boldsymbol{A}$. Using the appropriate choice of gauge we can obtain the Hamiltonian for the interaction of the electromagnetic field with an electron in the form:

$$H_{e-r} = \frac{e}{mc}\boldsymbol{A} \cdot \boldsymbol{p} \tag{1.9}$$

where e and m are the electron charge and mass, c is the speed of light in vacuum, and $\boldsymbol{p}$ is the electron momentum. The second interaction involved in a scattering process, the electron-phonon hamiltonian H_{e-ion}, is originated from the Born-Oppenheimer approximation used in the tight binding approach that allowed us to obtain the electronic band structure in Section 1.2. This term accounts for the relative motion of electron and ions in the crystal. Its derivation is beyond the scope of this work, for more details the reader can refer to [67].

To compute the Raman scattering probability we can use time-dependent perturbation theory injecting the interaction Hamiltonian describing the three step process. We obtain a scattering probability P_R for an incoming photon of frequency ω_i and scattered photon and phonon of frequencies ω_s and ω_0 in the form[67]:

$$P_R(\omega_s) = \left(\frac{2\pi}{\hbar}\right) \left| \sum_{n,n'} \frac{\langle i|\, H_{e-r}(\omega_s)\, |n'\rangle \, \langle n'|\, H_{e-ion}\, |n\rangle \, \langle n|\, H_{e-r}(\omega_i)\, |i\rangle}{[\hbar\omega_i - (E_n - E_i)][\hbar\omega_i - \hbar\omega_0 - (E_{n'} - E_i)]} \right|^2 \times \delta[\hbar\omega_i - \hbar\omega_0 - \hbar\omega_S] \tag{1.10}$$

where $\delta[\hbar\omega_i - \hbar\omega_0 - \hbar\omega_S]$ is the Kronecker delta which accounts for conservation of energy and E_j is the energy of the j_{th} state.

An important consequence arises from Equation 1.10 which is the so called resonant Raman scattering. This phenomenon occurs when the incident photon energy matches with the energy of one or some electronic band transition. If this is the case we can see that one or both the denominators in Equation 1.10 cancel out and the probability P_R diverges allowing for an enhancement of Raman lines' intensity by several orders of magnitude. The divergence of the denominators in Equation 1.10 is however an unphysical situation. This inconsistent behaviour is solved when considering the energy of the intermediate states n and n' imaginary in the form $E_j + \mathrm{i}\Gamma_j$[67]. Those intermediate states have a finite lifetime τ_j due to radiative and nonradiative decay processes. As a consequence a damping constant term $\Gamma_j = \hbar/\tau_j$ is introduced in the state's energy.

In the following section we will discuss how this theoretical formalism of Raman spectroscopy applies to the carbon-based low-dimensional systems.

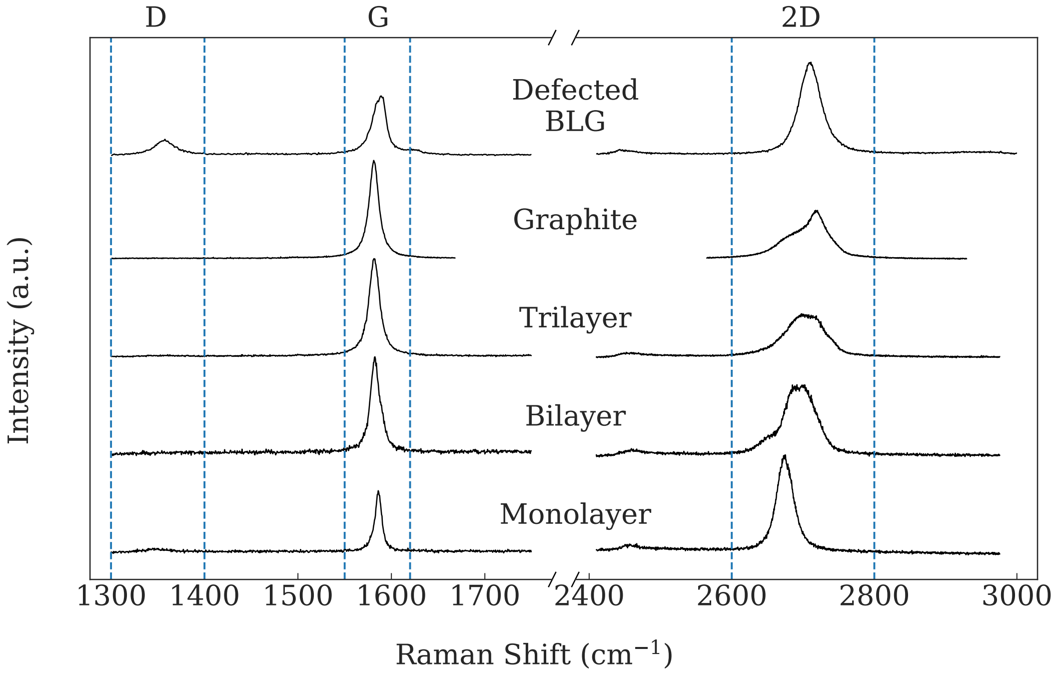

Figure 1.10: Main features of the Raman spectrum of graphene and graphene stacking. We can notice the change in shape of the 2D-band when adding successive graphene layers as well as the appearance of the D-band when defects are present in bilayer graphene (BLG).

1.4.2 Raman spectroscopy of graphene and graphene layered structures

Resonant Raman spectroscopy is an extremely powerful tool for the study of two-dimensional system. As well as giving direct information on the vibrational properties of those materials it allows for the measurement of strain[68, 69] and doping levels[69, 70], quantify the presence of disorder[71] as well as characterize the type of bonds within their structure[71]. Figure 1.10 shows typical Raman spectra of graphene, few-layer graphene and graphite.

Around 1582 cm^{-1} we can observe the so-called G-band. It is the principal first-order Raman process that characterize graphene and graphene layered materials[56]. It corresponds to the $\text{E}_{2\text{g}}$ phonon at the centre of the first Brillouin zone Γ describing the degenerate in-plane transversal optic (iTO) and longitudinal optic (LO) atomic vibrations (see Figure 1.8a). A schematic of the generation of a G-phonon is shown in Figure 1.11. The G-band is directly connected with the strength of the sp^2 bond and it can be use as a probe of in-plane strain[72] and doping effects in graphene [70].

In addition to the fist-order G-band we can find several second or higher order Raman processes. Those processes in graphene can involve either contributions of additional scatterers as well as the creation or annihilation of multiple phonons. The most common form of scatterer is given by the presence of defects in the structure. This type of scattering give origin to the so called D and D'-bands that are found respectively around 1350 cm^{-1} and 1620 cm^{-1} (using 2.41 eV excitation energy). The are originated by the formation of an iTO phonon in inter-valley process and an iLO phonon in intra-valley process respectively. The former involves two electronic states around the non-equivalent K and K' points whilst in the latter the two states belong to the same valley. For this reason their phonon wave vector differs with $|\boldsymbol{q}| \sim K$ for the D-band and $|\boldsymbol{q}|$ close to Γ for the D'-band. We thus scan different regions of the phonon dispersion relation with resulting different phonon energies. We can see a schematic of the processes in Figure 1.11. Those modes are activated in the presence of disorder and defects so they are often used to measure the sample quality and deterioration[71].

Another important mode is the D-band overtone called G' or 2D mode. This mode is generated by the second-order two-phonon process shown in Figure 1.11. It involves inelastic scattering with the creation of two iTO phonons of opposite momentum $\boldsymbol{q}$ and $-\boldsymbol{q}$. The momentum conservation is respected thanks to the two phonons momentum cancelling out allowing for exploring different regions of the phonon dispersion curves away from the Γ point. As for the D-band case it is a inter-band process with $|\boldsymbol{q}| \sim K$. This band is a powerful tool for the measurement of strain and doping in graphene[69, 73]. It is also an extremely accessible and accurate method for the measurement of the number of layers in Bernal graphene stacking allowing for the identification of mono to quadri-layer graphene and bulk graphite[74].

Additional weak signals can be seen in the Raman spectrum of graphene. Defect-activated and multiple phonon processes can be originated from combinations of the previously described modes. When dealing with graphene stacking

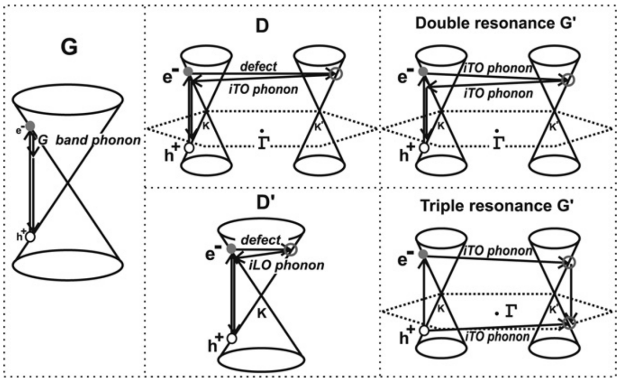

Figure 1.11: Schematic representation of the main resonant Raman processes in graphene. The cones represent the energy bands around K and K'. Figure taken from[76].

breathing modes issued from interlayer coupling are also observed at low energies[75]. As they have not been studied in this work they will not be discussed further.

1.4.3 Raman spectroscopy of SWCNTs

Much of the discussion about the Raman spectrum of graphene can be adapted to the description of that of SWCNT with some important differences. When looking at the phonon band shown in Figure 1.8c we can see a much more complex structure compared to that of graphene. The number of phonon modes is equal to $6N-4$ with N the number of carbon atoms in the unit cell indicating a strong dependency on the nanotube's chirality and diameter. In practice the Raman spectrum of SWCNTs largely simplifies when taking into account group theory selection rules. First-order Raman processes at the zone centre Γ involved 15 or 16 Raman-active modes. The number is ulteriorly reduced due to the small cross section associated to some modes resulting in weak signals[59].

Figure 1.12 shows a typical spectrum of the main Raman features of SWCNTs. Two strong Raman features in the range 1550-1600 cm^{-1} can be attributed to the splitting of the degenerate E_{2g} mode of graphene associated with the G-band[59, 56]. The nanotube curvature brake the in-plan vibrational symmetry at the origin of the degeneracy of the mode. Traditionally the two features are referred as G^+ and G^- in the literature. They describe the atomic vibration along the tube axis and in the circumferential direction respectively in the case of semiconducting CNTs (the inverted convention applies to the metallic CNTs)[59]. Figure 1.13a shows the comparison between the G-band of HOPG graphite, G^+ and G^- of metallic and semiconducting SWCNT's . The high energy G^+ at ~ 1590 cm^{-1} associated with the on-axis vibrations is found to be independent on the tube's diameter for both tube types. At lower energy we can find the G^- which, on the other hand, is diameter dependent with its frequency ω_{G^-} behaving as:

$$\omega_{G^-} = \omega_{G^+} - \frac{C}{d^2} \tag{1.11}$$

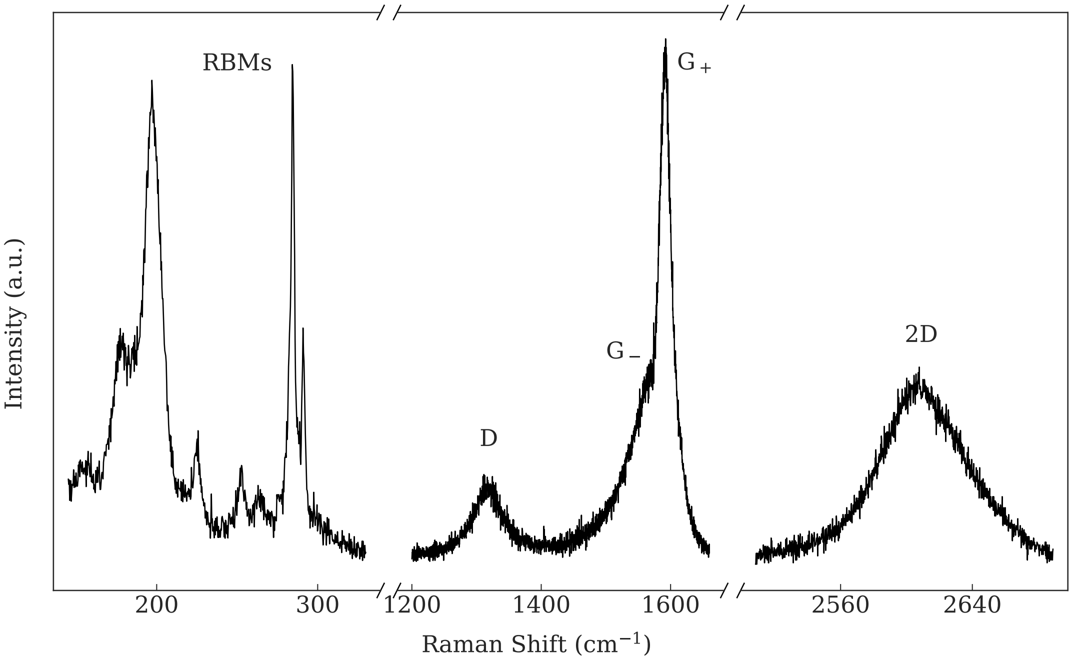

Figure 1.12: Typical Raman spectrum of SWCNT bundles. In addition to the graphene-like features we observe the splitting of the G-band in its G$^+$ and G$^-$ components as well as the radial breathing modes (RBM) at low vibrational energies.

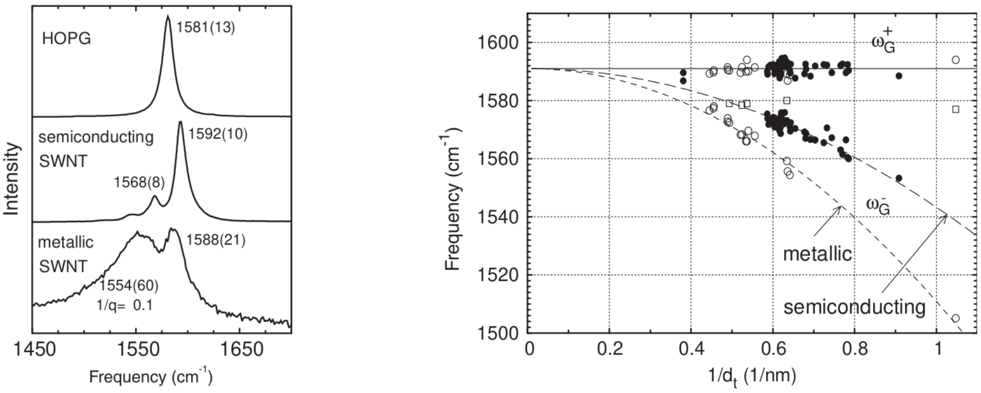

(a) **(b)**

Figure 1.13: (a) Comparison of Raman spectra of graphite and individualized semiconducting and metallic SWCNT. The metallic tube shows the characteristic large Breit-Wigner-Fano lineshape for the G$^-$ peak while the semiconducting one preserves a Lorentzian shape for all modes. The dependency of the ω_{G^-} and ω_{G^+} frequencies are plotted in (b) as a function of the inverse of the tube's diameter d_t for several tubes. Open and filled circles correspond respectively to metallic and semiconducting tubes. A peak was sometime observed also at $\sim$ 1580 cm^{-1} shown by empty square symbols. Dashed lines indicate the data fitting showing the inverse square dependency of the ω_{G^-} mode to the diameter. Figure taken from[77]

where d is the tubes diameter, ω_{G^+} is the frequency of the G$^+$ mode and C = 47.7 cm^{-1}nm^2 for semiconducting SWCNTs and C = 79.5 cm^{-1}nm^2 for metallic ones[77]. This dependence is highlighted in Figure 1.13b. Beside the G-band splitting in SWCNT we can notice a substantial difference in the shape of G$^-$ of semi-conducting and metallic tubes. In semiconducting tubes G$^-$ is described by one or multiple Lorentzians while metallic tubes are described by a Breit-Wigner-Fano lineshape. The origin of the broadening of the G$^-$ peak is still debated but it is commonly assigned to a strong electron-phonon coupling in metallic carbon nanotubes [78, 79].

Beside the graphene G-like band there are several other lower energy modes. Of particular interest we find the so-called radial breathing modes (RBMs). Those modes are associated with the vibration along the radial direction of the tube. They are found at relatively low frequencies in the range between 100 cm^{-1} and 400 cm^{-1}. They are very widely used for the determination of the nanotube's diameter as their frequency ω_{RBM} can be easily extracted, even in bundle samples. ω_{RBM} has been found to be inversely proportional to the tube's diameter d as[80]:

$$\omega_{RBM} = \frac{227}{d}\sqrt{1 + C_e d^2} \tag{1.12}$$

where C_e is a parameter that includes the environmental effects of the surrounding of the nanotube[81, 80]. An approximated formula is also commonly used in literature to determine the nanotube's diameter from RBMs[56]:

$$\omega_{RBM} = \frac{A}{d} + B \tag{1.13}$$

with A and B two constants obtained experimentally. The values of C_e, A and B are obtained from the fitting of experimental data thanks to various works[82, 83, 84, 85, 86, 87]. For SWCNT bundles, the bundle itself is considered as the tube's environment due to tube-tube interactions. Values of $A = 234$ cm^{-1}nm and $B = 10$ cm^{-1} have been found for tubes with $d = 1.5 \pm 0.2$ nm[87]. For individual nanotubes on SiO$_2$ substrates $A = 248$ cm^{-1}nm and $B = 0$ cm^{-1} have been found[85, 86].

In addition to first order Raman processes previously described, several higher-order processes arise from the rich phonon dispersion band of SWCNTs. As for the graphene case two main features are most commonly studied which are the D and its overtone 2D bands. In Section 1.4.2 we described the origin and characteristics of those bands in graphene and graphite. In SWCNTs additional information can be extracted from those bands.

The D-band is generally associated with structural defects in sp^2 structures. For carbon nanotubes it has been proved that a defect-free tube can have a strong Raman D-band originated by geometrical symmetry breaking of the structure[88]. This topic will be at the centre of the theoretical foundations in the following experimental chapter so for the details of this mechanism the reader can refer to Chapter 3. Moreover, both the D and 2D bands are strictly interconnected with the nanotube's electronic band structure. They are thus of extreme importance for its characterization and for that of the van Hove singularities in the SWCNTs density of states[89, 90, 91].

1.5 Environmental effect and external fields on low dimensional systems

In the previous section we described the potential of Raman spectroscopy as a tool for probing low-dimensional material's properties. In the following section we will show how those principles have been used to study substrate and environmental effect on those materials through a review of the state of art on the subject.

1.5.1 Substrate induced effects

The substrate is a fundamental building brick of low-dimensional systems. The necessity of carefully handle and characterize those systems stimulated the research for the most suitable bulk materials to use as a substrate, as well as to construct structures that would allow for partial suspension of the samples. Substrate engineering played an essential role for the first identification and isolation of graphene. In their pioneering work, Novoselov, Geim et al. [1, 52] proposed the use of a carefully oxidized silicon substrate as a way to enhance graphene contrast. The suggested 300 nm as the perfect thickness of SiO$_2$ on top of bulk silicon allows

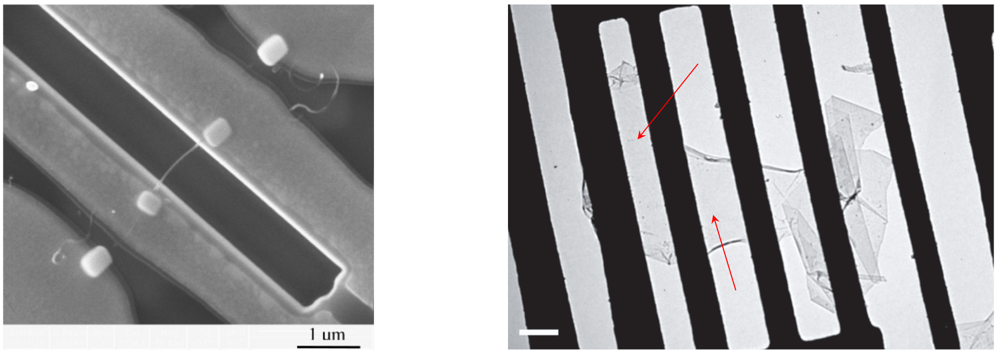

(a) (b)

Figure 1.14: (a) Suspended SWCNT imaged using SEM microscopy and (b) graphene imaged using bright-field TEM imaging. Scale bar, 500 nm. Right arrows indicate suspended graphene regions. Figures taken from [97] and edited from [39].

graphene to become visible using easily accessible optical microscopy techniques thanks to interference effects. Since then oxidized silicon wafers (Si/SiO$_2$) became the substrate of choice for the majority of experiments involving low-dimensional materials. On top of increasing optical contrast a strong enhancement of the Raman signal follows from similar considerations. Yoon et al. reported an increase of graphene's Raman signal of 370% when deposited on Si/SiO$_2$[92] with Wang et al. estimating a possible enhancement of a factor 300[93]. Moreover, substrate enhancement effects on the Raman spectrum are not uniform with the wavelength resulting in a modulation of the relative intensity of the Raman signatures[92].

Si/SiO$_2$ substrates are also found to interact chemically with the overlaying material. Impurities trapped on the substrate's surface can induce charge injection inhomogeneities[32, 33, 94]. Undesired effects can arise from this as in the graphene case where values of electric conductivity much lower than the predicted ones are found[95]. In order to prevent those undesired effects as well as to simplify the understanding of fundamental mechanisms occurring in low-dimensional materials several authors engineered suspending structure disentangling substrate effects and pure sample responses[96, 97, 98, 39]. Example of those suspended samples are shown in Figure 1.14.

Another approach is to use hexagonal Boron Nitride (hBN), a 2D material similar in structure to graphene but with a large bandgap, as an atomically-flat substrate to limit wrinkles and charge puddles[99]. High conductivity is observed in graphene supported or embedded in hBN[99, 100], and this configuration is usually chosen when aiming for high quality optoelectronic devices[100, 101, 102].

1.5.2 Raman modes evolution with strain

Carbon nanomaterial exhibit outstanding mechanical properties. The characterization of those properties, despite being of essential importance for tuning and finding the limits of quality devices, often can not be done using conventional techniques due to samples' nano-dimensions. A technique that is often used to extract their mechanical parameters is Raman spectroscopy. As it has been introduced in Section 1.4.1 Raman spectroscopy gives direct access to the atom vibration energies. We can model the evolution of the phonon modes by taking the dynamic equation of the atoms for a given phonon mode[73]:

$$-m\ddot{u}_i = m(\omega^0)^2 u_i + m\sum_{klm} K_{iklm}\epsilon_l u_k \tag{1.14}$$

with m the mass of the ions, ω^0 is the unstrained frequency of the mode, $u_{i=x,y,t}$ the ionic displacement along the spatial directions, K_{iklm} is an element of the fourth rank tensor of the bond force constants and ϵ is the strain. The solution of the equation is given in the literature and it solves in the case of the G-band mode frequency of graphene ω_G as[103]:

$$\omega_G^{\pm} = \omega_G^0 - A^{\pm}\epsilon \tag{1.15}$$

where $A^{\pm}$ is a function depending on graphene's Poisson ratio and the $+$ and $-$ signs refer to the two degenerate G-band eigenmodes which split in the case of uniaxial strain. In our experiments we were particularly interested in the effects of biaxial strain on graphene and few-layer graphene. In such case the degeneracy is kept and Equation 1.15 reduces to:

$$\Delta\omega_G = 2\omega_G^0\gamma_G\epsilon \tag{1.16}$$

width $\Delta\omega_G = \omega_G - \omega_G^0$ the shift of the G-band frequency and γ_G the so called Grüneisen parameter[104]. Several techniques have been employed to apply controlled strain on nano-systems in order to extract the value of the Grüneisen parameter for graphene under biaxial strain[105, 106, 68, 107, 10, 108, 109]. Recent works of Metten et al. found a value of $\gamma_G = 1.8 \pm 0.2$ by measuring graphene nanobubbles[68]. A similar equation can be obtained for the 2D-band mode. In this case the measure value of the Grüneisen parameter by Metten et al. is $\gamma_{2D} = 2.4 \pm 0.2$[68]. Those experimental values have been used in the analysis of the following chapters when needed.

1.5.3 Probing doping effects in low-dimensional materials

As well as the previously mentioned mechanical effects, low-dimensional materials properties can be manipulated by the injection of charges[70, 95, 110]. Their remarkable electronic properties opened up a great number of opportunities for the construction of devices such are Field Effect Transistors (FET)[111, 112, 113]. The characterization of its electronic properties can however be challenged by their nanometric dimensions. Raman spectroscopy is once again an extremely versatile tool as it can probe readily electron-phonon[114, 115] and electron-electron[116] interactions.

We will focus in this section on the Raman response of graphene to probe charge injection as it will be of fundamental importance in future Chapter 4. Doping can occur in several ways as by the application of external electric fields[114, 115], by the introduction of chemical dopants [117, 118] as well as by the interaction

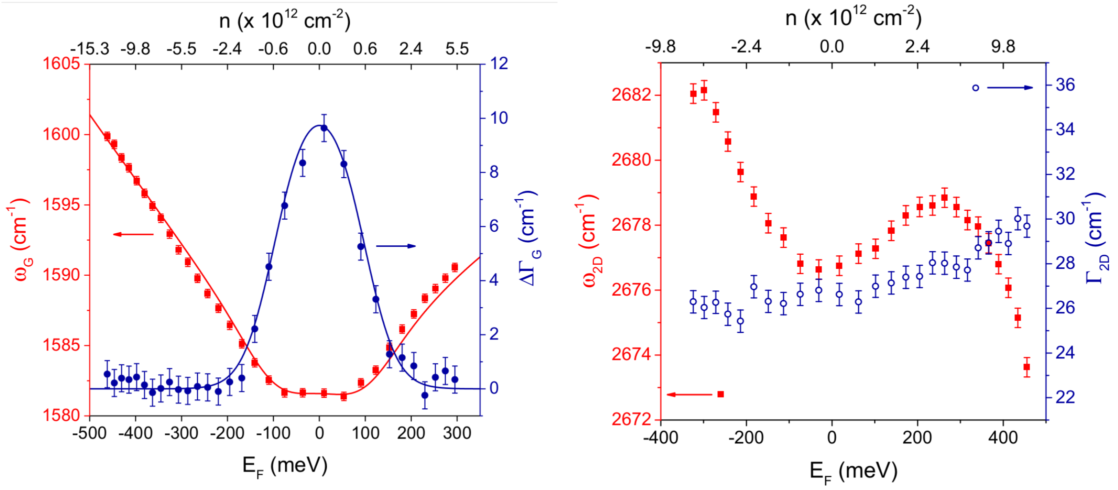

(a) **(b)**

Figure 1.15: Evolution of the (a) G-band and (b) 2D-band features with doping measured by Froehlicher et al[70]. Red markers indicate the evolution of the frequency. Solid blue markers in (a) show the shift of the FWHM from its lowest value while blue markers in (b) show the measured value of the 2D-band FWHM. Figure edited from [70].

with the surrounding atmosphere[119]. Due to the high sensitivity of graphene to its interaction with the environment its Raman response to external charge injection has been extensively studied. The most straightforward method is to create graphene transistors which can be used to reversibly inject both positive (holes) and negative (electrons) charges in a controlled manner[70, 120, 110]. Froehlicher et al. extensively exploited such devices to describe in details the evolution of the main Raman features of graphene i.e. the G and 2D bands[70]. The evolution of their features as a function of the charge density n or the Fermi energy E_F is shown in Figure 1.15. In Figure 1.15a we can see that the G-band frequency ω_G increases nearly symmetrically with respect to the zero charge Fermi level both for electron and hole doping. This anomalous behaviour was theoretically predicted by Lazzari and Mauri[121] and it was explained by a strong coupling of graphene's optical phonons at the centre of the first Brillouin zone with low energy electronic excitation. The shift of the FWHM of the G-band Γ_G with respect to the value for uncharged graphene, $\Delta\Gamma_G = \Gamma_G - \Gamma_G^0$ also is found to be symmetric with respect to holes and electrons doping. The G-band narrows with increasing charge density.

The 2D bands features, shown in Figure 1.15b are found to be less sensitive at low doping levels when compared to the G-band. Little to no variations are observed in the width of the peak Γ_{2D}. Its frequency shows a symmetric evolution with electrons and hole doping at low charge density, similarly to the G-band. When the charge is increased a strong softening is observed for hole doping.

1.5.4 Disentangling strain and doping in graphene

We showed in these last two section that the G and 2D bands features are largely affected by the present of both charge doping and external strain in graphene. The study of those features individually is, however, not sufficient to distinguish them when both the contributions are present at the same time. Lee et al. proposed a simple method for their disentanglement by correlating the frequency of the 2D-band to that of the G-band $\omega_{2D}(\omega_G)$ which is valid at low strain and doping levels[69]. For the strain contribution we have a linear dependency of the frequency of the two modes on the applied strain. From equation Equation 1.16 we obtain the shift of the G-band frequency when pure strain is applied. A similar equation can be obtain for the 2D-band by replacing γ_G for γ_{2D}. We can straightforwardly obtain the slope $(\partial\omega_{2D}/\partial\omega_G)^{strain}$ for pure biaxial strain of 2.2 ± 0.1 cm^{-1}[68]. In the case of doping the calculation of the slope of $\partial\omega_{2D}/\partial\omega_G$ is less immediate and it depends on the type of charge carrier. At low charge carrier densities ($\lesssim 5 \cdot 10^{12}$ cm^{-2}) we find a slope of 0.55 ± 0.2 for hole doping and 0.2 ± 0.13 for electron doping[70].

Each point in the $\omega_{2D}(\omega_G)$ plot can thus be decomposed into strain and doping contributions by projecting it into the non-orthogonal base formed by two unit vectors $\boldsymbol{e_T}$ and $\boldsymbol{e_H}$ ($\boldsymbol{e_e}$) parallel to the strain and hole doping (electron doping) evolution. We can see in Figure 1.16 an example of such a correlation plot. Two regions are clearly identified. Each set of points is parallel to the black dashed line indicating the presence of strain. Additionally the top right set of points can be described by a shift along the magenta dashed line as well as a shift along the black dashed line showing the presence of hole doping effects as well as strain.

For more details on the characterization through Raman spectroscopy of strain and charge doping, and the separation of the contribution of each effect, an extensive review article on the subject has been published by Bendiab et al.[73]. This disentangling approach will be employed in Section 4.3.4 of Chapter 4 for the study of the pressure evolution of suspended and supported bilayer samples in 4:1 Methanol:Ethanol.

1.6 High pressure application on low-dimensional systems

The role of pressure (P) as a tuning thermodynamic variable for low-dimensional systems is a field that is growing in interest in recent years. The sensitivity of those systems to the surrounding environment is strongly enhanced by pressure due to increased proximity between the atoms composing the various elements. The supporting substrate for the low-dimensional systems is a major element in direct contact with the sample. During compression it reduces in size and induces additional mechanical strain on the sample. A second element composing the environment is the so-called pressure transmitting medium (PTM). In a liquid or solid state this medium is used to transfer the pressure from our compressing device to the sample. By largely surrounding the sample it increasingly interact

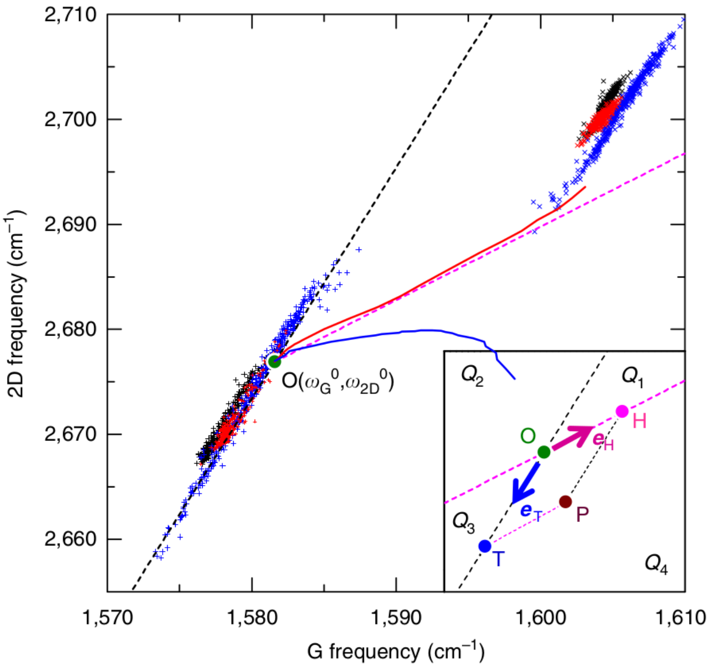

Figure 1.16: Raman mapping data measured by Lee et al. for a sample of graphene on Si/SiO$_2$ (+ symbols). After thermal annihilation at 400° the Raman mapping data from the same sample are represented by × symbols. The black dashed line models the correlation of the frequencies in the case of pure strain on the sample. Similarly the magenta dashed line shows the case for a purely hole doped graphene. In the inset an example of the decomposition of a point P in the correlation plot in the strain $\boldsymbol{e_T}$ and hole doping $\boldsymbol{e_H}$ base vectors. Figure taken from [69].

with it when pressure is augmented.

In this section we will introduce the state-of-art of recent discoveries in the field of high pressure experiments on low-dimensional systems. A major focus will be devoted to the the effects introduced by those two environmental elements.

1.6.1 Graphitic systems at high pressure

Two dimensional materials' response to high pressure is often dominated by biaxial strain effects introduced by the supporting substrate[45]. The G-band frequency shift with pressure $\partial\omega_G/\partial P$ is commonly used as a parameter for its measurement. Several studies have been performed on bulk graphite allowed to find slope values between 4.0 to 4.7 $\mathrm{cm}^{-1}\mathrm{GPa}^{-1}$ for the evolution of $\omega_G(P)$[122, 26]. Hanfland et al. also performed x-ray diffraction measurements in order to extract the bulk modulus β_0 of graphite along the crystallographic directions finding 35.7 and 1250 GPa for out-of-plane and in-plane bulk modulus[26]. As we already discussed in Section 1.5.2, another commonly used parameter that characterize Raman frequencies evolution with strain is the Grüneisen parameter γ. Alternatively to its definition in Equation 1.16 it can be expressed as[104]:

$$\frac{\omega(P)}{\omega(P_0)} = \left(\frac{V(P)}{V(P_0)}\right)^{-\gamma} \tag{1.17}$$

where $V(P)$ is the volume of the unit cell at a given pressure P and P_0 is the ambient pressure.

When studying two-dimensional systems the in-plane compressibility is orders of magnitude lower than the out-of-plane one. It is custom to define an in-plane Grüneisen parameter γ_G to study the G-band frequency shift as[48]:

$$\frac{\omega(P)}{\omega(P_0)} = \left(\frac{a(P)}{a(P_0)}\right)^{-\alpha\gamma_G} \tag{1.18}$$

with a the in-plane lattice parameter, $\alpha = 1$ for uniaxial compression and $\alpha = 2$ for biaxial compression and hydrostatic pressure. Hanfland et al.[26] found a value of 1.06 for the G-band frequency.

1.6.2 Environmental effects on the high pressure response of graphene and few-layer graphene

When reducing the number of layers towards monolayer graphene, the pressure response is strongly affected by environmental effects. Substrate play an important role on pressure induced strain transfer to few-layer graphene. Proctor et al.[48] et Nicolle et al.[44] performed layer dependent studies on samples deposited on $\mathrm{Si/SiO_2}$ substrates showing a strong dependency of $\partial\omega_G/\partial P$ on the number of graphene layers finding a shift for monolayer with values between $\sim$ 8 and $\sim$ 10 $\mathrm{cm}^{-1}\mathrm{GPa}^{-1}$. Figure 1.17a show the data obtained for one, two and few-layer graphene where we see that with an increasing number of layer we approach the behaviour of graphite.

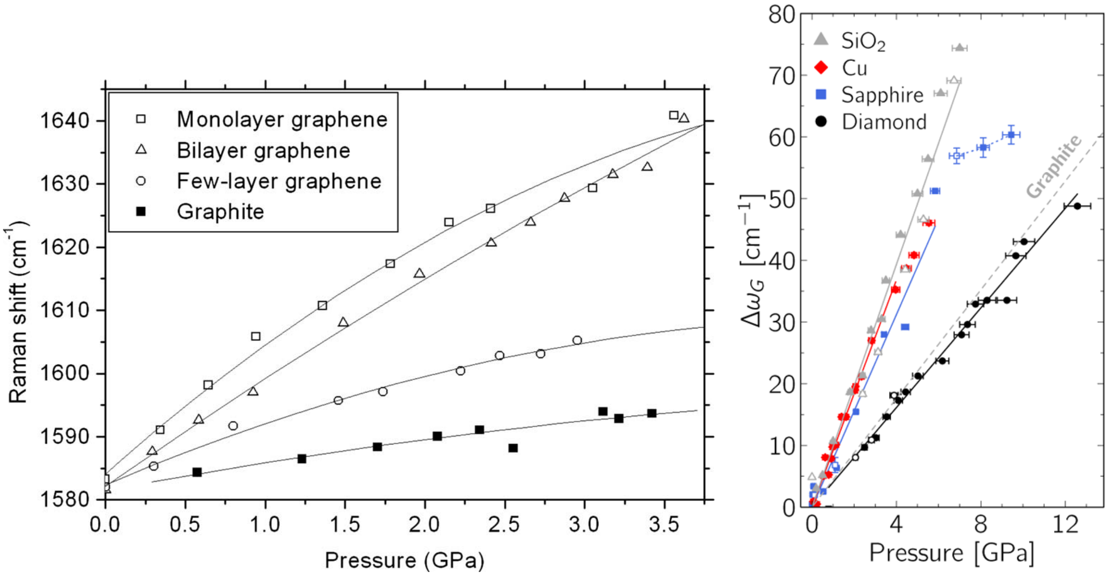

(a) **(b)**

Figure 1.17: Pressure evolution of the G-band frequency (a) as function of the number of graphene layers. Black lines are guides to the eye for the pressure evolution. (b) Evolution of the difference in frequency of the G-band with respect to its ambient pressure frequency $\Delta\omega_G = \omega_G(P) - \omega_G(P = 0)$ for different supporting substrates. The data are linearly fitted resulting in the shown solid lines. Figures taken from [48] and [45]

A large number of studies have been performed on samples deposited on Si/SiO$_2$ substrate but also several other substrates have been explored. Figure 1.17b show the results obtained by Bousige et al. for graphene deposited on different substrates[45]. We can see a strong dependence of $\partial\omega_G/\partial P$ on the substrate nature. This can be explained due to compressibility mismatch between different substrates and graphene introducing a strong biaxial component on graphene dominating over the hydrostatic pressure induced by the PTM. In addition to substrate compressibility Nicolle et al.[44], later confirmed by Bousige et al.[45], proposed that substrate-graphene adhesion is of high impact on the biaxial strain component governing the G-band pressure evolution. To take its contribution into account they introduced a phenomenological parameter which includes the contributions of both the strength of the Van der Waals interaction between graphene and the substrate as well as sample's geometrical modifications induced by the compressibility mismatch such as rippling and sliding.

The nature of the PTM also largely impact graphene's response to pressure. This can be due to both chemical interaction and the PTM's phase, whether it is in solid or liquid phase. Controversial results emerge from studies of whether the polar or apolar nature plays a role in graphene's doping effects with pressure. Filintoglou et al. studied the effect of two PTMs, polar 4:1 Methanol:Ethanol and non-polar Flurinert, on graphene deposited on copper substrates[123]. The authors found that in both cases strain transfer from the substrate is the dominating contribution to the pressure evolution of graphene G and 2D-bands excluding the hypotheses of eventual doping effects from the PTM. On the other hand Nicolle et al.[44] et Forestier et al.[34] found evidences of doping effects when comparing 4:1 Methanol:Ethanol to inert PTMs as Nitrogen and Argon.

A solid PTM or its solidification at a given pressure can largely impact the mechanical response of graphene. 4:1 Methanol:Ethanol is widely used as a PTM due to its high solidification pressure around $\sim$ 10.5 GPa and it is often used as a reference for the study of non-hydrostaticity effects. When solidification occurs a competition between biaxial strain due to the substrate and the solid PTM is established. The Raman features of graphene are impacted by the phase transition showing discontinuities at the PTM solidification both on the frequency and width of the modes. This behaviour has been reported on bilayer samples by Machon et al. using 4:1 Methanol:Ethanol, argon and water as PTM[36] and by Forestier et al. using 4:1 Methanol:Ethanol, argon and nitrogen[34].

The chemical and physical interaction of the PTM with graphene and graphene stacking play also an important role favouring pressure induced phase transitions. Graphite is a stable allotrope of carbon at ambient pressure and temperature. With increasing pressure a structural phase transition is induced towards a sp^3 hybridized phase. This transition has been observed in graphite for pressure above 10 GPa[26, 124] at room temperature. A widening of the G-band is observed associated with the beginning of the transformation. Balima et al. proposed a transformation towards a Z-phase of carbon corresponding to this transition[124]. In a similar fashion, the possibility of creating an sp^3 rich phase from graphene and few-layer graphene systems, often referred as 2D diamond or diamondene, drew major interest in the two-dimensional community. Pimenta Martins et al. proposed the first evidences of transition towards a 2D-diamond like phase using turbostratic bilayer graphene immersed in water as PTM[23]. Several other works are in agreement with the previous results highlighting how water plays a major role in the sp^2 to sp^3 phase transition[46, 125, 126]. In Chapter 4 we will propose novel experimental evidences on the characterization of the sp^2 to sp^3 transition as well as methods to tune and quench the transition. For further details we invite the reader to refer to Section 4.4.3 and Section 4.5.

1.6.3 Nanotubes at high pressure

The high-pressure behaviour of carbon nanotubes is a widely studied domain due to the very rich physics at relatively low pressure that has a high potential for applications. Their pressure evolution is characterized by pressure induced geometrical transitions that modify their circular cross section. The most common technique used to characterize the pressure evolution of carbon nanotubes with pressure is once again resonant Raman spectroscopy. Thanks to their unique band structure and density of states characterized by van Hove singularities it is possible to obtain great quality signal in high pressure experiments. G-band and RBMs are widely used as a probe for both mechanical properties and geometrical transitions with pressure. Several studies investigated the transition from the circular to flattened cross section of CNTs induced by pressure both from an experimental and theoretical point of view[41, 43, 42]. Torres-Dias et al. demonstrated that

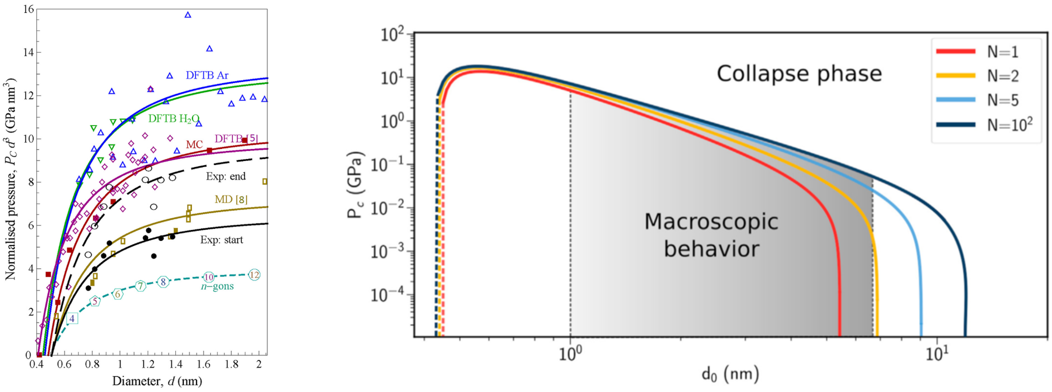

(a) **(b)**

Figure 1.18: (a) Experimental data and theoretical simulations showing the nanotubes' collapse pressure P_C for different nanotubes diameters d. (b) Phase diagram of the nanotubes collapse pressure as a function of the innermost diameter d_0 and the number of tube walls. Computed using a theoretical model taking into account for Van der Walls interaction a small diameters. In grey is highlighted the area where the tubes follow a macroscopic behaviour. Figures taken from [43] and [42].

the tube's collapse follow continuum mechanics predictions for big diameters and start deviating when approaching ~ 1 nm[43]. Radial collapse pressure P_C in the continuum mechanics limit is expected to follow a behaviour inversely proportional to the cube of the tube's diameter d as:

$$P_C = \frac{24D}{d^3} \tag{1.19}$$

Where D is the bending stiffness of the material. In order to take into account the divergence from the continuum prediction of Equation 1.19 at small diameters the authors proposed a modified collapse equation as:

$$P_C d^3 = 24aD(1 - \beta^2/d^2) \tag{1.20}$$

The phenomenological parameter β takes into account this deviation for small diameter. A second parameter a is introduced after the observation that the beginning and the end of the carbon nanotube's collapse is not instantaneous. a will take a value of 1 at the beginning of the collapse and 1.5 at the end. Figure 1.18a shows the agreement of the experimental and theoretical data with this law. Indirectly this study on carbon nanotubes allowed, using Equation 1.20, to determine an intrinsic parameter of graphene that is its bending stiffness $D = 1.7 \pm 0.2$ eV. Given the several experimental results and calculations present in the literature Magnin et al. proposed an unified phase diagram for the collapse of carbon nanotubes with pressure as a function of pressure, the number of tube walls and the inner tube's diameter[42]. Figure 1.18b shows the phase diagram obtained by Magnin et al..

The collapse of carbon nanotubes with pressure will be the object of Chapter 3. In Section 3.1 we will provide further details on the characterization methods to probe carbon nanotubes collapse.

1.7 Summary

In the present chapter we introduced the theoretical background and the state of art at the core of the understanding of the physical phenomena involved in carbon based low-dimensional systems at high pressure. By breaking down the atomistic description of the crystallographic structure of graphene, graphene stacking and nanotubes we could thoroughly describe the electronic and vibrational structures of those systems.

Using those theoretical concepts we could detail the underlying mechanisms that describe the functioning of Raman spectroscopy and its application in the study of low-dimensional material. This spectroscopic technique has indeed been the most fruitful probe throughout the totality of my work applied on my studies of carbon nanotubes (Chapter 3) and two-dimensional carbon materials (Chapter 4).

Furthermore, we showed how the properties of low-dimensional systems can be manipulated by external factors. The surrounding environment as well as external fields can be used to manipulate the crystallographic and electronic structures. Raman spectroscopy has been proved to be highly efficient in detecting the variations associated to it so we introduced the main scientific contributions, principally on 2D carbon materials, that helped designing the experiments and interpret the results in Chapter 4.

The last section, was dedicated to the state of art of high pressure experiments on two-dimensional systems. We firstly introduced the useful quantities that interconnect the compression of the materials to their Raman response. Following, we centred the discussion on two-dimensional materials by describing the principal studies on graphene and few-layer graphene at high pressure. Major attention was dedicated to the environmental effects that strongly affect the physical properties of two-dimensional materials. In high pressure experiments, two major elements are in mutual interaction with graphene which are the substrate and the PTM. The effects of each of these elements have been explored by several studies but a large number of questions still remain unsolved. Our experiments in Chapter 4 dived straight into those topics and by interchanging different substrates and PTM we obtained a deeper understanding of the rich physics the is involved in the environmental-mediated pressure response of two-dimensional materials. At last, we focused on previously reported studies on the pressure response of carbon nanotubes. The state-of-art on the physics of the geometrical transition of carbon nanotubes from their circular to the flatten cross section was introduced. In Chapter 3 we studied this transition in detail introducing novel spectroscopic signatures for its identification.

In order to perform our experiments I dedicated part of my work to technological developments that allowed to obtain the results of Chapter 3 and Chapter 4. In the following chapter we will describe those developments as well as introducing the necessary supporting experimental devices used for the experiments.

Chapter 2

Experimental Techniques

In the present chapter we will discuss about the main technologies required to perform the experiments carried out during my PhD.

The first part of the chapter will be dedicated to high pressure devices. We will begin in Section 2.2, after a short introduction, with the description of the main components and the functioning principles of the diamond anvil cell. This compression device has been used in the majority of the experiments of this work to apply pressure on the samples.

Beside diamond anvil cells, sapphires anvil cells have been largely used to perform the high pressure experiments on carbon nanotubes which are detailed in Chapter 3. In Section 2.3 we will introduce the advantages and drawbacks associated with their use. Then we will present the sapphires characterizations and adjustments of the experimental procedure I performed which allowed to increase the pressure limits of those cells.

In a second part of the chapter we will focus on the developments I carried out for the preparation and characterization of low-dimensional materials. In Section 2.4.1 we will describe the upgrades I made on the transferring system and procedure for the fabrication of 2D materials. Moreover, for the characterization of samples I developed, with the help of PhD student Max Gerin, a software for integrating automated mapping of samples into our custom Raman spectrometer. The description of the Raman set-up as well as the operating principles of the software will be the object of Section 2.4.2.

2.1 Introduction

The theoretical and bibliographical introduction developed in the previous chapter granted us with the necessary fundamental groundwork for the interpretation of the rich palette of phenomena involving low-dimensional systems at high pressure. In what follows, we will describe the technological developments that allowed for their study and interpretation. The need for dedicated technologies arises from several challenges introduced by both the complexity of high pressure experiments as well as the reduced size of low-dimensional systems. High pressure technologies often require to work in reduced spaces limiting both sample accessibility, handling and size. Furthermore, the sample area is enclosed in a chamber-like space enveloped in several layers of materials which need to be crossed when probing the samples. This limits the available usable characterization techniques as well as partially deteriorates and lower the sample signal. For what concerns the low-dimensional systems, the difficulties are often related to handling issues, fragility and low optical contrast. This results in the need for dedicated techniques to transfer them from their production site into the high-pressure devices. Moreover being composed of mainly surface atoms makes them extremely sensitive to the surrounding environment which, in high pressure experiments, is characterized by the PTM and the substrate. Their accurate choice and engineering can largely simplify the interpretation of experimental data as well as induce secondary phenomena. Finally local inhomogeneities in the environment and the sample are enhanced in those systems resulting in fluctuations in the sample response. Automated scanning systems allow to probe local properties of the sample and access high-statistic analysis tools.

In order to overcome those difficulties I developed several dedicated devices and software. In the following we will introduce those advancements separating the discussion treating independently the technologies directly involving high-pressure techniques and those concerning handling and characterization of low-dimensional materials.

2.2 High pressure technologies

A wide range of devices have been developed throughout the last century for the generation of pressure since the pioneering works of Bridgman at the beginning of the 20th century. Each technology is designed for specific needs and has advantages and limitation. Among all, the most outstanding device is the diamond anvil cell (DAC) which is predominant due to its possibility to extend the range of achievable compression pressure to outstanding values in the megabar range[127, 128, 129].

Its functioning principle includes two separate blocks featuring opposing diamonds anvils at the extremities as shown schematically in Figure 2.1. In order to transfer pressure to the sample a small compression chamber is created interposing a gasket between the anvils. The latter is essentially a metallic disk where a central circular hole is drilled in order to open up the compression chamber which is sealed between the anvils as shown in the close up in Figure 2.1. The anvils deform plastically the gasket reducing the size of the compression chamber, increasing the density of the pressure transmitting medium (PTM) i.e. the medium that fills the compression chamber, thus increasing the pressure inside the chamber. Before drilling the gasket a pre-indentation is performed in order to increase the gasket hardness and stability, and to provide additional support to the anvil reducing the risks of anvil failure[130]. The choice of the amount of pre-indentation is a balance between the maximum pressure attainable and sample size restriction. Dunstan recommends an initial thickness of the indented gasket of $\sim d_c/10$ with d_c being the culet (the diamond flat facet in contact with the gasket) diameter[130]. The choice of the hole diameter also has an optimal value which is recommended to be $\sim d_c/3$[130].

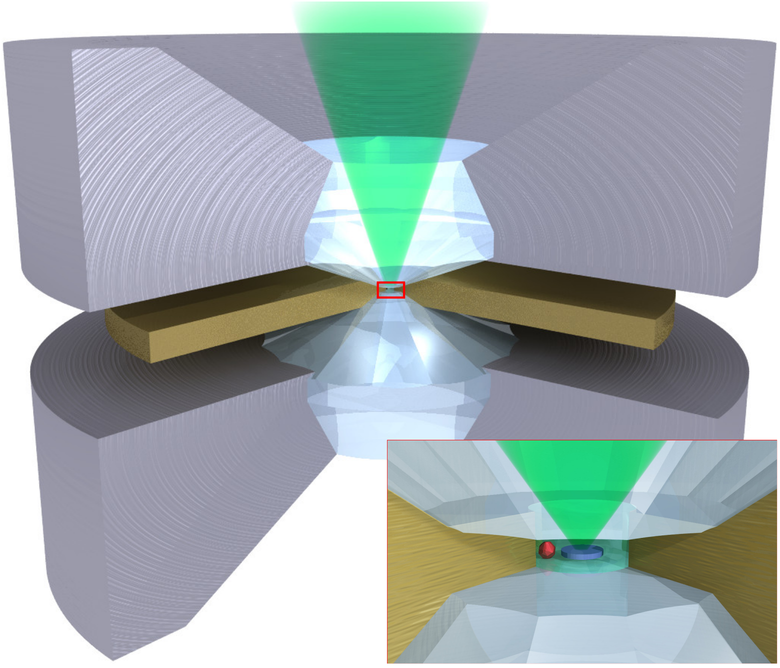

Figure 2.1: Schematic representation of the DAC. The anvils compress the central brown disc representing the metallic gasket. The laser (in green) reaches the sample through the top optical window of the DAC and the diamond. In the inset a zoom of the gasket cavity (red rectangle in the larger view) shows the compression chamber where a red sphere represents a ruby chip and the disk a schematized sample.

(a) **(b)**

Figure 2.2: (a) Front and (b) top views of the gas supply device used for inflating the DAC membrane. The set-up is connected to a small gas bottle fill with helium with a maximum pressure of 150 bars.

In order to achieve extremely high pressures the diamond culet is polished to have very small surfaces allowing to reduce the external load that needs to be applied on the anvils. External forces can be applied using several methods including screws, hydraulic and pneumatic systems. The latter is the most commonly used method in our laboratory and it has been used in all the experiments of this work. It uses a pumping cylinder that injects helium gas into an inflatable membrane. The latter is in contact with one of the two cell blocks which is free to move and is pushed towards the other fixed part applying the desired pressure. Figure 2.2 shows the gas supply apparatus used for our experiments.

Using a helium gas-driven pneumatic system has several advantages. To begin with, a high degree of control on the pressure value is possible thanks to the possibility of finely regulate gas injection rates whilst measuring *in-situ* pressure. Moreover, in order to apply extremely high pressures on the sample only a relatively moderate gas pressures is necessary. Typically, to reach *in-situ* pressures of the order of hundreds of kbar only tenths of bars in the membrane are necessary. In the following we will refer to *in-situ* pressure to talk about the sample pressure inside the gasket hole and membrane pressure for the pressure applied from the pneumatic system.

To withstand such extreme pressures only the hardest material can be used for the fabrication of the anvils so the most commonly used material is diamond. Diamond is among the hardest materials known to date and it is fairly available in its synthetic and natural forms. Furthermore it is transparent in the whole visible range and partially in the infrared, ultra-violet and x-ray regions. This makes it compatible to a large number of optical spectroscopy techniques as well as it allows for *in-situ* sample observation with simple optical microscopy techniques. Beside diamond several other *gems* are used as anvil materials in the so-called gem anvil cell (GAC). Those will be further discussed in Section 2.3 with special focus on sapphire anvil cells.

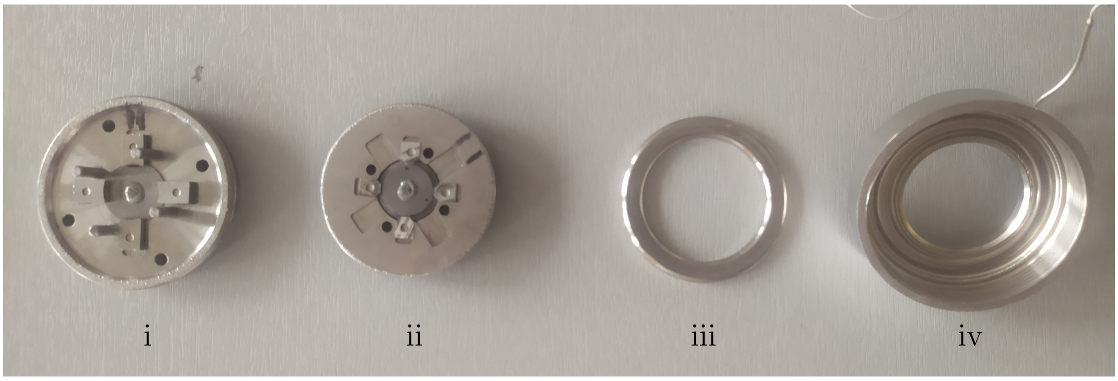

(a) PROXIMA

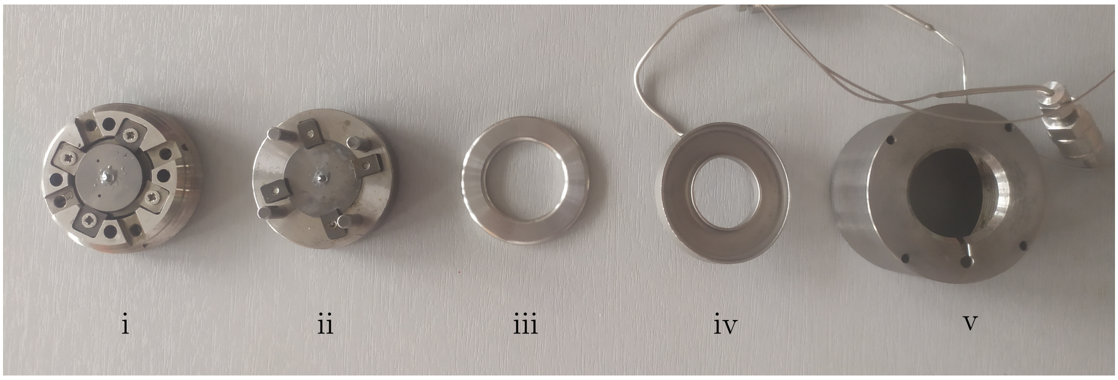

(b) Letoullec

Figure 2.3: Two DAC models used in the experiments. The DACs components are taken apart to identify the different components: (i) bottom fixed block including one of the anvils; (ii) top mobile anvil part of the DAC; (iii) smoothen up round disk for avoiding membrane damaging; (iv) inflatable membrane; (v) threaded cap used to fix the bottom part of the anvil in the Letoullec model (integrated with (iv) in the PROXIMA model).

2.2.1 Diamond anvil cell designs

The choice of the cell design is of great importance when planning an high pressure experiment. A vast number of models are available both commercially and as prototypes which are conceived to accommodate broad and specific experimental needs. Among all, we find cells adapted for low and high temperatures, magnetic field measurement, x-ray diffraction and ultra-high pressure. Throughout this work two models have been used which are the commercially available Letoullec design (Figure 2.3b) and the PROXIMA design (Figure 2.3a), developed in the laboratory. The two models include common parts as the previously mentioned main blocks on which the anvils are glued (i,ii) and the inflatable membrane (iv). A smooth rounded ring (iii) is added between the membrane and the anvil to avoid piercing of the membrane due to the sharp cell edges. An additional cover (v) is necessary to lock the cell after mounting in the Letoullec model while that was merged with the membrane in the PROXIMA case. The substantial difference in applications between the two model is given by the improved optical window introduced in the PROXIMA design. This ultra-flat cell has been engineered for allowing a very short working distance. Meanwhile, a wide optical opening allows for light collection at very high scattering angles. It is thus suitable for high numerical aperture and magnification objectives resulting in an improved spatial resolution and enhanced signal collection efficiency. A modified Mitutoyo 100x magnification objective with 0.7 NA has been implemented to further ameliorate sample probing. The latter has been conceived with a correction for the spherical aberrations introduced by the diamond in the optical path ulteriorly improving signal collection and resolution. The combination of the Mitutoyo objective and the PROXIMA cell has proved its efficiency in the work of Medeghini et al. who found a sub-micron spatial resolution at high pressure[20].

The PROXIMA cell has however a downside introduced by the ultra-thin design. The reduced dimensions and weight partially compromise its response to the high mechanical loads. Finite elements simulations estimate the capability of the cell to reach just above 10 GPa, limiting the maximum pressure attainable. For experiments that needed to go beyond this limitation the Letoullec cell has been preferred. This cell has a more *general purpose* design that allows to reach pressures of several tenths of GPa. Whilst it is not possible to use the diamond-corrected Mitutoyo objective, acceptable spatial resolution can be achieved using standard long working distance x50 objectives. This cell has also been used when anvil materials different to diamond were used.

2.2.2 Ruby fluorescence for pressure measurement

After the description of the devices that allow to reach extremely high pressures we will talk in this section about how such pressures can be measured in an experiment using a DAC. Two methods are mainly used for reliable and calibrated results which are the x-ray diffraction measurement of a pressure marker for which the pressure-volume relationship is well known and the fluorescence of electronic transitions related to ion impurities in a crystal structure[131]. Whilst they both give accurate measurements, the advantage of using the fluorescence method is

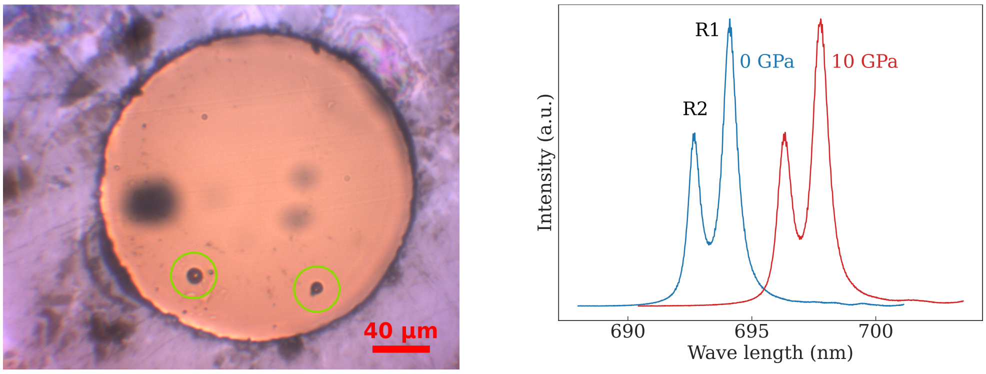

(a) **(b)**

Figure 2.4: (a) Top view of the gasket hole showing two rubies circled in green. The typical luminescence spectrum of ruby is shown at room pressure and at 10 GPa in (b).

that it is fast, easy and only needs equipment readily available in the majority of laboratories. We have thus used this method for our experiments.

For the vast majority of experiment the most suitable crystal is chromium-doped sapphire (Cr^{3+} doped Al_2O_3), also known as ruby. Rubies can be produced in little spheres of few microns in diameter so they easily fit inside the DAC without compromising the sample space. Figure 2.4a show an example of a DAC loaded with two rubies. The chromium impurities are responsible of the ruby fluorescence, with two close emission lines in the red part of the visible spectrum (at ambient pressure and temperature) named R_1 and R_2 (in blue in Figure 2.4b). The frequency of those line are dependent on the surrounding electric field produced by the crystal's ion, O^{2-} in the case of sapphire. Pressure application acts on the crystal approaching the ions, perturbing the field and modifying the absorption and emission properties of the ruby crystal. This result in a shift of the frequency of the R_1 and R_2 lines with pressure[132]. In red in Figure 2.4b is shown a ruby fluorescence spectrum taken at 10 GPa where a clear red shift in frequency is noted compared to the ambient spectrum.

This shift has been calibrated throughout the years against pressure markers measured by x-ray diffraction. The wavelength of the R_1 ruby line λ is found to follow the equation below at a given pressure P[131]:

$$P = \frac{A}{B}\left[\left(\frac{\lambda}{\lambda_0}\right)^B - 1\right] \tag{2.1}$$

where A and B are parameters obtained from fitting the experimental data and $\lambda_0 = 694.24\,\text{nm}$ is the value of the frequency of the R_1 ruby line at ambient pressure (at 298 K). The most recent scale calibration extended the validity of the ruby method to 150 GPa finding values of $A = 1876 \pm 6.7$ and $B = 10.71 \pm 0.14$[131].

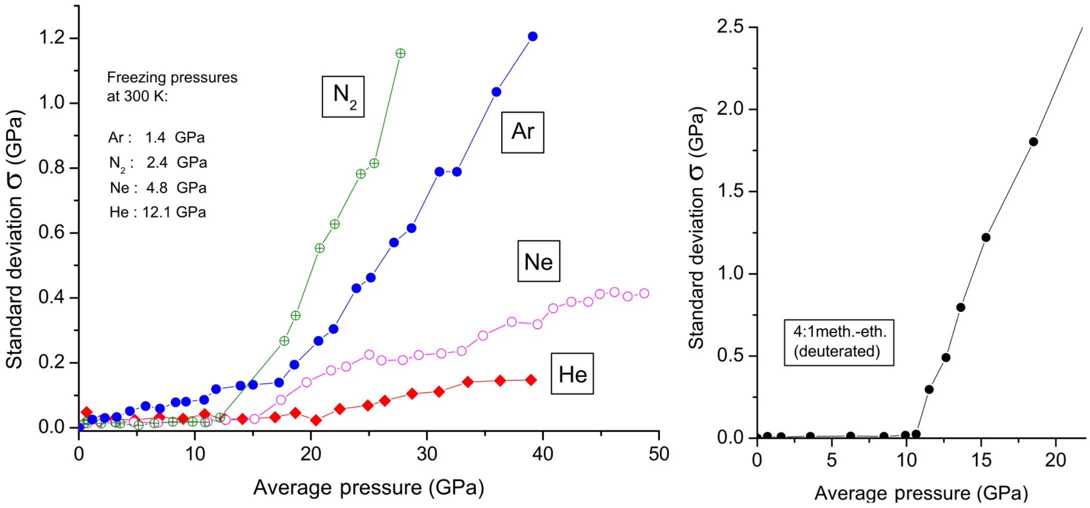

(a) **(b)**

Figure 2.5: (a) Comparison between the standard deviation of the ruby measured pressure σ in high pressure experiments dedicated to find the hydrostaticity levels of rare gasses and nitrogen. (b) σ values obtained for 4:1 Methanol:Ethanol PTM. Figures taken and adapted from [133].

2.2.3 Hydrostaticity limits of pressure transmitting media

In previous section Section 1.6.2 we introduced the role of the pressure transmitting medium (PTM) as a major player in governing low-dimensional systems' response to high pressure. It can interact both from a physical and chemical point of view. It is thus essential to choose the most adapted PTM for each experiment in order to explore different properties of the low-dimensional materials.

Hydrostatic limits are one of the very first things to take into consideration when choosing the PTM for an experiment. Every medium undergoes a solidification phase transition with pressure at a given point when its density is such that an organized structure becomes more favourable than a liquid or gas phase. The pressure at which it occurs depends on the chemistry of its building blocks. A solid medium has non-zero shear strength in opposition to liquid media which have zero shear stress (we refer respectively to non-hydrostatic and hydrostatic pressure for the two cases). This can induce non-homogenous pressure gradients on the sample resulting in damaging, tearing, local difference in the physical response, and inducing or preventing phase transitions. Ideally, hydrostatic conditions are preferred but they are not always achievable for experimental reasons. In order to characterize the *level* of hydrostaticity the most commonly used method is to put several rubies loaded into a DAC. Measuring the standard deviation of the pressure measured by the rubies σ gives a *scale* to compare the hydrostaticity of different media.

The leading PTM in terms of hydrostaticity is undoubtedly helium. It is liquid up to a pressure of 12.1 GPa[133] with almost no increase in the rubies standard deviation up to 23 GPa[133]. After that a mild linear increase is observed. Other inert gasses also show great quasi-hydrostaticity properties with neon being the second best PTM in term of hydrostaticity at very high pressure. It solidify at 4.8 GPa showing values of σ almost unaffected up until 15 GPa[133]. Despite their excellent properties those two PTMs need fairly complicated procedures for their loading and dedicated equipment not always available. Other room pressure gasses like argon and nitrogen are inexpensive and can be loaded easier than the previous PTMs, still preserving good quasi-hydrostaticity properties at high pressures. They solidify at respectively 1.4 GPa and 2.4 GPa with nitrogen showing the first pressure gradients in the standard deviation above 10 GPa. Figure 2.5a shows a comparison of the evolution of σ with pressure for those PTMs[133]. Nitrogen was used in the experiments on carbon nanotubes at high pressure in Chapter 3 because of the clearness of the Raman spectrum which does not majorly polluted the signal of the sample.

Beside ambient pressure gasses several liquids and liquid mixtures are also used as PTMs. In particular a mixture of methanol and ethanol in a 4 to 1 ratio (4:1 Methanol:Ethanol) is the most commonly used PTM. It is easy to load with no need for additional equipment and its two ingredients are readily available in the majority of laboratories at high purity levels. Moreover, it has a high solidification pressure at room temperature of 10.5 GPa. Above this pressure the values of σ increase steeply but remain similar to other ordinary PTMs[133]. This PTM was widely used in the experiments described in Chapter 3 and Chapter 4 to study samples in hydrostatic conditions below 10.5 GPa.

Water is also seldom used as PTM and very few studies are available about its hydrostaticity. Piermarini et al. reported very low pressure gradients using this PTM above 10 GPa despite the low solidification pressure of ~ 1 GPa[134]. A second transition solid to solid between the phase ice VI to ice VII also occurs at ~ 2 GPa. The use of water played a central role in our study on the pressure induced phase transition from few-layers graphene to diamondene so it has been used as PTM in our experiments in Section 4.4.3 and Section 4.5.

2.3 Sapphire anvils for the study of carbon-based systems

In the previous section we introduced the working principles of the diamond anvil cell to perform high pressure experiments. In particular we described in detail the advantages of the use of diamonds as anvil materials but mentioning that several other materials also are used for their fabrication. Whilst being superior in hardness they might not be suitable for all the high pressure applications as their presence might interfere with the sample signature we want to study. We mentioned that diamond has great optical transparency in the visible range but it becomes opaque in the ultraviolet with a band gap of 5.4 eV[135]. Diamond is thus not suitable for UV spectroscopy studies at high pressure. Its Raman spectrum also shows two major features in its spectrum as shown in Figure 2.6. In particular its first order Raman feature is found around 1334 $\text{cm}^{-1}$and being strongly present in high pressure experiment is a limiting factor when studying sample signals close to this frequency. In our case, the sp^2 based low-dimensional materials show a

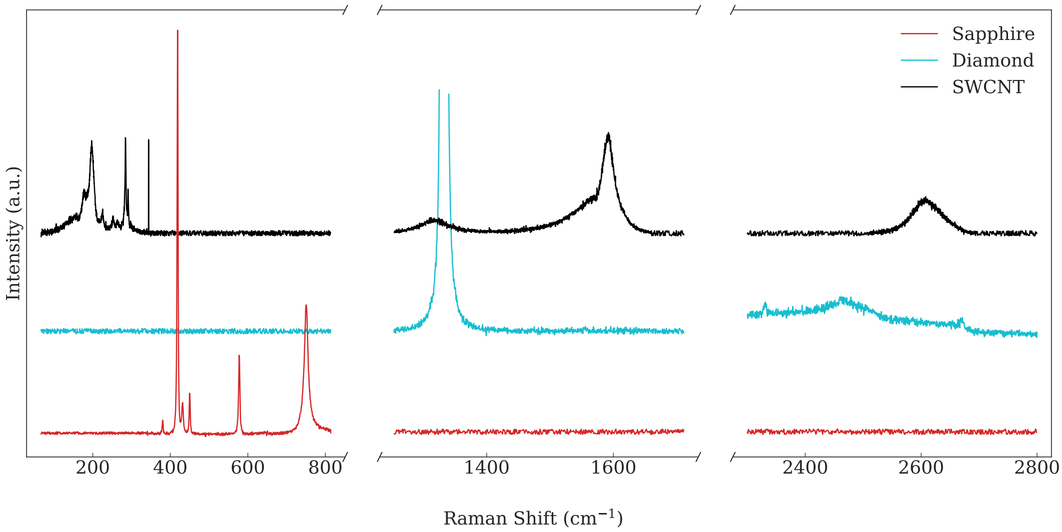

Figure 2.6: Background subtracted spectra of the different anvils' spectra compared to SWCNTs spectrum. Only the lower part of the diamond first order peak around 1334 cm^{-1} has been shown for easing the plots visualization. The spectra intensities have been adapted to resemble experimental conditions.

Raman feature between 1320 cm^{-1} and 1350 cm^{-1}, the D-band. This band is fully masked by the intense first order peak of diamond up to $\sim$ 10 GPa when, due to a higher pressure coefficient of its frequency compared to the diamond's peak, is recovered. Figure 2.6 also highlights this overlap comparing the typical Raman spectrum of SWCNTs with that of diamond at ambient pressure. The evolution of the D-band with pressure in SWCNT was the core assumption for the results obtained in future Chapter 3 so we explored the use use of gems instead of diamond as anvil materials allowing us to perform those studies.

A commonly used alternative as anvil material is sapphire. Its hardness, despite being lower than diamond's one, has a value of 9 on the Mohs scale of hardness (for comparison diamond has a value of 10, the highest on the scale, and hardened steel 7-8). It has excellent optical properties with extended transparency in the UV due to its large bandgap of $\sim$ 10 eV. In Figure 2.6 we can see that the Raman peaks of sapphire fall in a region where there are no signatures of the SWCNTs making sapphires a perfectly suitable anvil material for our studies. From now on we will talk about Sapphire Anvil Cell (SAC) to refer to an anvil cell using sapphire anvils.

In the following sections we will describe the difficulties encountered associated with the choice of using a SAC and the improvements to the methods that allowed us to extend the pressure range they can achieve.

2.3.1 Sapphire anvil failures

Very few studies are present in the literature about the use of sapphire anvils reaching high pressures. The only reported cases of measurements above 5 GPa

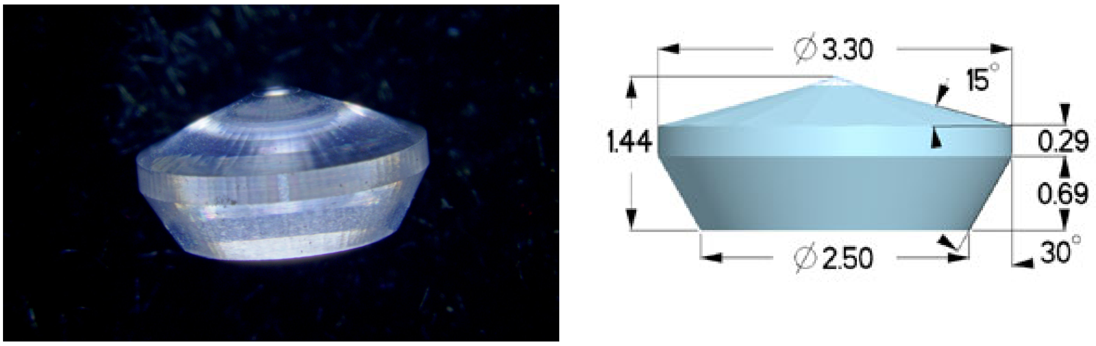

(a) **(b)**

Figure 2.7: (a) Optical image of the Almax-Boehler cut sapphire anvil and (b) its schematic representation and sizes (lengths are expressed in mm).

are from Xu et al. and one from Furunu et al. where they reached 7.8 GPa[136], 14 GPa[137], 24 GPa[138] and 25.8 GPa[139] in not very detailed experiments that mostly aimed to test the SAC limits. To reach the highest pressures single bevels anvils were used. The sapphire anvils used in our experiments have a Almax-Boehler cut with culet sizes of 500 µm which have been purchased from Almax Easylab. We can see an image of one of the anvils in Figure 2.7a and a schematic including the anvil dimensions in Figure 2.7b. Those anvils are designed to withstand pressures of around 6-7 GPa.

Our first attempts to use the anvils concluded in the anvil failure at much lower pressures than the nominal one. This happened both during the indentation process and the experiments. Due to the lack of literature and the little usage of those anvils in our laboratory an exploratory study has been necessary in order to achieve higher pressure using the SAC. In Figure 2.8 are shown two sapphires that broke during the indentation (a) and in a high pressure experiment reaching 2.9 GPa (b). The membrane pressure was in the two cases 46 bars and 34 bars.

From those two sapphire failures we drew two substantial conclusions:

- Indentation is an extremely critical phase where the sapphire is submitted to high tensile stresses. Spain el al. claim, for the diamond's case, that an anvil break more likely during indentation than during a high pressure run[140].
- The anvil might present misalignment, defects or residual stresses from fabrication and polishing which may lower their quality and lead to breaking before attending the nominal pressures

We will tackle those two aspects in the following two sections.

2.3.2 Characterization of the sapphire anvils: defects, strain and orientation

In order to characterize the presence of defects in the anvils several techniques are available, the first being simple observation. Defected sample may show, as

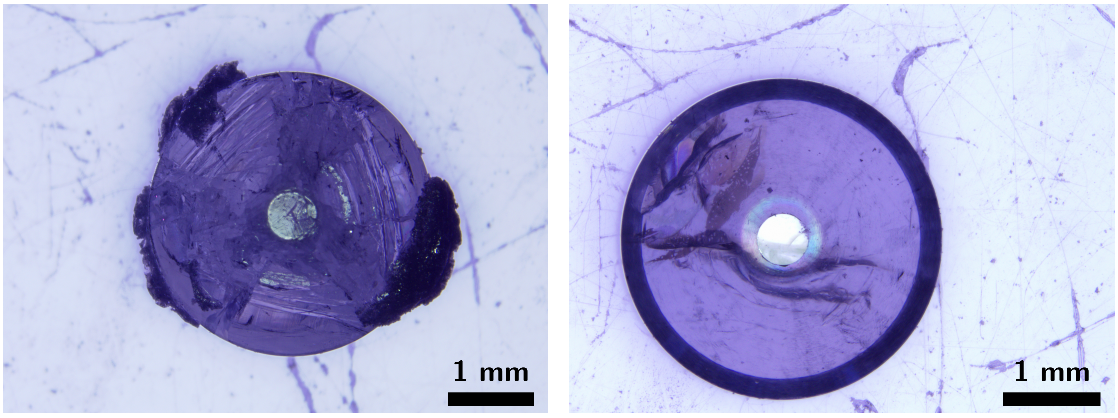

(a) S1 **(b)** S2

Figure 2.8: (a) Sapphire anvils broken during the indentation phase at a membrane pressure of 46 bars and (b) in a high pressure experiment reaching 2.9 GPa (membrane pressure of 33 bars).

well as evident signs of inhomogeneities and defects, the presence of micro-bubbles that can be an indicator of inadequate production processes[141]. Our anvils however did not show any visual imperfections under close inspection using optical microscopy. Spectroscopic techniques can then be used to extend the visual observation to the atomic scale in order to verify the presence of residual strain and structural defects. Raman spectroscopy is a direct indicator of the presence of residual strain in the crystal as the latter can shift the frequency of the vibrational modes. In sapphire the A_{1g} mode is considered a good indicator and it is often used for its characterization[141]. The downside of this technique is that it only probes locally the sample and the induced frequency shift can be of the order of the spectrometer resolution. Another technique that involves the use of X-ray diffraction is the Rocking curve imaging. The latter is a measurement of width of the diffraction peaks that can be caused by Mosaicity (misorientation of crystallites) and strain. In sapphire it has been shown to be a good indicator of the crystal quality[142].

Those spectroscopic techniques, despite being powerful, can be extremely time consuming due to the need for long acquisition, post processing and analysis, and accessibility of the instruments. They have been briefly explored without giving significant results confirming or rejecting the possibility of using those techniques for the characterization of the sapphire anvils due to the lack of statistics (data and analysis not included in this thesis). Further experiments and more detailed analysis would be needed to exploit the maximum capacity of those techniques (also breaking more sapphires would help but it is not advised).

Beside the previously described techniques that aimed to detect the presence of defects and residual strain to characterize the crystal quality, identifying the crystal orientation relative to the compression axis also plays an important role in the task of reaching higher pressure. Sapphire is a non-isotropic crystal which has the trigonal (rhombohedral) crystal structure shown in Figure 2.9a. It has equivalent length lattice vector for two a and b direction and a third non-equivalent orthogonal

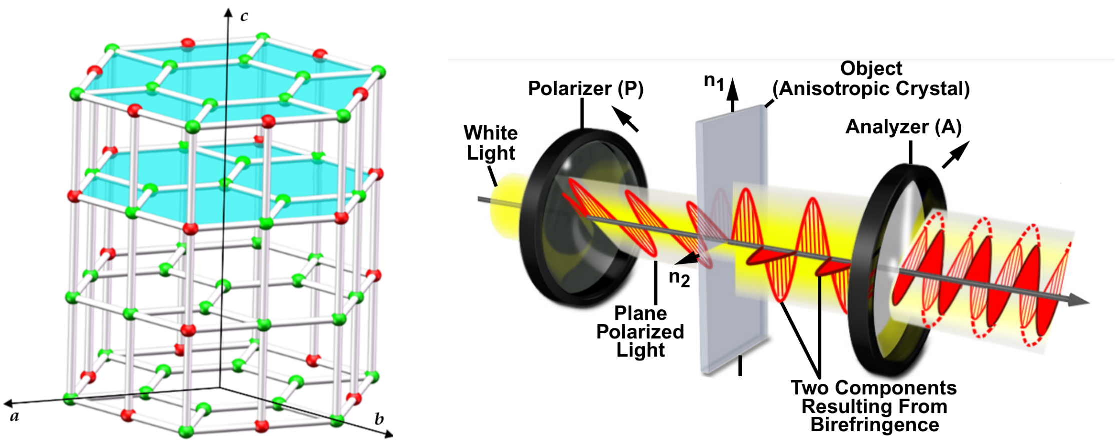

(a) (b)

Figure 2.9: Model of the crystallographic structure of sapphire (a). The black arrows show the crystallographic axis. (b) Schematics of the set-up used to perform the cross polarisers measurements. The red sinusoid shows the components of the electric field with the line-filled and solid-filled curves representing respectively the ordinary and extraordinary rays. Figures edited from [143] and [144].

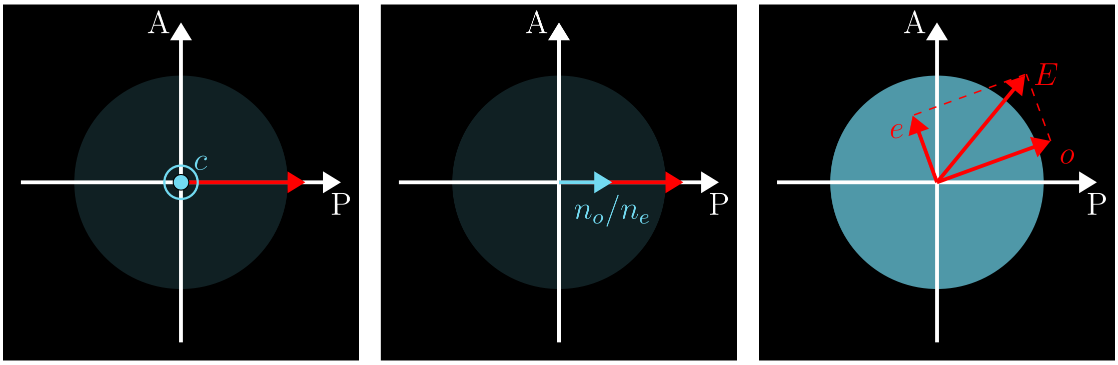

(a) (b) (c)

Figure 2.10: Top view of the crystal as seen through the microscope in the cross polariser experiment. The arrows labelled with **P** and **A** indicate the polariser and analysed transmission azimuth. The central blue circle represents the crystal. Increasing light intensity passes through the analyser is shown by brighter blue circles (the first two images where the crystal is totally extinct still shows a small portion of light for the reader visualization of the crystal's position). Red arrows show the polarization direction of the light rays crossing the crystal. Three cases are shown: (a) the optical c-axis is vertical so the crystal behaves as an isotropic crystal and the light is blocked by the analyser; (b) the polariser is parallel to the projection of one of the refractive index direction in its plane so once again the polarization is not altered and the crystal will appear as dark as the background; (c) at intermediate angles the crystal will generate an ordinary (o) and extraordinary (e) rays which result in the total field E. As E has a component in the **A** direction the light will cross the analyser and arrive to the objective.

c-axis, which is called the optical axis. Due to its anisotropy it shows birefringence for incident light rays that are not parallel to the c-axis. This axis is thus preferred for optical applications. It is also more resistant to rupture compared to several other orientations[145] so it is the best candidate for the construction of sapphire anvils. We decided for those reasons to investigate the crystallographic orientation of our anvils before gluing them to the SAC in order to reduce the possibility of failure due to a weak crystallographic direction of the anvil cut.

A quick and effective solution to verify if a crystal is aligned parallel to an isotropic plane is to use two crossed polarisers. This technique uses the fact that the light crossing through a non-isotropic crystal plane will rotate the light polarization while it will remain unaffected in the case of an isotropic one. Figure 2.9b show a schematic of the set-up used to perform this measurement. Interposing the crystal between two parallel crossed polariser (polariser and analyser) and sending unpolarized light through will allow us to distinguish if the crystal is aligned with an isotropic plane parallel to the polarisers or not. An objective is placed parallel to the system axis, at the opposite end of the light source, to visualize the crystal.

The origin of this polarization rotation reside in the fact that anisotropic uniaxial crystals, like sapphire, are described by two refractive indexes n_1, n_2, one along the optical axis and one orthogonal. When light enter an uniaxial crystal propagating parallel to the optical axis it will behave as if it was crossing an isotropic crystal. However, when it enters along any other direction it splits into two rays travelling at different velocity and with polarization at right angle. Those two rays are called ordinary and extraordinary rays which are schematically shown in Figure 2.9b by the red sinusoids at right angle after the crystal. We will distinguish three cases:

1. The crystal is placed such that the optical axis is orthogonal to the polarisers' plane: the light will be blocked by the crossed polarisers as the crystal will not affect the light polarization. The crystal will appear as dark as the background. Figure 2.10a shows schematically this configuration;

2. The crystal is placed such that the crystal's optical axis is parallel or perpendicular to the polariser transmission azimuth: the polarized light arriving to the crystal will travel feeling only one velocity (either ordinary or extraordinary) so the polarization will not be rotated. The analyser will block the out-coming light so the crystal appears dark as shown in Figure 2.10b.

3. The crystal is oriented with the optical axis in the polariser plane at an oblique angle with respect to the polariser transmission azimuth: the vector sum of the ordinary and extraordinary rays' polarization will have a component parallel to the analyser so light will arrive to the objective (Figure 2.10c).

In order to not get mistaken misjudging the case 2 with an isotropic axis (case 1), the crystal is rotated several times. Anisotropic planes will show a four-fold light transmission pattern.

Figure 2.11 shows the optical images obtained applying this procedure to two of our anvils. In the case of a misalignment between the optical c-axis and the anvil

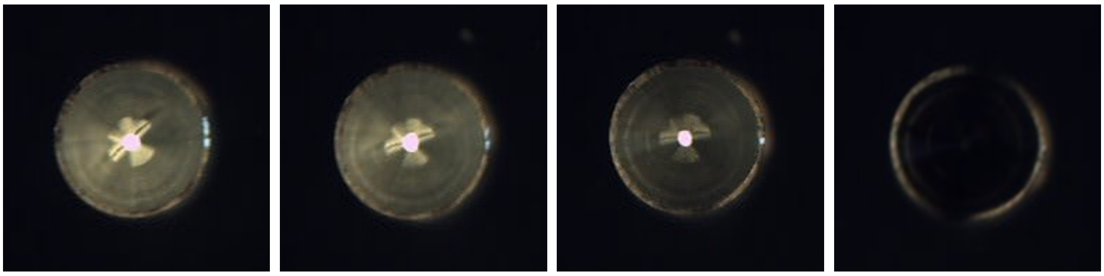

(a) Randomly oriented

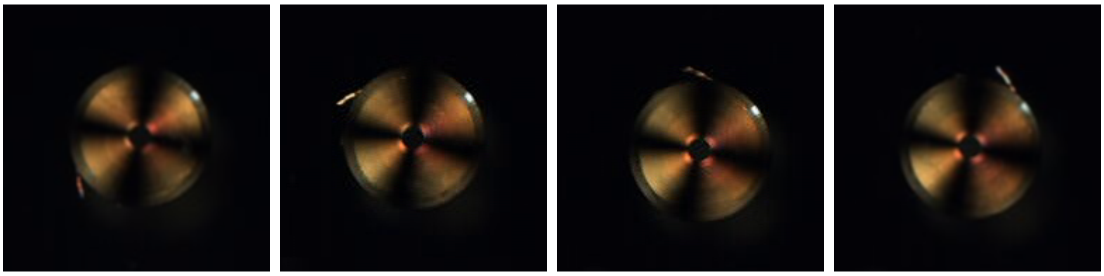

(b) *c*-axis oriented

Figure 2.11: Crossed polarisers technique applied to sapphire anvils that had (a) a random orientation of the cut and (b) with its axis aligned with the optical *c*-axis. From left to right the anvil is rotated for a total rotation of 90°. We can note that when looking through (b) we see the light cross signature of conoscopic interference patterns which remains unchanged when rotating the anvil.

axis we see a clear transition between the light passing through the crystal (case 3) and the extinction (case 2) which occurs every 90° (Figure 2.11a). The case in which the anvil axis was parallel to the *c*-axis (case 1) showed total extinction in correspondence of the culet. On the anvil sides a phenomenon known as conoscopic interference pattern lights up the sides in a cross shape ulteriorly confirming the *c*-axis orientation of the anvil[146].

Out of the four sapphire anvils we had in our laboratory only two showed good alignment between the anvil axis and the optical axis. They have thus been selected to be used in our experiments.

2.3.3 Choosing the right gasket

The other improvement in the methodology for reaching higher pressure using the SAC concerned trying to reduce anvil stresses. The first step was to choose the most suitable gasket material. A hard gasket provide for the necessary support to avoid extrusion of the hole and thus allows to reach high pressure[140]. On the other hand being less compressible they need higher forces to reach the desired pressure and thus higher stresses are applied on the anvil. A compromise in the hardness is thus necessary.

Initial attempts to use copper gaskets only allowed to reach 1.1 GPa before the gasket hole opened up above safe extrusion levels. Moreover, the pre-run phase of preparation of copper gaskets is tedious and time consuming. The technique used for gasket piercing, based on electrical discharge (Betsa MH20M), seems to not be adapted to copper as the process is very long and the electrode is eroded very rapidly.

We decided to move back to steel, the most commonly used material for the fabrication of gaskets, but choosing steel T304 which is a softer grade than the commonly used T301. Furthermore, in order to ulteriorly limit indentation's risk of failure we reduced the level of indentation to few tenth of micron compared to optimal 140-160 which would be recommended for our sapphire culet size (the initial gasket thickness is 200 µm).

Following this procedure for the gasket preparation with the choice of sapphires selected using the procedure described in the previous section, we performed five indentations and the two experiments in Chapter 3 topping 4.22 GPa (37 bar membrane pressure) without anvil failure. More statistics would be necessary to obtain a direct correlation of our experimental procedure and the anvil limitations but no anvils have been broken since.

2.4 Developments for the preparation and characterization of low-dimensional systems

In the first part of this chapter we focused on the description of the high pressure technologies used in our experiments, the challenges that they introduce and how to solve them. Those aspects were seen from a general point of view without particularly focussing on low-dimensional systems which are the essence of this work. In this section we will then focus on sample preparations, characterization and how to make compatible the challenges introduced by the manipulation of low-dimensional systems with the limitations of high pressure experiments.

2.4.1 Transfer systems for 2D materials

Handling low-dimensional materials can be highly challenging. For what concerns nanotubes, the problem is simplified when studying CNTs bundles as they are issued from production in a powder form which is easy to handle as its grains can range from micrometer to millimetre in size. Things complicate when we want to study the properties of individual nanotubes. In this case several methods are used as nano-manipulation[147], direct growth on substrates[148] and dispersion in liquid solution[149]. The latter will be used for the preparation of dispersed nanotubes used in Section 3.4 where we will describe it in details.

In this section we will focus instead on the handling of 2D materials which require dedicated development in order to make them compatible with high pressure experiments. We will refer to the case of graphene but the same procedure applies to other 2D systems.

Transfer techniques

The most commonly used technique for *moving* 2D materials to different substrates is to use temporary sacrificial polymers which allow to transfer the sample from its production site to the desired substrate. The standard procedure to prepare high quality graphene samples is to cleave bulk graphite through the mechanical exfoliation method. This simple technique consists in stripping graphite layers into thin flakes using an adhesive tape[1]. The procedure is repeated obtaining a random uniform distribution of number of layers on the tape. A final exfoliation step is done on a substrate suitable for seeking and finding interesting flakes. An optical scan of the substrate allows to estimate the thickness of the samples that can be then precisely determined by Raman spectroscopy (see Section 1.4.2).

The reduced dimensions of the sample area given by the gasket hole is not compatible with the use of those substrates directly in the DAC. The maximum allowed dimension of a sample in the DAC are of the order of 100 µm while the exfoliation substrates are several millimetres in size. Therefore, the development of a reliable and accurate technique is needed to transfer the samples from the production substrate into the DAC.

The simplest way to achieve deterministic and controlled transfer of a sample into the DAC is to use a viscoelastic polymer substrate for the final exfoliation step and use it as a stamp[150]. PDMS is commonly used as a substrate material for this purpose. Figure 2.12a show the schematics of this procedure: (i) after the final exfoliation on PDMS (ii) the stamp is turned upside down; (iii) it is then aligned with the target and (iv) contact is made with the receiving substrate. (v) The stamp is then slowly peeled off with (vi) the sample remaining on the target substrate. This simple procedure has a high success rate for transferring samples traditionally on Si/SiO_2. In high pressure experiments it is also common

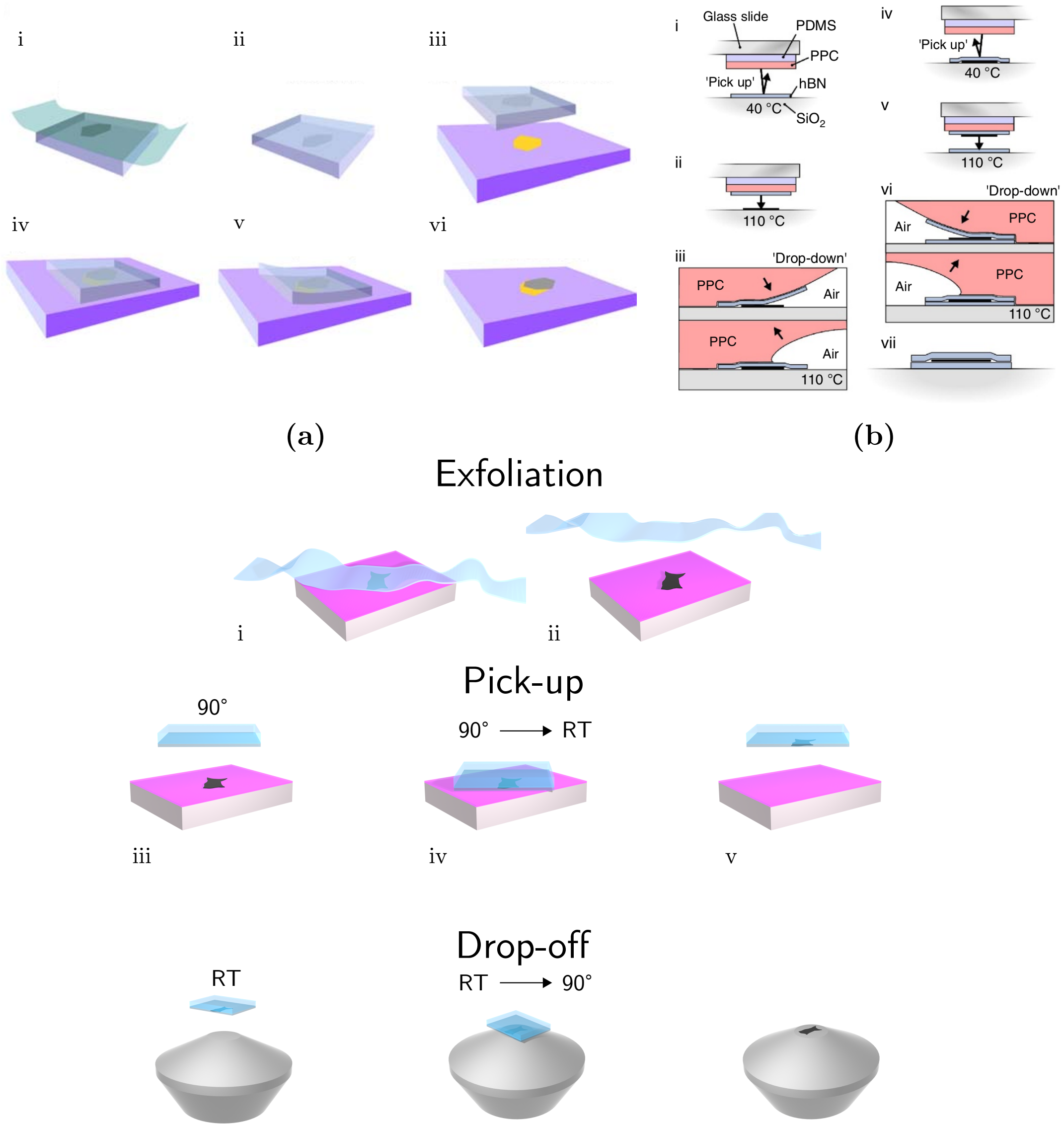

(a) **(b)**

(c)

Figure 2.12: Schematic representation of the viscoelastic polymer assisted transfer technique developed by Castellanos-Gomez et al.[150] for transferring 2D materials. Here a transfer of few layer graphene on hBN is shown (a). Improved technique for controlled pick-up and drop-off of 2D materials designed by Pizzocchero et al.[151] using PPC/PDMS stamps (b). Our adaptation of the Pizzochero PPC/PDMS technique compatible with transfer in the DAC featuring heating of the stamp. Figure (a) is adapted from [150] and Figure (b) is taken from [151].

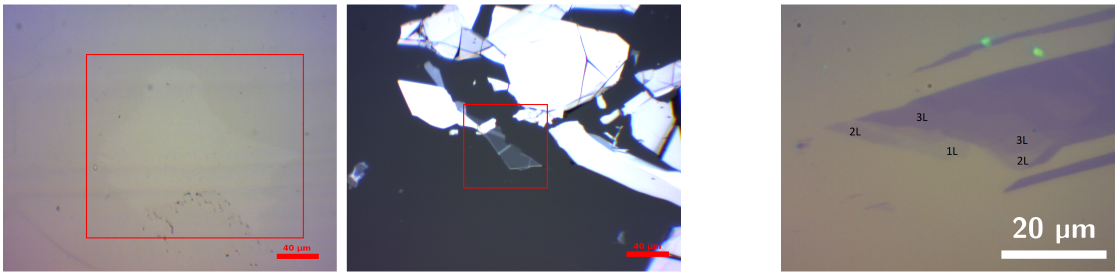

(a) **(b)** **(c)**

Figure 2.13: Optical images of (a) CVD grown monolayer graphene on PDMS, (b) exfoliated few-layer graphene on PDMS and (c) monolayer graphene (1L), bilayer (2L) and trilayer (3L) on Si/SiO$_2$. Red rectangles help visualizing the flakes. The monolayer graphene on PDMS is barely visible compared to when it is supported on Si/SiO$_2$. The FLG counting between 10 to 20 layers is clear also on PDMS.

to transfer the sample directly on the anvil. The downside of this technique is that monolayer graphene is hardly visible when on the PDMS due to its very low optical absorption or reflection (around 3% of incoming light). We can see in Figure 2.13a how a monolayer graphene is barely perceivable when it is on PDMS. Finding thin samples after exfoliation is thus extremely time consuming and sometimes not even possible. For this reason this technique has been used in our studies mainly for few-layer graphene where the contrast is sufficient for locating samples as we can see in Figure 2.13b for a sample counting between 10 and 20 layers of graphene.

In order to find thin graphene samples it is necessary to exfoliate graphite on Si/SiO$_2$. We have seen in Section 1.5.1 that a strong optical contrast enhancement occurs when graphene is supported on Si/SiO$_2$. We can see in Figure 2.13c how one, two and three layers samples are easily detectable on this substrate. It is however not possible to follow the previous procedure to transfer the sample in the DAC due to the rigidity and opacity of this substrate. An intermediate step is needed to strip out the sample from the Si/SiO$_2$ substrate and transfer it to the desired substrate. Pizzocchero et al. developed a procedure (Figure 2.12b) which involves the use of an intermediate PPC (polypropylene carbonate) coated PDMS block to pick-up and drop-off the flake[151]. PPC adhesivity can be controlled using temperature allowing for its use both in the pick-up and drop-off phases. The standard method is however not compatible with the DAC as it would require heating the cell which may cause misalignment of the diamonds. For this reason we developed a new procedure where only the PDMS/PPC block needs to be heated. The procedure is schematized in Figure 2.12c. The sample is exfoliated on a Si/SiO$_2$ substrate in order to easily find thin samples (i) and (ii). The pick-up phase follows a similar procedure to that of Pizzochero et al.. The stamp PDMS/PPC is heated to 90°C (iii), put in contact with the sample and substrate and let cool down to room temperature (iv). The stamp is slowly retracted allowing for picking-up the sample (v). The drop-off procedure starts at room temperature to avoid expansion of the stamp during heating risking to stretch and brake the sample (vi). When in contact the stamp is heated to 90°C (vii) and slowly retracted to leave the

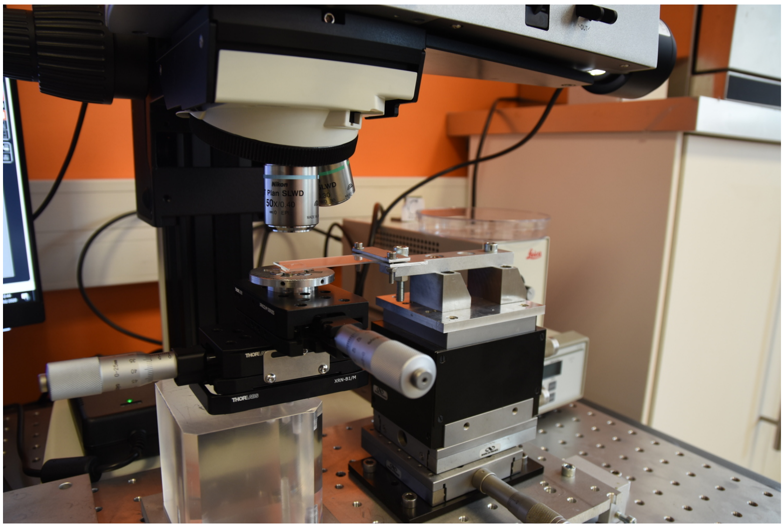

Figure 2.14: Transfer system developed by Forestier et al. for room temperature transfer of 2D systems. Figure taken from [152].

sample on the target substrate. The described procedure can be used to transfer sample directly on the anvil or Si/SiO_2 substrates placed on the anvil. So far it has proved to be be successful for transferring exfoliated bilayers on Si/SiO_2 but the application on monolayers would be straightforward.

Transfer system

The transfer techniques we just described can provide reliable and controlled transfer of 2D materials. However, in order to achieve deterministic spatially resolved transfers we need a translation system that allows for micrometer control of the sample and substrate positions. Forestier et al. developed the transfer system shown in Figure 2.14[152]. It allowed for stamp and target control on the x and y directions, and the stamp approach and retract in the z direction. Optical sample monitoring was possible during the whole transfer procedure thanks to a Laika microscope featuring x10, x20 and x50 magnification objectives with long working distance.

This transfer system was however designed for the PDMS assisted room temperature dry-transfers but it did not integrate a heating system for heat-assisted techniques. Moreover, very little control was allowed on the target positioning resulting in long and tedious preparation before the transfer as well as reduced likelihood of transfer. I performed several device improvements to the system in order to integrate the missing features. Figure 2.15 shows the improved version of the transfer system I developed. Major ameliorations concern the target positioning control (Figure 2.15a). Beside the control of the x (i) and y (ii) target position, I integrated a z-axis micromanipulator for coarse target-stamp approach (iii). A control of the tilt angle was also included (iv). The latter allowed to control the contact and peel off angle between the stamp and the target. A large improvement on the success rate of transfers was achieved after its introduction especially when transferring suspended samples. Finally the control of the rotation around the

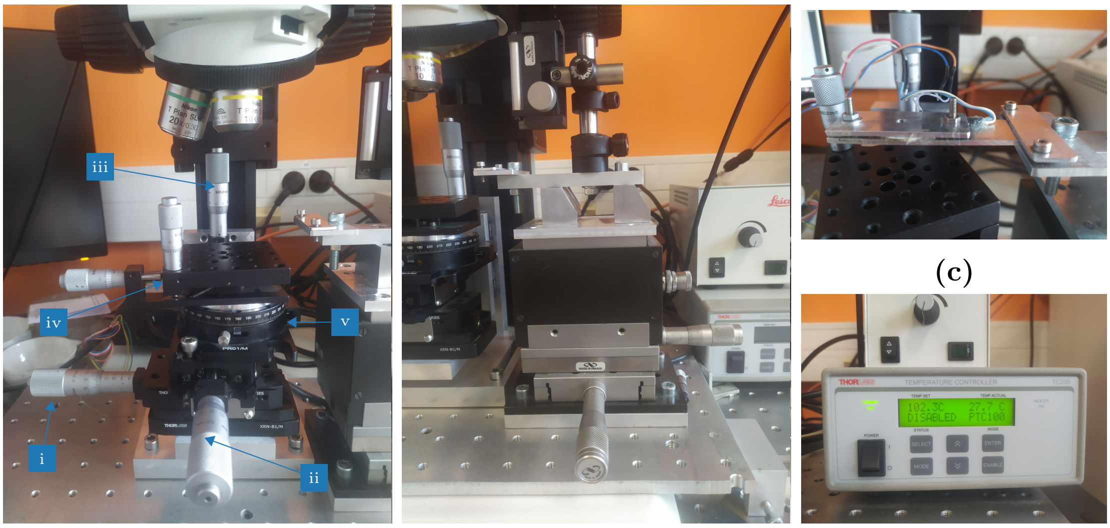

(a) (b) (c) (d)

Figure 2.15: Upgraded version of the transfer system for 2D materials. Major improvements concern the control of the target positioning (a) in the x (i), y (ii) and z (iii) directions, the tilt angle (iv), and rotation around the z-axis (v). The control of the stamp position (b) remained unchanged in relation to the previous set-up shown in Figure 2.14. The stamp heater for temperature assisted transfers is shown in working configuration (c) and the temperature is set by a ThorLabs TC200 heating controller (d).

z-axis (v) allowed for better target alignment as well as to extend the tilt angle (iv) in all the directions. The second major improvement concerns the integration of a heating system for heat-mediated transfers. It consisted of a disc shaped ceramic heater sandwiched between two aluminium plates (Figure 2.15c). A central traversing hole allowed for visualization of the sample through the PPC/PDMS block that is placed on the bottom aluminium plate. A platinum resistive temperature detector was also clamped between the plates for temperature measurement. A Thorlabs TC200 heating controller was used for temperature control and measurement.

With the upgraded transfer system we could prepare the 2D structures studied in Chapter 4. The most complex structures that we fabricated include the suspended few-layer graphene studied in Section 4.4.3 as well as the graphene/hBN heterostructures of Section 4.5.

2.4.2 2D cartography integrated Raman spectrometer

The nature of low-dimensional systems make them being extremely sensitive to local variation of the environment, external field and sample morphology. The possibility of probing their local properties is thus essential for a thorough understanding of the physical phenomena that they are involved with. The local character of Raman spectroscopy makes it a perfectly suitable technique to fulfil this task and it full potential can be attained when it is combined with an automated 2D

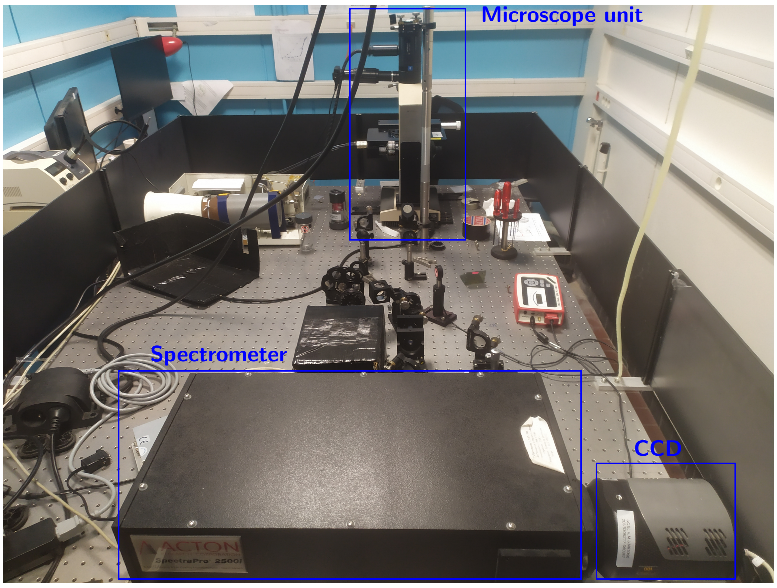

Figure 2.16: Picture of the custom made Raman set-up used during the experiments.

scanning system. We will thus describe in the following the custom-made Raman spectrometer used for the majority of our experiments followed by the developed adaptation for realizing 2D spectral cartographies of low-dimensional materials.

Custom-made Raman spectrometer

Figure 2.16 shows a photo of the Raman spectroscopy set-up. It is a custom-made spectrometer developed in the laboratory and adapted for high-pressure experiments of low-dimensional systems. It is based on a Princeton Instruments Acton SP-2500i spectrometer mounted with a 1800 $\mathrm{gr\,mm^{-1}}$ grove density grating with blaze wavelength of 500 nm. Before entering the spectrometer the excitation laser beam crosses several optics shown schematically in Figure 2.17. The excitation source is a 532 nm diode pumped solid state laser for which the output power is controlled using a gradient filter. After expansion the beam is sent to a Volume Bragg Grating (VBG). This optical mirror is designed to reflects light only when the Bragg condition is respected, reflecting the beam towards the microscope. The latter consisted of an imaging system coupled to a light source in reflection geometry and a transmission light source. Mitutoyo x20, x50 and x100 objectives were used for focusing the excitation beam on the sample which lays on a motorized x-y stage. Raman signal is then collected in backscattering geometry following the incoming path back to the VBG. This component allowed for rejection of the Rayleigh elastic scattering through reflection with a bandwidth of less than 20 $\mathrm{cm^{-1}}$ transmitting the sample's Raman signal. The efficiency of the VBG is around 90% both in transmission and rejection. Two ultra-narrow notch filters followed, ulteriorly decreasing the Rayleigh signal allowing to measure as low as 40 $\mathrm{cm^{-1}}$. Two coupled mirrors were used to direct and focus the filtered signal into the spectrometer slit. Finally, the Acton SP-2500i spectrometer focus the

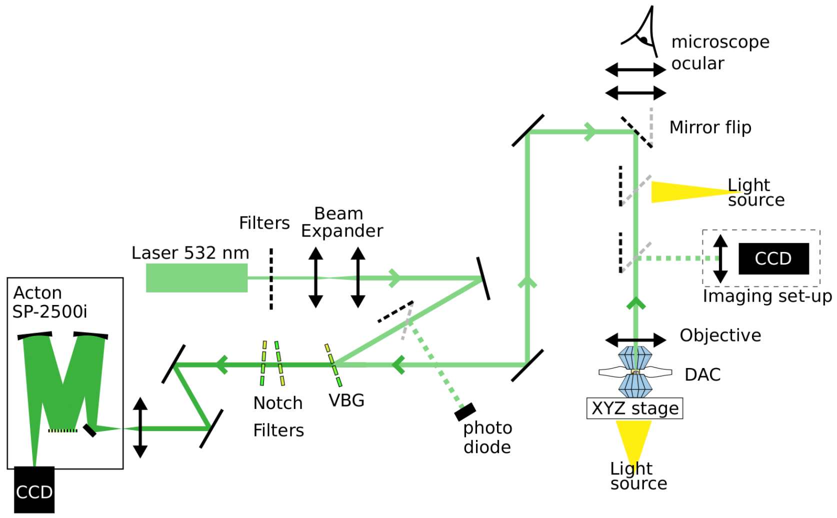

Figure 2.17: Schematic representation of the custom made Raman spectrometer. The green line shows the optical path followed by the 532 nm laser. Light green arrows show the excitation light direction on the path while the dark green ones the back scattered Raman signal. Black and grey dashed lines show turnable mirrors for sample observation and power measurement.

diffracted light onto a 1340x100 pixels Princeton Instrument Pixies CCD camera cooled at -75°C. The resolution of the spectrometer was estimated to 1 cm at the centre of the spectral window with an accuracy of ~ 2 cm^{-1} across the whole window.

To keep the spectrometer at its maximum efficiency I performed regular alignments of the optical components and calibration of the spectrometer. The quality of the alignment was verified by measuring the TO mode of a reference silicon crystal. The spectrometer was considered aligned if a minimum of 200 counts/s was obtained for a laser power of 0.7 mW using a x50 long working distance objective. For graphite sample we obtain typically 20 counts/s in the same experimental conditions.

Ramander: 2D Raman cartography software

In order to perform automated Raman acquisitions with this set-up it was necessary to develop a software interface that would allow for communication between the spectrometer and the x-y movement unit. The microscope's sample stage is equipped with two coupled motorized slides with submicron precision covering the planar translations. A Märzhäuser Tango Desktop controller allows to shift the stage via a joystick or an external computer. The Acton SP-2500i spectrometer and the Princeton Instrument Pixies CCD camera are commanded by Princeton Instrument's Lightfield software. In order to establish communication between the independent parts I developed with the help of PhD student Max Gerin an interface written in National Instruments LabView that I named Ramander. Figure 2.18a shows the main screen of the application with red rectangles highlighting the main features:

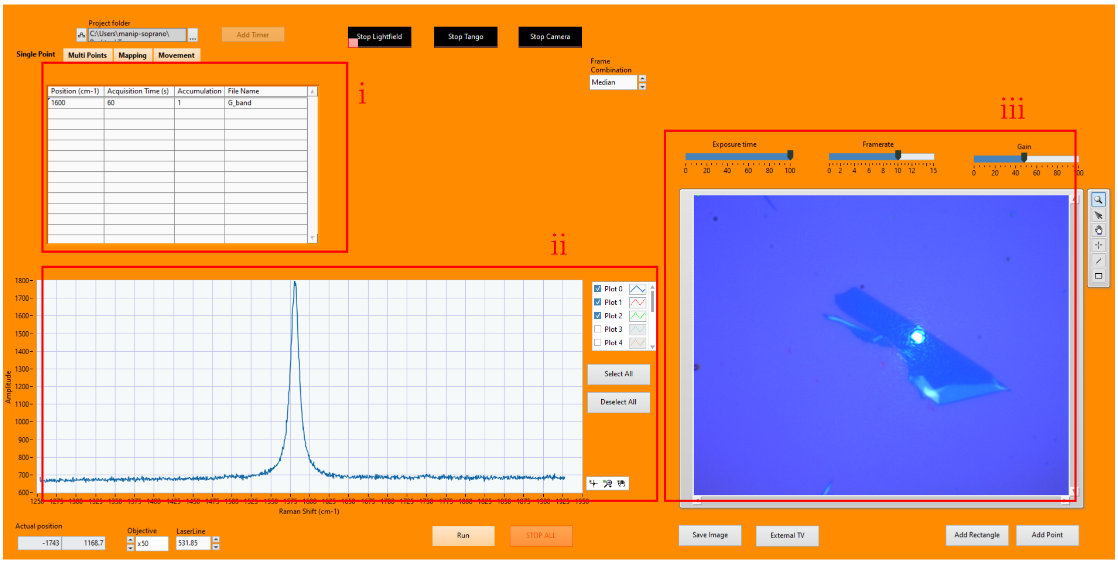

Project folder: C:\Users\manip-soprano\

Position (cm-1)	Acquisition Time (s)	Accumulation	File Name
1600	60	1	G_band

Frame Combination: Median

Actual position: -1743 1168.7

Objective: x50

LaserLine: 531.85

(a) Main interface

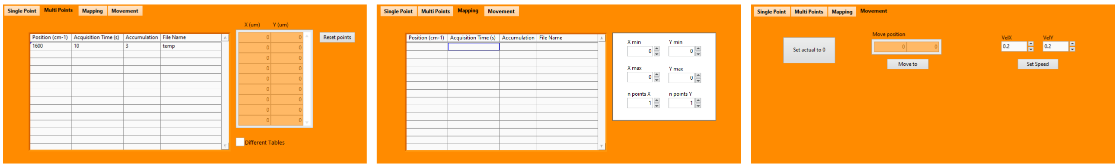

Position (cm-1)	Acquisition Time (s)	Accumulation	File Name
1600	10	3	temp

X min 0, Y min 0, X max 0, Y max 0, n points X 1, n points Y 1

Move position 0 0; VelX 0.2; VelY 0.2

(b) Multi points tab **(c)** Mapping tab **(d)** Movement tab

Figure 2.18: Ramander software main interface (a). The red rectangles highlight the main parts: (i) the control tabs, (ii) the spectrum plotter and (iii) the optical visualization output. Beside the Single Point tab selected in the main interface, the three other tabs are shown in (b), (c) and (d)

(i) On the top left, the main control panel features a tab interface where it is possible to select different actions to command the spectrometer and the motorized stage. The *Single Point* tab allows to create a queue of commands to perform procedural acquisitions without interaction with the motorized stage. Commands are given in the shown *command table*, with each line being a spectral acquisition, specifying the grating centre (Position (cm^{-1})), the Acquisition Time, the number of Acquisitions and the output File Name. Those tasks are sequentially sent to Lightfield and processed in order. The next tab, *Multi Points*, shown in Figure 2.18b, allows to perform single point acquisitions on a list of x-y pairs of coordinates. For each position it is possible to either assign the same command table to each point or perform different tasks for each position by enabling the *Different Tables* tick box. Finally, the *Mapping* tab (Figure 2.18c) allows for scanning a rectangular region for which the top-right and bottom-left corners' coordinates and the number of points in each direction have to be inserted by the user. A common command table is executed at each point. An additional *Movement* tab is added for simple computer assisted motor movements (Figure 2.18d).

(ii) Below, an amplitude vs Raman shift plot allows to show the spectra obtained during the execution of the commands given in the *Multi Points* and *Mapping* tabs. A list of entries on the top right side of the plot allows to select which plot to visualize and hide.

(iii) On the right, integrated optical imaging can also be enabled in order to visualize the sample morphology as well as record points of interest. The main camera setting are easily accessible for efficient image adjustments.

The type of file obtained after the acquisition depends on the type of task performed. For *Single Point*, acquisitions are entirely performed by Lightfield so the file obtained was in the Princeton Instruments native format *.spe*. For *Multi Point* and *Mapping* the data was output in *.txt* format. Table 2.1 shows a typical snippet of the data obtained after a mapping scan. The first column contains the Raman shift in cm^{-1} related to each pixel of the detector. Each other column contains the corresponding number of counts measured at a given spatial position which was set as a header to the column in the format *x,y* in micron. Metadata is included as header to the file and featured the time at which the acquisition finished, the exposure time, the number of exposures, the grating central wavelength and the laser wavelength.

2.5 Summary

In the present chapter we presented the major experimental instrumentation employed during this work. In Section 2.3, we concentrated on the characterization and upgrades I performed on sapphire anvils cells. We found, by interposing sapphire anvils between crossed polarisers and observing them by optical microscopy, that in only a part of the sapphires we stored the anvil axis was aligned with the optical axis of the crystal. We thus selected those anvils for our experiments.

Table 2.1: Snippet of the data table in output of a *Multi Point* and *Mapping* using the Ramander program.

Shift	0.00,0.00	1.82,0.00	3.64,0.00	5.45,0.00	7.27,0.00	
1254.1	634	631	629	632	631	...
1254.6	621	620	621	623	625	...
1255.2	621	618	618	618	622	...
1255.7	620	621	616	615	620	...
1256.2	615	619	618	622	618	...
...	...	...	...	...	...	...

Moreover, we improved our indentation procedure by using soft grade steel gaskets and reducing the indentation depth. With those two improvements we could attain a maximum *in-situ* pressure of 4.2 GPa without the anvil failure, 1.2 GPa higher than our previously highest recorded value in an experiment that led to the anvil breakage. Those anvils were extensively used throughout the experiments in Chapter 3. Their use can, however, be extended to other systems and numerous other studies. Our particular interest will be to include the characterization of the formation of defects in high pressure experiments on pristine and already defected graphene samples thorough the study of the D-band at high pressure. In addition to that, on the same systems, they could be employed for the identification of the formation of sp^3 sites by monitoring diamond-like features.

In Section 2.4.1 we discussed about the transfer techniques and devices for the preparation of 2D materials for high pressure. We described several polymer assisted transferring techniques which we employed for the experiments in Chapter 4. One of the techniques was developed by me for the pick-up of samples exfoliated on Si/SiO_2 and dropped-off on the high pressure anvil or on a substrate glued on it. The samples prepared with this technique were not included in this work but I successfully picked-up and transferred bilayer samples from and to Si/SiO_2 substrates as well as several few-layer graphene samples. The main goal of this development is to successfully prepare suspended mechanically exfoliated monolayer and bilayer samples on Si/SiO_2 for high pressure experiments (see Section 4.2 for more details). In the same section, we described the upgrade I performed to the transfer system we used to finely manipulate the samples for those preparations. Major improvements included the introduction of a heating system for PDMS/PPC stamps, and the addition of the control of a coarse z-axis translation, and in-plan and out-of-plane rotation of the target. Those improvements allowed to increase our success rate for transferring few-layer graphene of more than 10 layers from PDMS to Si/SiO_2 to almost 100%. The overall transfer success rate was improved for all the samples.

In the last section of the chapter we described our custom Raman spectrometer which was used for the experiments in Chapter 3 and most of the works in Chapter 4. We also illustrated the Ramander Raman mapping software we developed for which I was the major contributing developer. The software allowed to find the individualized nanotubes of Chapter 3, to perform the mapping of suspended and supported bilayer graphene of Section 4.3 as well as perform several other characterization not included in this work.

This chapter concludes the first part of the manuscript focused on establishing the theoretical foundation and experimental methodology required for the upcoming chapters. We will proceed now to the following chapters where we will thoroughly detail the main experimental results of my work.

Chapter 3

High pressure induced geometrical transitions in single walled carbon nanotubes.

The characterization of the response of carbon nanotubes to high pressure drew a lot of attention in the low-dimensional systems community due to extremely rich diversity of phenomena occurring at relatively low pressure. Major interest was given to the geometrical transition of CNT from their tube-like shape towards a flatten (collapsed) shape which drastically modify their electo-optical properties. Pressure sensors and switches promptly come to mind as possible applications but fast, reliable and accurate characterization methods are necessary for improving their efficiency. In Section 3.1.1 we will describe the experimental techniques used so far for the characterization of this phase transition at high pressure which used the disappearance of the tube's RBM as an indicator of the collapse of the CNTs[35, 43]. A turning point that allowed for stepping forward in the characterization was introduced by a recent study of Picheau et al. who measured a direct Raman signature of the collapse, given by the appearance of a defect-free D-band associated with the geometrical transition[88]. In Section 3.1.2 we will briefly introduce the main results of this study describing the mechanism that triggers the appearance of the D-band.

Backed up by those insights on the characterization of the nanotubes collapse our work aimed to get a further comprehension of the mechanisms governing the pressure response of carbon nanotubes to high pressure. In particular the use of the D-band signal has been very rarely exploited in high pressure experiments. This is due to the pollution of the spectrum by the diamond anvil's first order Raman feature which can be avoided by the use of sapphire anvils (see Section 2.3). Experimental challenges were introduced also by the choice of the most suitable PTM for each experiment. A series of high pressure runs featuring carefully selected PTM allowed to obtain a complete description of the nanotubes collapse. In Section 3.2 we will describe the PTMs used in our experiments highlighting the pros and cons of each.

I personally performed the totality of the experiments included in this chapter. One part of the study was conducted using bundles SWCNT samples, where we showed how the D-band of CNTs can be used to detect the tube's collapse at high pressure. Moreover, we could follow the reversibility of the transition in the decompression cycle where the sample's initial conditions are recovered after the complete pressure release. This work will make object of Section 3.3. The study was further extended by reducing the number of tubes in the bundle until following the evolution of the collapse of an individualized (16,8) tube with pressure (Section 3.4).

3.1 Raman signatures of collapsed carbon nanotubes

The nanotubes radial collapse induce drastic modification of the nanotube's physical properties largely affecting their electronic structure[153]. Conducting-insulator and insulator-conductive transitions have been observed[25] which have direct impact on the nanotubes optical properties. As well as the electronic structure, the phonon modes are majorly impacted experiencing a drop in the G-band frequency at the transition[35]. Moreover, carbon nanotubes feature a unique Raman signature given by the RBMs. Being associated to the vibrational modes in the radial direction they are highly sensitive to the tubes geometrical changes. We will present now the results in the literature which used this signature for the detection of the tubes geometrical transitions with pressure.

3.1.1 RBM quenching

Thorough analysis of the RBMs evolution with pressure have been performed in the literature[35, 43]. In particular their intensity I_{RBM} (peak area) was used to describe the various phases of the tube transition. Torres-Dias et al. showed that the RBMs experience a drop of intensity until complete disappearance when compressed[43]. The collapse pressure is found to be inversely proportional to the tube diameter. Figure 3.1a shows some of the spectra obtained at different pressure. The spectra were fitted imposing physical constrains allowing to extract each RBM's intensity. The intensity evolution with pressure is shown in Figure 3.1b. An initial drop at low pressure is experienced for all the diameters followed by a plateau. After this constant regime a second smooth decrease reduces the RBM intensity until complete quenching passing through a transient phase where intermediate values of I_{RBM} are measured. The intensity was fitted by the function:

$$I_{RBM}(P) = \frac{1}{2}\left(I_0 e^{-bP} + a\right) \operatorname{erf}\left(\frac{w}{P_0}\left(P - P_0\right)\right) \tag{3.1}$$

with I_0 the RBM's intensity at ambient pressure, erf is the Gauss error function and a, b and w phenomenological parameters. The authors assigned the decrease of intensity with the nanotube's collapse. Backed up by computational simulations those results allowed to obtain the general behaviour described in Section 1.6.3 by Equation 1.20.

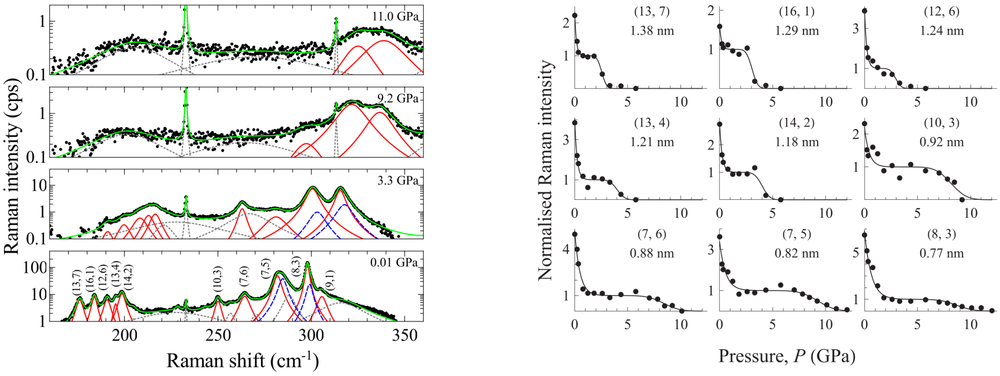

(a) **(b)**

Figure 3.1: Pressure evolution of the RBMs spectrum of SWCNTs compressed in water PTM measured by Torres-Dias et al. (a). The spectra are taken using 647.1 nm excitation wavelength. Each red solid line represents a Lorentzian peak fitting the RBMs, blue lines fit the RBMs of water filled tubes and grey dashed lines other background peaks. The total sum of the functions is shown by the green solid line fitting the data (black dots). (b) shows the area of those RBMs (black dots) fitted by Equation 3.1 (black solid line) and normalized imposing the plateau being equal to 1. Figures taken from [43].

3.1.2 Defect-free D-band

Alternatively to the RBMs, another Raman signature of CNTs is highly sensitive to the tube's geometrical changes which is the D-band. We mentioned in Section 1.4.3 that this band is traditionally used as an indicator of the amount and type of defects in carbon nanotubes. However, beside what is commonly identified as structural disorder, such as atomic vacancies, line or plane defects, we can extend the definition to a more general one. In our case the D-band is activated by inhomogeneities of the electron potential introduced by symmetry breaking of the electron potential at the folded edges of the flatten CNTs. Gupta et al. already proposed that a defect free D-band could be originated by graphene folds [154]. They measured a folded monolayer graphene, shown in Figure 3.2a, and they found that at the fold edge the D-band signal was present and was otherwise absent in the pristine region of the sample. Following the same line of thoughts Picheau et al. conducted similar experiments on flattened CNTs assimilating the edge of a flattened CNT to a folded graphene or few layer graphene[88]. They produced the samples by extracting the first few outer layers of multi-walled CNTs. This process resulted in large diameter single- and few-walled nanotubes that were unstable at ambient pressure thus collapsing spontaneously into flattened CNTs. Figure 3.2c shows the TEM imaging of some samples produced using this method where the flattened tubes are clearly distinguishable from the originating multi-walled. The samples were compared using Raman spectroscopy which showed that flattened samples indeed featured an intense and narrow D-band which was absent in cylindrical samples. Moreover, polarisation dependent Raman measurements demonstrated that the D-band was activated by a linear scatterer parallel to the tube's axis in agreement with the hypothesis that the curvature act as a scatterer for the phonons.

The D-band is thus a unique probe of the nanotubes geometrical state. It provides a direct proof of the collapse identified by the appearance of a new signature thus avoiding eventual problems connected to loss in signal, resonance or parasite background that might affect the RBMs analysis. However, in Section 2.3 we described the issues linked with measuring the D-band signal in the traditionally used high-pressure devices, the diamond anvil cells, and that those issues can be overcame by using sapphire anvils. In the rest of this chapter we will show how the use of those anvils allowed us to exploit the D-band as a novel spectroscopic signature of the nanotubes collapse with pressure.

3.2 Experimental methods

To perform the experiments we equipped a Letoullec anvil cell (see Section 2.2.1) with a couple of Almax-Bohler cut sapphires with 450 µm cullet. The samples used are commercially available single walled carbon nanotubes (SWCNT) provided by Sigma Aldrich (Ref. 755710). They come in small powder grains of bundles produced by catalytic carbon vapour deposition. The distribution of diameters includes relatively large tubes spanning from ~ 1 to ~ 2 nm.

For the experiment's design great importance was given to the choice of the most suitable PTM for those sample. Because of the relatively large diameters of the tubes we studied, the expected collapse pressures are limited to low pressures (below 5 GPa). The PTM's hydrostaticity do not play a central role at those pressures for the most common PTMs described in Section 2.2.3 which retain relatively low levels of non hydrostaticity. On the other hand, the PTMs' spectroscopic signatures importantly affected the signal's background, potentially masking the Raman modes associated with the sample. Due to the need of studying small variations on the sample response to high pressure we choose the PTMs that least compromised the sample signal.

Figure 3.3 shows the main individual contributions of the anvils and PTMs to the Raman background in high pressure experiments. We have already discussed in Section 2.3 about the diamond anvil pollution in the D-band region that can be avoided by using sapphire anvils. Here we will focus instead on the PTMs' contribution. We considered two PTMs for our experiments: 4:1 Methanol:Ethanol and nitrogen. The former is composed by a methyl or ethyl group chained to a hydroxyl group. The main contribution in the Raman spectrum within the CNTs region of interest is given by a wide peak centred around 1450 cm^{-1} identified with the CH$_3$ group bending modes[155]. In Figure 3.3 its spectrum is shown in dark blue where we can see that it partially overlap with the SWCNT modes. This conflict is generally not significant as the nanotubes signal intensity is much more important than the PTM's one. However, when dealing with small samples of few tubes where the signal intensity is reduced, its relative contribution is amplified and it can mask the sample features. It was the case for our studies of individualized CNTs which we will discuss later in this chapter. 4:1 Methanol:Ethanol

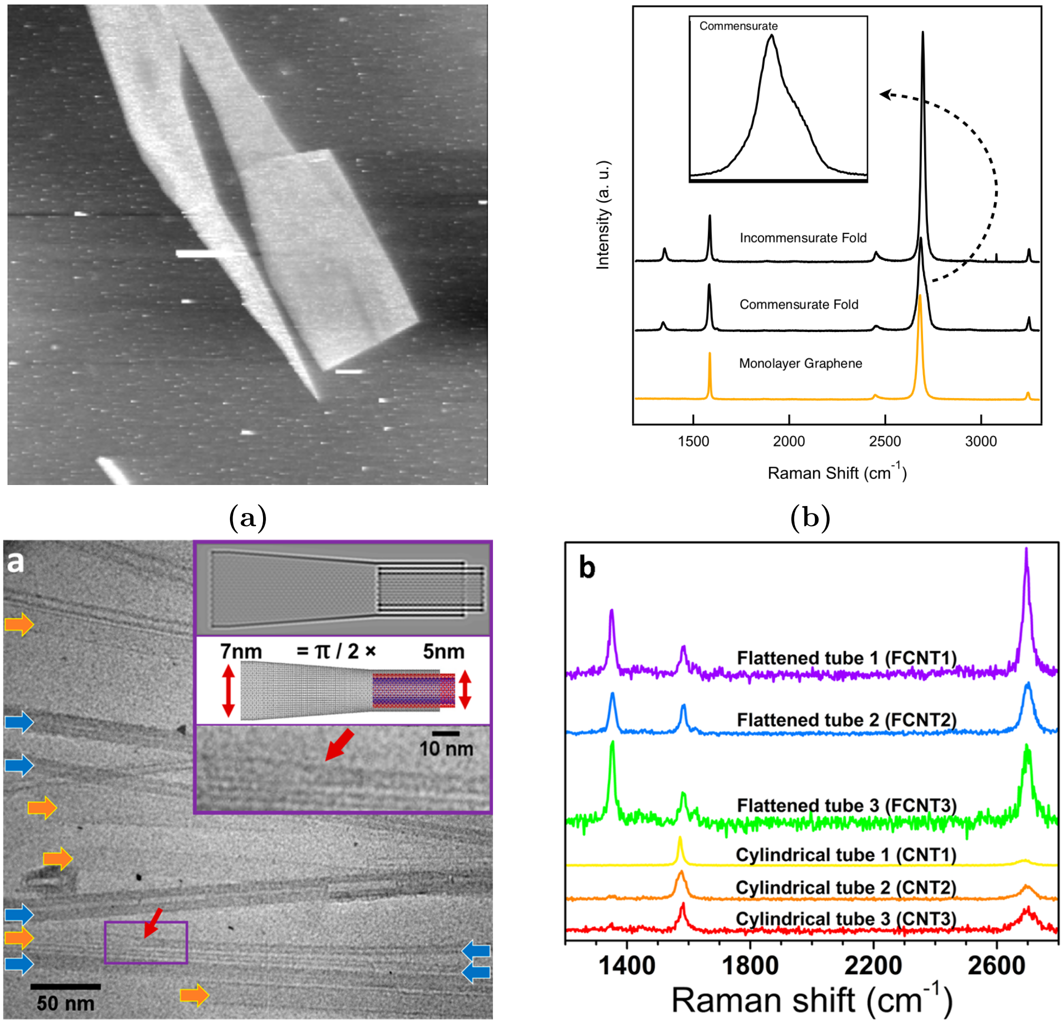

(a) **(b)**

(c) **(d)**

Figure 3.2: (a) AFM imaging of a folded monolayer graphene sample. The comparison of the Raman spectrum of folded and unfolded monolayers is shown in (b). Commensurate folds refer to bilayers with long range ordering. (c) TEM imaging of multi-walled CNTs (blue arrows) and flattened CNTs (orange arrows). A zoom on a tube extracted from the MWCNT is shown in the inset (bottom) paired to a TEM simulation (top) and an AIREBO potential optimized atomic structure (middle). (d) Spectra of cylindrical and flattened tubes showing the appearance of a strong D-band in the collapsed tubes. Top two figures taken from [154] and bottom two from [88].

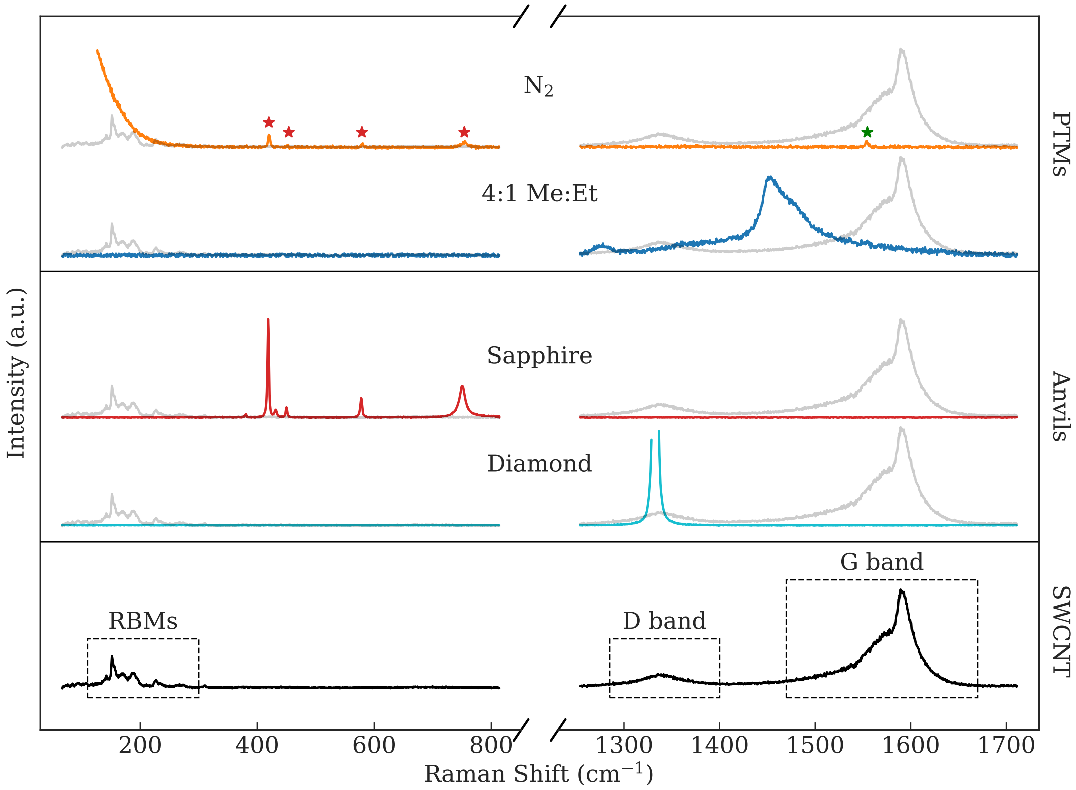

Figure 3.3: The Raman signature of PTMs and anvils compared to the spectrum of the SWCNTs bundles. The spectra are acquired using 532 nm excitation wavelength at room pressure, beside nitrogen which is acquired at 0.4 GPa. Red and green stars in the nitrogen spectrum indicate respectively the peaks of sapphire and oxygen.

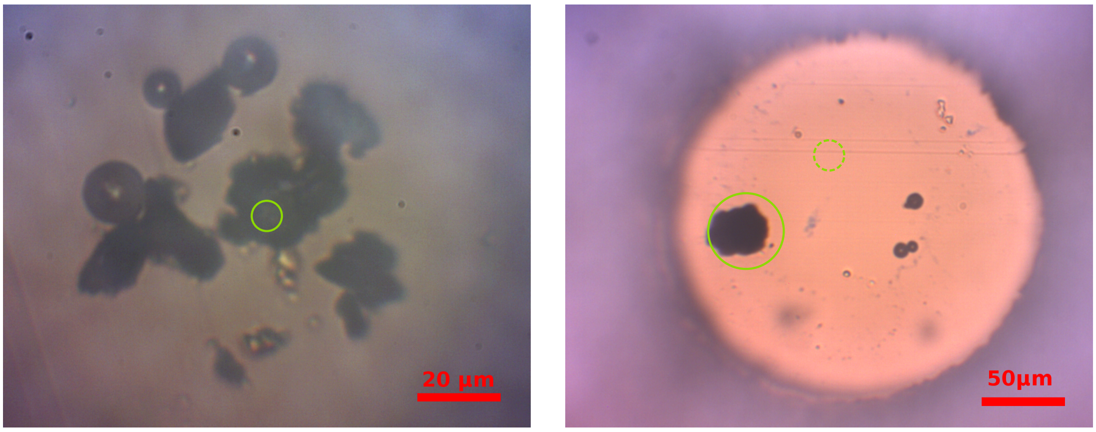

(a) 4:1 Methanol:Ethanol **(b)** Nitrogen

Figure 3.4: Optical images of the samples used in our experiments. The green solid-line circles highlight the part of the sample that have been studied during the experiments on bundle CNTs. The green dashed circle indicates the region where the individualized CNTs have been found.

could not be used in this case. On the other hand, one of the advantages of this PTM is that the low frequency region is clear of peaks thus RBMs can be studied without external signal pollution. Finally, 4:1 Methanol:Ethanol may show a wide fluorescence signal when increasing pressure due to impurities in the mixture. Depending on the run this wide background may appear or not, but in our case it was sufficiently intense to fully mask the tubes signal above 3 GPa, persisting during decompression that could not be followed using this PTM.

The second PTM considered was diatomic nitrogen. Being a much simpler molecule that methanol and ethanol, its Raman vibrational spectrum only shows a thin peak around 2330 cm^{-1} at ambient pressure thus not impacting the CNTs spectrum. However, the cell loading procedure, which consisted in submerging the cell in a bath of liquid nitrogen, retains some oxygen from the air which mixes with nitrogen and remains in the cell. Its Raman signal is thus also present identified by a weak narrow peak around 1550 cm^{-1}. Beside the vibrational modes those diatomic molecules have an important spectral contribution given by the rotational spectrum. At ambient pressure it is characterized by a series of thin sharp peaks at frequencies below 200 cm^{-1}, decreasing in intensity for increasing frequency. When the gasses are pressurized into their liquid phase, the peaks widen up resulting in a large tail that fully masks the RBMs signal. In orange in Figure 3.3 we can see the spectrum of nitrogen at 0.4 GPa where it is shown the evident overlap between the RBMs and its rotational spectrum. Using this PTM it was thus not possible to follow the RBMs evolution with pressure.

3.3 High pressure studies of bundle SWCNTs

The first experiments we conducted were performed on small grains of powder SWCNTs. Those samples are easy to transfer inside the SAC. Simply using a sharp

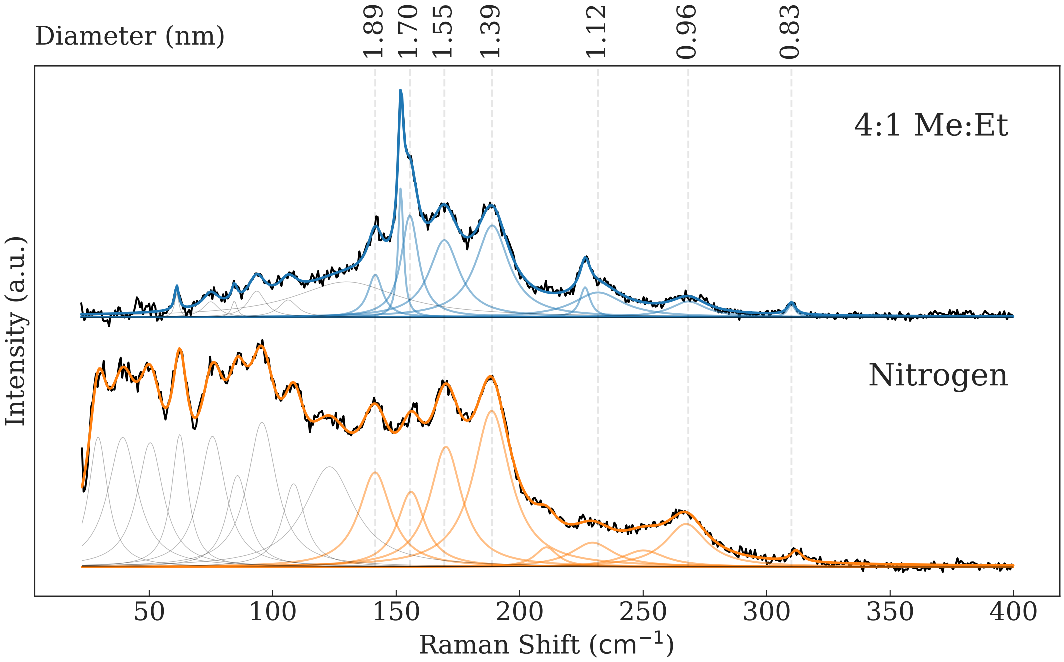

Figure 3.5: RBMs spectra of the bundle samples for the two experiments in alcohol (4:1 Me:Et) and nitrogen. Grey Lorentzian peaks show the background introduced by the air spectrum while coloured ones are the individual RBMs. The thicker coloured line is the sum of all the components fitting the data (in black).

needle it is possible to collect small bundles of SWCNTs of few tenths of micrometer which easily fit the 150-200 µm gasket hole. We performed two experiments using 4:1 Methanol:Ethanol and nitrogen PTMs. The bundle samples measured during the experiments are shown in Figure 3.4. The samples have been characterized at ambient pressure in order to determine the diameters of the tubes resonant with the incoming excitation laser at 532 nm. The RBMs spectra have been used to characterize the samples converting the RBM frequency into the tube's diameter using Equation 1.13. The spectra are displayed in Figure 3.5. We can note how the two samples present a similar diameter distribution with the majority of resonant tubes diameters ranging between 1.39 nm and 1.89 nm.

3.3.1 Evolution of the Raman features with pressure

Figure 3.6 shows the background subtracted G and D-band spectra obtained in the pressure cycles for the two experiments. The advantage of using sapphire instead of diamond as anvil material is readily highlighted by the clearance of the entire spectrum from the eventual anvil background signal. The D-band as well as the G-band could be followed throughout the whole pressure range. As expected, we note a blue shift of both modes which is associated with the hardening of the carbon bonds. The first original result that can be extracted from those spectra is the monotone augmentation of the D-band signal intensity relative to the G-band that is experienced both in the 4:1 Methanol:Ethanol and nitrogen

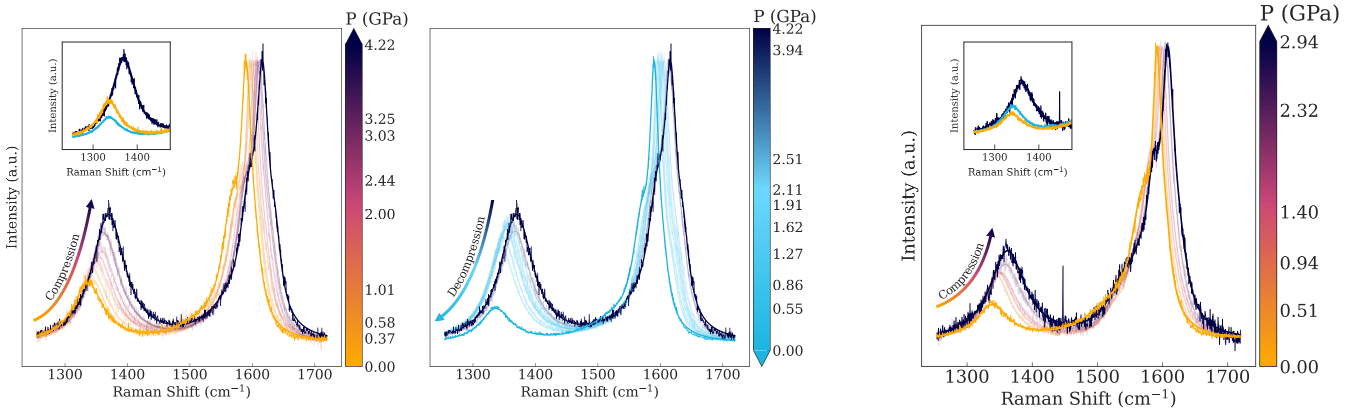

(a) Nitrogen **(b)** 4:1 Methanol:Ethanol

Figure 3.6: Pressure evolution of the G and D-bands for the bundles samples of the two experiments. The nitrogen experiment (a) includes both compression and decompression cycles while only the compression one is shown in the case of 4:1 Methanol:Ethanol (b). A colour gradient is used to indicate the pressure at which the spectra are taken with its values reported on the colour scale bar. The insets show the D-band before (orange) and after (light blue) the experiment and at the maximum pressure value (dark purple). All the spectra are normalized to the G-band maximum value.

experiments. Furthermore, thanks to the possibility of following the decompression cycle in the nitrogen experiment, we can observe that the D-band intensity decreases upon release, reaching a similar value to that of depart when the cell is opened again. The insets in Figure 3.6 show that the spectrum of the sample before cycle is recovered in both experiments, with small variations probably due to sample inhomogeneities. Those results are compatible with our hypothesis of the emergence of a defect-free D-band when submitting the CNTs to compression induced by the CNTs' collapse. Moreover, whilst the reversibility of the process was expected no previous record of the possibility of following its signature during the decompression has been recorded.

3.3.2 Spectra analysis of the carbon nanotubes bundles

In order to complement the qualitative analysis of the spectra we fitted the D and G-bands of the SWCNTs using Lorentzian functions. Figure 3.7 shows the fitted ambient pressure spectra for the two experiments. Dashed lines show the G-band components that we used to fit the experimental data. A good fit of the data was necessary to obtain systematic measurements the G-band peak area. We can see that four peaks were sufficient for the correct representation of the total signal in the nitrogen experiment while an additional one was necessary for the 4:1 Methanol:Ethanol one. The D-band was well fitted by a single Lorentzian component.

With the extracted fit parameters we identified the quantity that better would

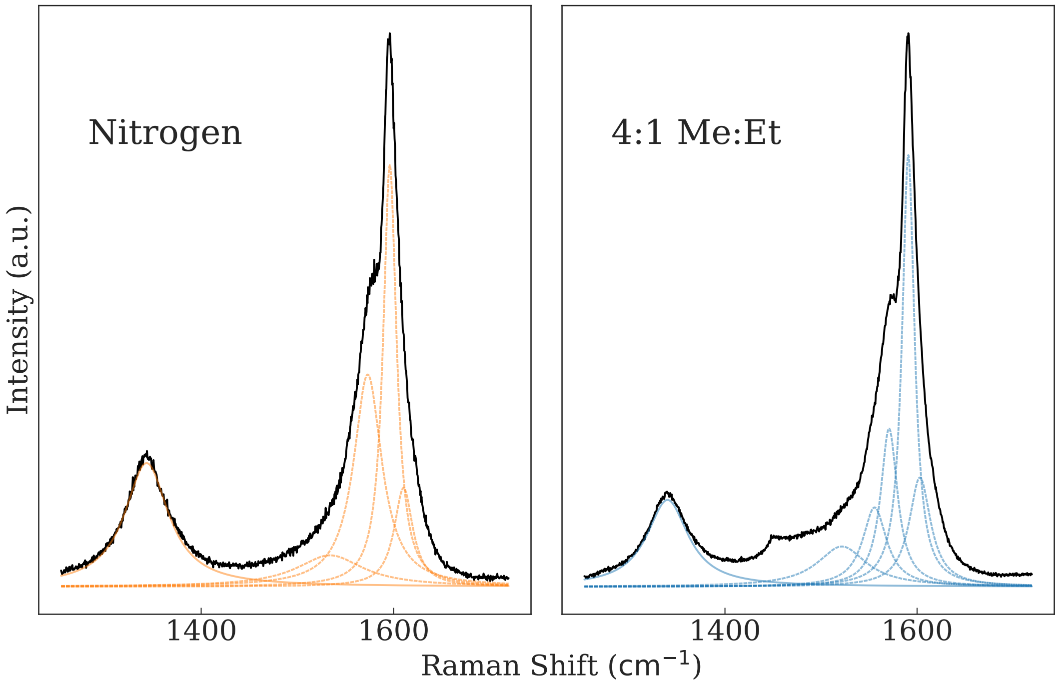

Figure 3.7: Normalized ambient pressure D and G band spectrum of the bundle samples. Dashed lines show the G-band components and the solid coloured line the D-band. The black line shows the experimental data.

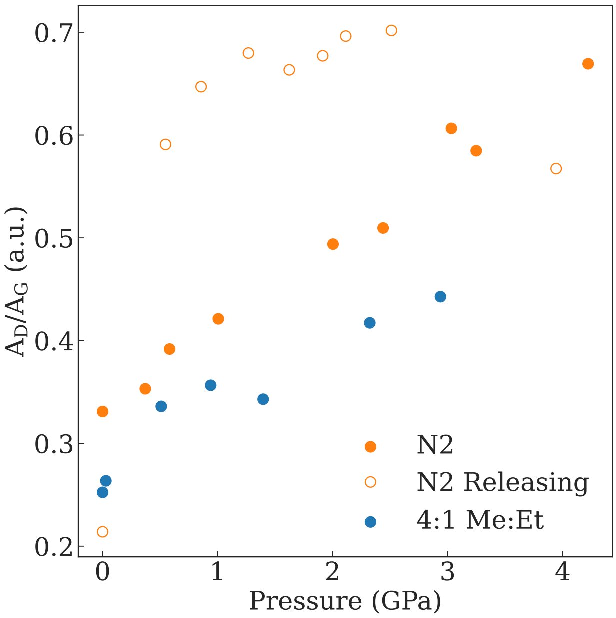

Figure 3.8: Evolution of A_D/A_G with pressure. Filled and empty dots show respectively the compression and decompression cycles.

describe the tube's collapse. We defined A_D/A_G as the ratio of the area of the D-band A_D and the sum of the area of each G-band component A_G. In Figure 3.8 the evolution of A_D/A_G is plotted as a function of pressure. We obtained qualitatively a similar behaviour in the two experiments with an increase of A_D/A_G with pressure of a factor ~ 2 at the highest pressure. A step like discontinuity is present in the two cases between 1.5 and 2 GPa. The pressure release monitored in the nitrogen experiment shows an hysteresis character of A_D/A_G with very moderate decrease until 1.9 GPa suggesting that the tubes face difficulties to inflate back to the cylindrical geometry. A sudden drop in A_D/A_G is experienced upon complete pressure release following the cell opening.

The evolution of the RBMs with pressure has also been studied and can be used to correlate A_D/A_G with the diameter of the tubes. This was possible only in the case of 4:1 Methanol:Ethanol as PTM due to the strong rotational spectrum of nitrogen. The spectra at each pressure point are shown in Figure 3.9a. The general trend shows a decrease in the RBM's intensity with pressure with only the 0.96 nm tube signal still present at the highest point. The peaks have been fitted using Lorentzian functions for which the area normalized to the ambient pressure point is shown in Figure 3.9b. From the plots we can note that the area of the three central diameters 1.39, 1.55 and 1.70 nm experience a drop at 1.4 GPa. The collapse pressure is compatible with the reported one in the literature beside the 1.39 nm tube which was expected to collapse at slightly higher pressure (3.2 GPa). At this pressure A_D/A_G experience a sudden increase which we thus associated with the collapse of the listed tubes.

The use of nanotubes bundles has the advantage of being easily manipulated as well as producing an intense Raman signal due to the high number of tubes in the bundle. On the other hand, it does not give access to the single tube information as the spectra are the result of a collective behaviour of the ensemble of tubes. For the D-band particularly, while its frequency depends on the tube diameter, the variation is rather small and we observe an averaged central frequency in bundles samples[156]. For this reason, the evolution of A_D/A_G with pressure features a smooth monotone increase in contrast to the sharp drops observed in the RBM intensities. In order to access more detailed information on the tubes' collapse we decided to reduce the number of tubes going towards the study of an individualized tube to access more accurate values of the collapse pressure for which the results will be discussed in the next section.

3.4 Individualized SWCNTs at high pressure

The use of individualized nanotubes allows probing the Raman response of a single SWCNT diameter. In previous Section 2.4.1 we briefly described different methods for the tubes isolation. We will here focus on the method we used in our experiments based on the solvent assisted disentanglement of the bundles.

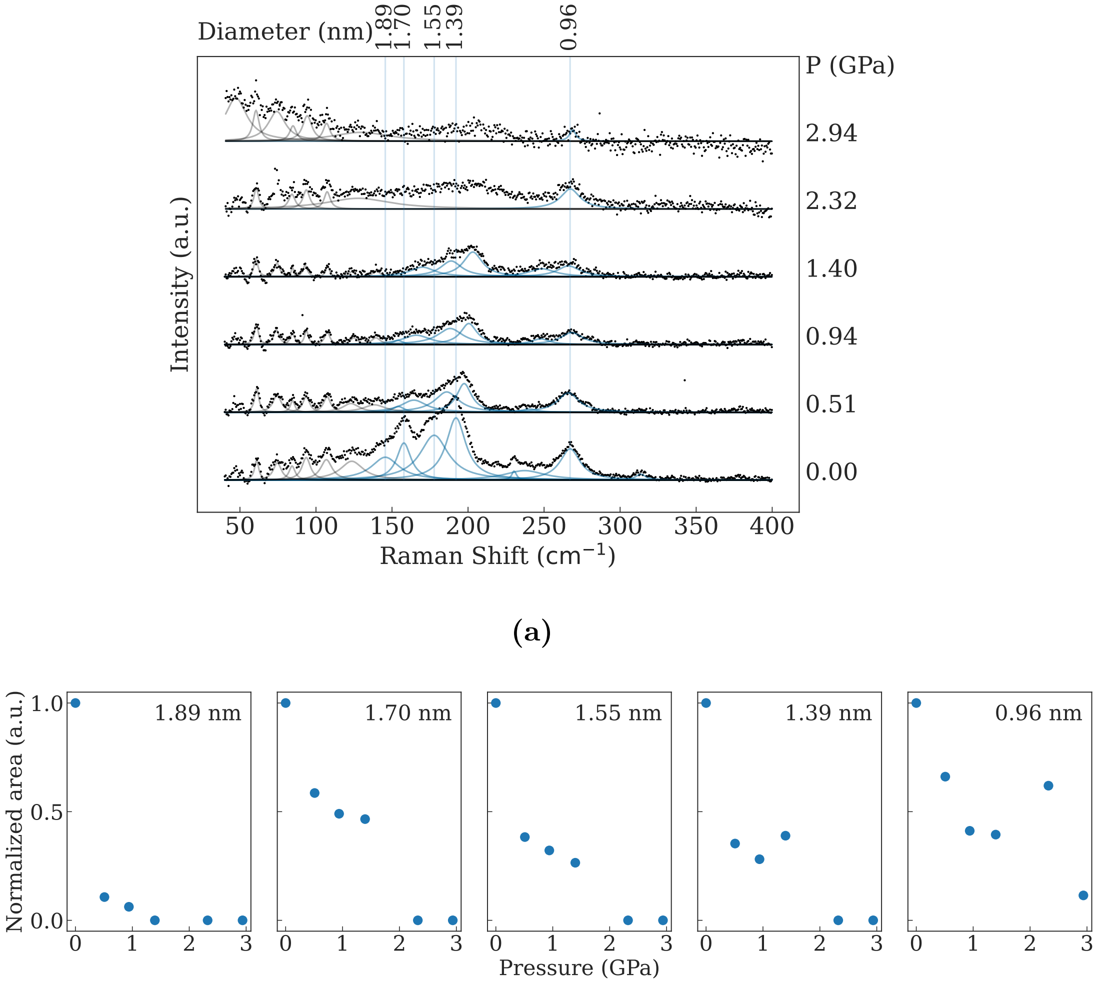

(a)

(b)

Figure 3.9: (a) Pressure evolution of the RBMs spectrum in the 4:1 Methanol-:Ethanol experiment. Grey Lorentzian peaks fit the air spectrum and blue ones the RBMs. Black dots show the measured spectrum. (b) Area of each RBM normalized to the lowest pressure point.

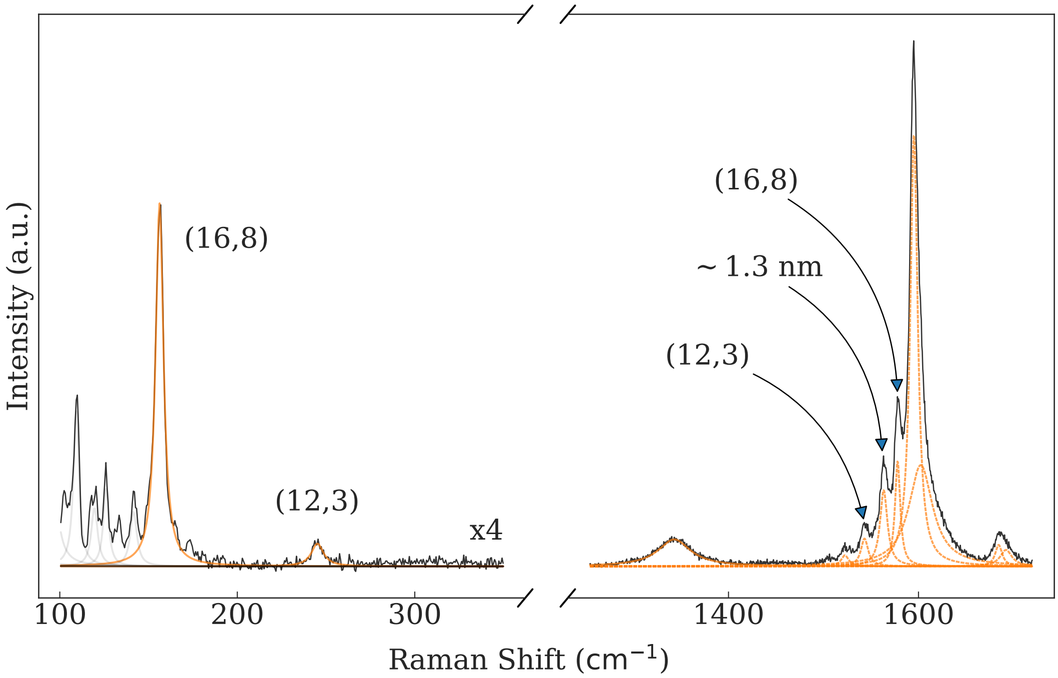

Figure 3.10: Raman spectrum of the individualized carbon nanotubes sample taken at ambient pressure. The RBMs at low frequency have been used to determine the tube's chiralities. Around 1600 cm^{-1} we observe the G-band peak with the highest peak being the G^{+}, common to all diameters and black arrows indicating the G^{-} peaks. The orange dashed line is used to show the G-band components.

3.4.1 Sample preparation and characterization at ambient pressure

For the isolation of the SWCNTs, a small quantity of powder is dispersed directly into a liquid solvent. 0.1 mg of the CNTs are diluted into 1 ml of N,N-dimethylformamide (DMF) which has proved to have a high efficiency in disentangling the bundles[157]. The solution is shortly sonicated for 15 minutes with a partial separation of the tubes and obtaining a light grey solution. Few small drops (100µL) of the liquid are deposited on the sapphire anvil and let dry. Raman spectroscopy was then used to find interesting samples by scanning the anvil using the Ramander cartography program (see Section 2.4.2). The advantage of using this technique to isolate the tubes is that with an easy and accessible procedure it is possible to find small bundles with only one or few resonant tubes. The RBM signal was used to discriminate the tubes distribution. The sample studied in our experiment was loaded together with the bundle sample of the nitrogen experiment of the previous section. The region where it was found is circled with a dashed line in Figure 3.4b. Its ambient Raman spectrum is shown in Figure 3.10. The RBM frequency can be used to identify the diameter of the tubes using Equation 1.13. We can note the presence of one strong peak around 155 cm^{-1} which was assigned to a (16,8) semiconducting tube of diameter 1.68 nm by matching the estimated

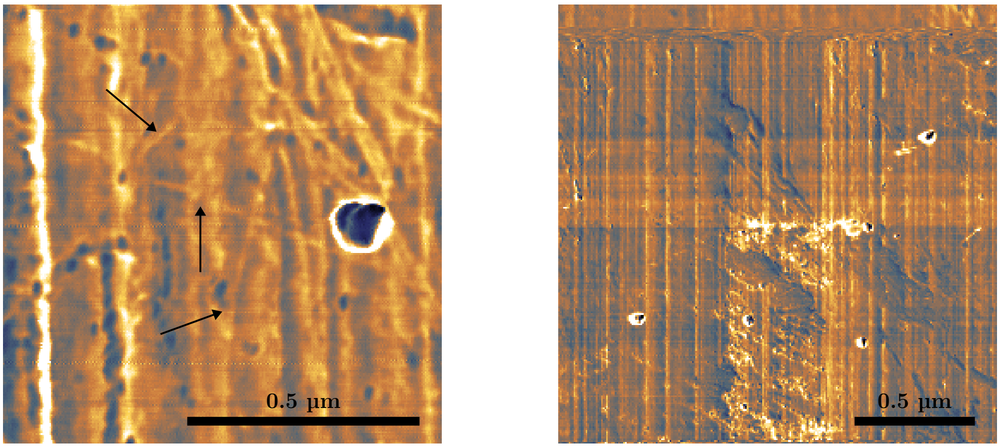

(a) CNTs **(b)** Background

Figure 3.11: Phase signal of the AFM imaging of the sapphire anvil. Black arrows show CNTs samples isolated from the bundles for few hundred microns.

diameter and imposing the resonance condition with the incoming laser light (see Section 1.2). A second, less intense RBM is identified with a smaller tube (12,3). In the same figure we can find at higher frequency also the D and G-band signals. The latter shows several narrow peaks, characteristic of semiconducting nanotubes. Using Equation 1.11 it is possible to estimate the diameter of the tubes from the frequency of the G^- band. We thus assigned two peaks to the two resonant tubes identified using the RBMs. This spectrum suggests that at least one more tube contributes to the G-band signal which we calculated being originated by a tube of diameter $\sim$ 1.3 nm. The absence of RBMs does not allow for the assignment of the tube's chirality as a great uncertainties is intrinsic to the results obtained using Equation 1.11.

In order to further characterize the sample we performed AFM imaging on the anvil. Figure 3.11a shows a scan performed around the region where we identified the presence of CNTs by Raman spectroscopy. Because of a large pollution of the anvil introduced by the deposition method we also scanned a region free of tubes which is shown in Figure 3.11b. Large vertical lines dominating the image are due to polishing marks on the anvil surface. By comparison between the two regions we identified the presence of CNTs separated by several hundreds of microns which are highlighted by black arrows in Figure 3.11a.

3.4.2 Pressure response of individualized tubes

The evolution of the G and D-bands spectra with pressure is shown in Figure 3.12. In these normalized spectra, a clear sudden transition modifies largely the tubes response when we reach 2 GPa. A drop in intensity of the signal is experienced marked by the increase of the signal to noise ratio as well as the relative augmentation of the intensity of the oxygen peak around 1550 cm^{-1}. Moreover, a large increase of the D-band relative intensity is also experienced. At 1.7 GPa the spectrum already appears modified, showing the first signatures of the nan-

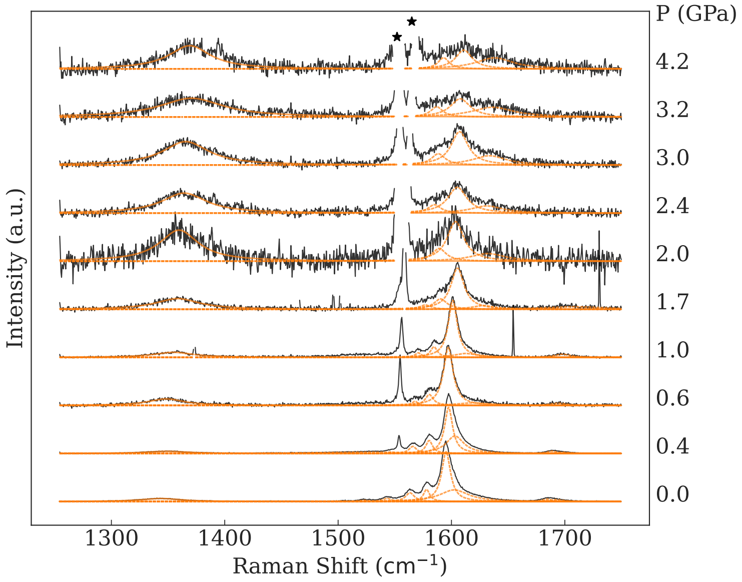

Figure 3.12: Normalized Raman spectrum evolution with pressure of the individualized sample. The data (black line) is fitted using Lorentzian functions for the D (solid orange lines) and G (dashed orange lines) bands. Black stars indicate the signal of oxygen inside (higher energy) and outside (lower energy) the cell.

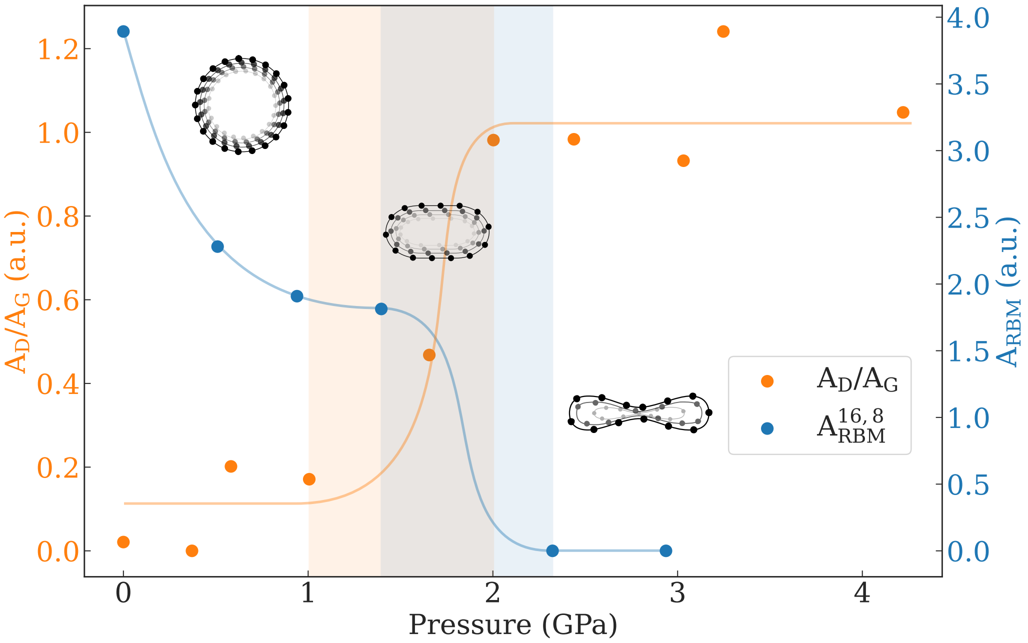

Figure 3.13: Pressure evolution of A_D/A_G of the individualized nanotubes (orange dots). The area of the RBM of the (16,8) tube extracted from the 4:1 Methanol:Ethanol experiment using the bundle sample is overlapped on the graph (blue dots). The solid lines are guide to the eye for the evolution of the two quantities with pressure. An orange and a blue rectangle have been added to show the intermediate oval transition measured in the two experiments.

otubes collapse. The large drop in signal is a confirmation of the theoretically predicted loss in signal due to collapse drastic modification of the electronic band structure[24, 158].

We performed a similar analysis to that carried out on the bundles samples in order to extract the values of A_D/A_G which are shown by the orange dots in Figure 3.13. A_D/A_G experiences a sudden change in behaviour between 1 and 2 GPa where after an initial flat response it rapidly increases until restabilizing to a higher value. The strong signal given by the (16,8) tube both in the G^- and RBMs signals suggests that the greatest contribution on the signal is given by this tube. We thus assigned those two thresholds of pressure to the beginning and the end of the collapse of this tube. Between those two values the tube undergoes a transient phase where it is found to be in an intermediate oval geometry. In contrast, an averaged monotone increase was observed in A_D/A_G when using nanotube bundles (see Figure 3.8).

Due to the impossibility of measuring the RBMs in this experiment due to the strong background introduced by the rotational spectrum of nitrogen (see Figure 3.3) a direct comparison with their signal is not possible. We could however extract the values of the RBM intensity corresponding to the (16,8) tube from the bundle experiment in 4:1 Methanol:Ethanol PTM (see Figure 3.9b) and overlapped its pressure evolution in Figure 3.13. A good agreement in the measured collapse pressure is found using the two independent methods i.e. the decrease of the RBM intensity in the bundle tubes and the rise of the D-band in the individualized ones. Study at the individual CNT level confirms the D-band evolution as a relevant signal to follow the high pressure collapse.

3.5 Conclusion

The series of experiments we described in this chapter aimed to characterize the use of the Raman D-band as a novel spectroscopic probe of the nanotubes collapse. The previous method used in literature for the detection of the tube's collapse was based on the disappearance of the RBMs signal, introducing the possibility of interpretation inconsistencies. Our method focuses on the appearance of a unique collapse signature given by the raise of a defect-free Raman D-band.

In order to study this signature the traditional diamond anvils used in high pressure experiments are not compatible due to their intense first order Raman signal. We demonstrated that sapphires can be efficiently used as a fruitful replacement for the fabrication of the anvils opening up to a wide range of opportunities in the high pressure study of carbon based materials.

In our study we performed high pressure experiments on SWCNTs both in bundle and individualized samples. Using the former it was possible to detect the first signatures of the tubes collapse using the D-band evolution with pressure. Moreover, we could follow the reversibility of the transition which shows an hysteresis character reducing the pressure at which the tubes pop back to their original tube-like shape. The analysis of the recovered samples, compared to the pre-characterization before the cycles, shows that the bundle returns to a similar state to that of departure, without evidences of tubes' damaging. This is an ulterior confirmation that the D-band originated at high pressure is not related to permanent structural modifications of the tubes, indeed agreeing that the geometrical transition to the flattened state is the underlining mechanism behind its origin. Finally, the use of two PTMs of different nature did not show significant differences in the nanotubes behaviour.

The study of individualized nanotubes was carried out in parallel to that of bundles samples. Using nitrogen as PTM it was possible to follow the evolution of a small bundle of only few tubes with a predominant signal given by a resonant (16,8) SWCNT. The collapse of this tube was highlighted by two clear signature which allowed for the identification of the beginning and the end of the nanotube's collapse. First, the overall tube signal suddenly drop when reaching 2 GPa. When the geometrical transition occurs, a strong modification of the electronic structure is expected which shifted the energy resonance condition. The result is the rapid drop in the Raman intensity that was experienced by our sample. The other clear signature of the tube's collapse was given by the relative increase of the D-band intensity compared to the G-band. The parameter A_D/A_G was efficiently exploited for the description of the transition which shows a step like evolution with a smooth transient phase between 1 and 2 GPa associated with the establishment of intermediate oval geometries.

To conclude, a good agreement was found between the studies we performed in different experimental conditions. This confirmed the importance of the characterization of the D-band evolution with pressure as well as establish the solidity of our method to detect the nanotube's collapse. Using individualized tubes gives access to the possibility of performing chirality resolved study of the nanotubes properties at high pressure. Moreover, those samples open up opportunities for the detailed characterization of the physics of intermediate states between the circular and flattened geometries which can be compare to existing[159, 160] and novel theoretical models.

Chapter 4

Environmental tuning of graphene's properties at high pressure

4.1 Introduction

In the previous chapter we described the experimental results we obtain on the study of pressure effects on carbon nanotubes. In the present one we will step up in dimensionality by focussing on the results of our experiments conducted on two-dimensional systems. Our aim was to get a further comprehension of the environmental effect on the pressure response of those materials. To achieve that we performed a series of experiments pairing different combinations of substrates and pressure transmitting media in a way that we could identify each of their contributions with a specific physical response. We will divide the discussion between three main topics.

To understand the role of the substrate on the pressure response of 2D systems we engineered Si/SiO$_2$ substrate for graphene suspension at high pressure. In Section 4.3 we will present our results using those substrates with CVD grown bilayer graphene samples at high pressure in 4:1 Methanol:Ethanol PTM. In Section 4.4, we used thin few-layer graphene samples for testing different suspending geometries as well as showing the effect of changing the PTM from 4:1 Methanol:Ethanol to water.

Finally in Section 4.5 we studied the necessary conditions for the formation of a two-dimensional diamond like structure, referred as diamondene in the literature, from few-layer graphene. A combined mechanical and chemical interaction introduced by the PTM and the substrate triggers the formation of sp^3 bonds between the graphene layers at pressure as low as ~ 6 GPa.

Due to the great importance of the substrate in our studies, before entering into the details of the experimental results we will first describe in the next section the different Si/SiO$_2$ substrate designs we employed in our experiments.

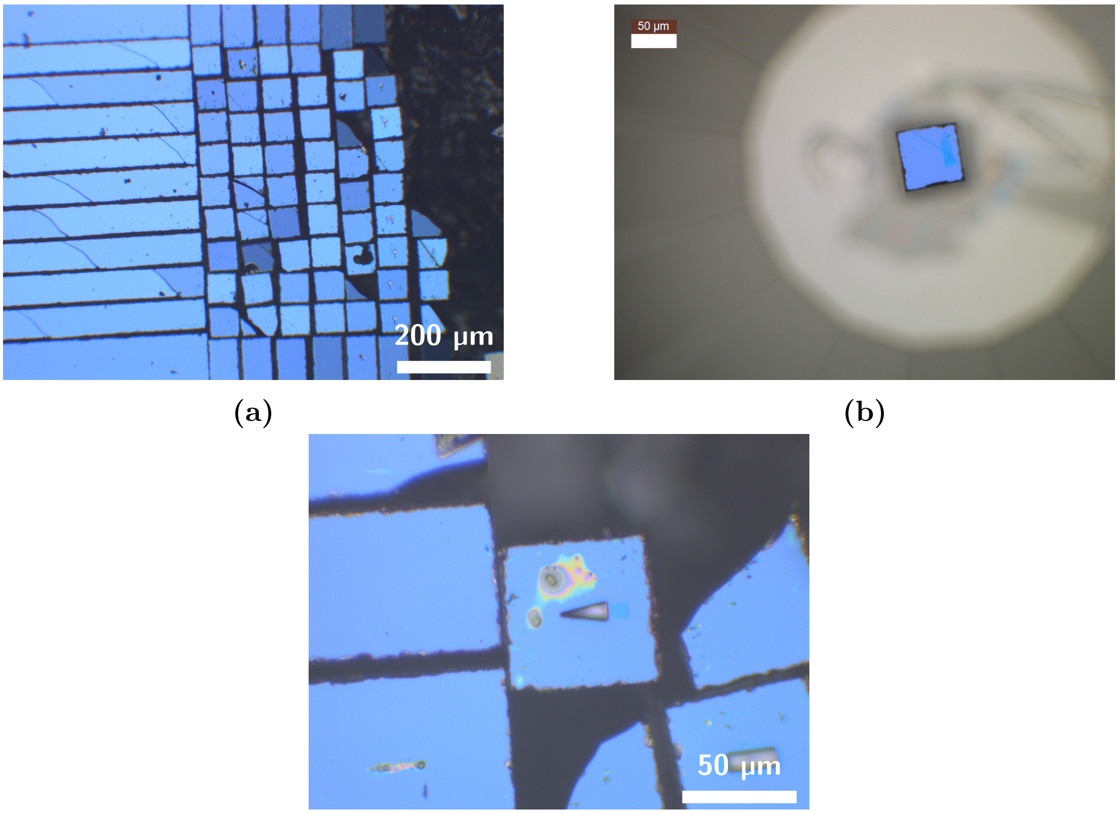

(a) (b) (c)

Figure 4.1: Si/SiO$_2$ substrates for high pressure experiments on (a) their fabrication site and (b) after it is transferred on the anvil. (c) One of the cubes where a triangular hole for suspension was drilled using FIB.

4.2 Fabrication of Si/SiO$_2$ substrates for high pressure

We have already introduced in Section 1.5.1 that the most common substrate used for 2D materials is formed by a thin layer of silicon oxide on top of silicon (Si/SiO$_2$). Due to its widely spread use, it is of great importance to characterize its interaction with 2D samples when submitted to high pressure. However, in order to be used in the DAC, we had to made dedicated adaptation for its compatibility with high pressure experiments. The main experimental restriction concerns the substrate size which has to fit the gasket hole. Moreover, we had to take into account the gasket hole shrinking with increasing pressure both in the lateral and axial directions. Finally, the substrate needs to be sufficiently easy to manipulate to be placed at the centre of the diamond anvil without damaging it. We thus engineer two independent fabrication methods which allowed to either place the substrate on the anvil and then transfer the desired sample on it or placing the substrate on the anvil with the transferred sample already on it.

The first method, designed by former PhD student Alexis Forestier, consisted in cutting a thin Si/SiO$_2$ foil of 50 µm in thickness into small cubes of $\sim$ 50 µm in size.

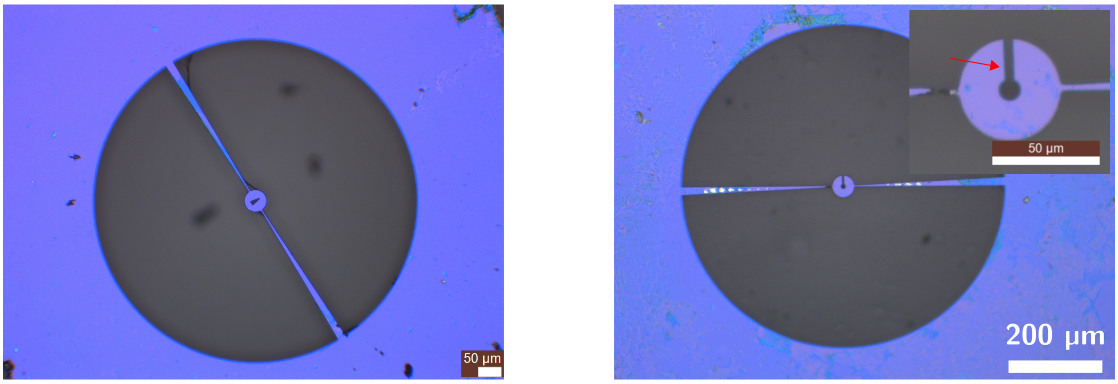

(a) **(b)**

Figure 4.2: Two examples of substrates made by lithography featuring weak-links for systematic transfer. (a) features a triangular hole and (b) a key-like shape with a central hole and an aperture (red arrow in the inset) for facilitating the entrance of the PTM.

The foil was cut using a diamond saw in the x and y direction resulting in a squared area filled with cubes. Figure 4.1a shows some of the substrates obtained using this procedure. Using a thin needle, a specifically chosen cube-shaped substrate can be collected and dropped at the centre of the anvil as shown in Figure 4.1b. The substrate is then ready for sample deposition using the techniques described in Section 2.4.1. Using this method few hundred substrates can be fabricated in few hours and the sample can be safely transferred without risk of damage.

With the aim of studying suspended samples at high pressure we ulteriorly manufactured the cubes by carving small trenches using the focus ion beam (FIB) technique. We shaped the trenches into triangles as shown in Figure 4.1c which have a base of ∼ 7 μm, a height of ∼ 20 μm and few microns in depth. This shape allowed for compatibility with the high range of sample morphologies that characterizes mechanically exfoliated samples and leaving a great flexibility on the amount of suspended region we wanted to study.

The second substrate design we fabricated was build with the purpose of transferring graphene before placing the substrate on the anvil. In such a way we could simultaneously prepare several samples by transferring large surface CVD grown graphene. Two of the substrate we designed are shown in Figure 4.2. A small circular disc with diameter ranging from 50 μm to 120 μm was carved into the 50 μm thin Si/SiO_2 foil using lithography. These substrates were prepared by our colleagues of Institut Néel, Grenoble (L. Marty et al.). Due to the risk of sample damaging introduced by the needle manipulation involved with the previous substrates we optimized the substrate pick-up and drop-off procedure. Two weak links attached the disk to the rest of the foil at a distance of ∼ 400 μm. To transfer the sample we used micro-manipulated thin tweezers which could be used during microscope inspection of the substrate. The weak links are broken using the tweezers and the disk attaches to it by simple electrostatic force. The sample was then carefully dropped on the anvil with minimal risk of damaging. Small trenches for suspended sample studies were also integrated in the disks. Beside the triangular shape used in the cube samples (Figure 4.2a) we produced a batch of substrates featuring a circular holes as shown in Figure 4.2b. A red arrow in the magnified inset indicates a small escape channel which was also added to ensure that the PTM could easily fill the trench reducing the risk of breaking the sample. For both shapes, the hole was fully traversing the whole substrate.

Once deposited on the anvil the Si/SiO_2 substrates needed to be glued in order to avoid moving during either the transfer of graphene or the PTM loading. We used an UV optical-curing glue for this purpose (Norland Optical Adhesive 81) for which a thin layer was placed underneath the substrate. Only few minutes of curing was sufficient to guarantee that the substrate would not move during the sample preparation or the experiment.

Thanks to those two fabrication methods it was possible to integrate the use of Si/SiO_2 substrate into the DAC experiments. We will show in the following sections the results that could be obtained using them in high pressure experiments.

4.3 Strain and doping in the suspended/supported bilayer graphene binary system

In Annex A we describe a series of experiments on thin few-layer graphene samples which showed that both the substrate and the PTM can strongly interact with graphene at high pressure. By reducing the number of graphene layers in the studied sample we expect that the effect of this interaction will be amplified due to a higher density of superficial atoms in the limit of mono and bilayer samples where the totality of the atoms are on the surface. Driven by those principles, we focused our study on bilayer samples where the interaction between the two adjacent layers can additionally induce interesting phenomena. The aim of our study was to deeper understand the complex interactions that are involved in the few atom thick system substrate-bilayer graphene-PTM.

The core innovation of our study is the use of the drilled substrates we introduced in Section 4.2. The binary system that originated after transferring the sample onto the substrate i.e. supported and suspended bilayer graphene, opens up the opportunity to study, within the same pressure run, the sample subjected to different environmental conditions. Furthermore, this approach allows for the disentanglement of substrate and PTM contributions to the evolution of graphene's features.

In order to clearly characterize the signatures of the suspended and supported regions we performed our experiments using the Proxima DAC which allows for high pressure spatially resolved measurements using the Mitutoyo diamond corrected x100 objective (see Section 2.2.1). This allowed to perform detailed high pressure Raman mapping measurements of our sample by using the Ramander controlling software (see Section 2.4.2). We will describe in this section the technological developments and the experimental results of our study.

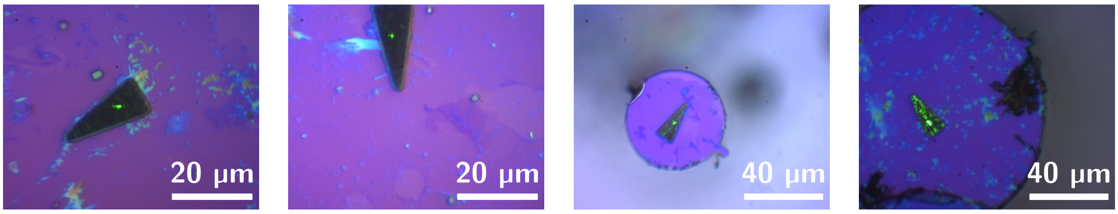

(a) (b) (c) (d)

Figure 4.3: Optical images of BLG on Si/SiO$_2$. They show some of the failed attempts of using the triangular shaped hole for suspension of CVD grown BLG.

4.3.1 Sample transfer and first attempts

The study of suspended bilayer samples at high pressure encounter several challenges due to the fragility of the system. In particular the PTM loading phase is extremely delicate as the strong capillary forces that are involved when the PTM enters the suspended region risk to severely damage the sample. We conducted our experiments using 4:1 Methanol:Ethanol in order to preserve hydrostatic conditions up to $\sim$ 10 GPa as well as for its relatively easy and controlled loading procedure that can reduce the risk of breaking the suspended part of the sample.

Due to the exploratory nature of our study we opted for CVD grown samples in our experiment in order to systematically produce large area samples. We thus used the round disk substrate held by weak links shown in Figure 4.2a. The substrates and bilayer samples were prepared by the Läetitia Marty group at Institut Néel in Grenoble (France). After the substrates fabrication two subsequentially transfers of CVD grown monolayer graphene were employed for the preparation of the bilayer samples.

The first batch of substrates was featuring a traversing triangular hole for suspension. Figure 4.3 shows few attempts of loading the DAC with 4:1 Methanol:Ethanol after placing and glueing the sample on the diamond anvil. All of those attempts showed the absence of sample signal after the cell was filled with PTM which was probably damaged by the PTM entering in the hole through the sample.

In order to avoid the damaging of the suspended part of the sample we changed the geometry of the system by including a channel for filling the trench from the side and replaced the triangular shape hole by a circular one as shown in Figure 4.2b. With this geometry I loaded a new sample which successfully remained intact after the PTM's insertion in the chamber. Figure 4.4a and Figure 4.4b show the sample imaged with the open, and loaded DAC respectively. In Figure 4.4b a red arrow indicates the faint contrast at the edge of the sample that ensures the sample presence in the suspended region.

4.3.2 Bilayer graphene characterisation via Raman mapping at high pressure

In order to characterize the sample and study the effects of introducing the alcohol PTM both on the suspended and supported regions I performed a Raman spectral

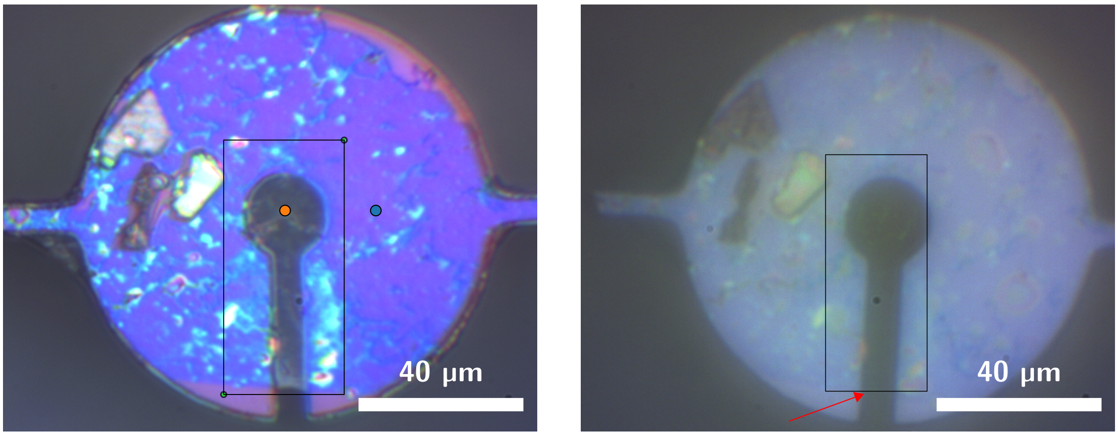

(a) Ambient **(b)** 0.6 GPa

Figure 4.4: Optical image of the sample before (a) and after (b) loading. A black rectangle indicate the region that have been mapped through Raman spectroscopy. In (a) an orange and a blue dots show the points measured throughout the pressure cycle, later referred as Suspended and Supported respectively. A red arrow in (b) points to the BLG edge to indicate a faint contrast that confirms the presence of the sample in the suspended region.

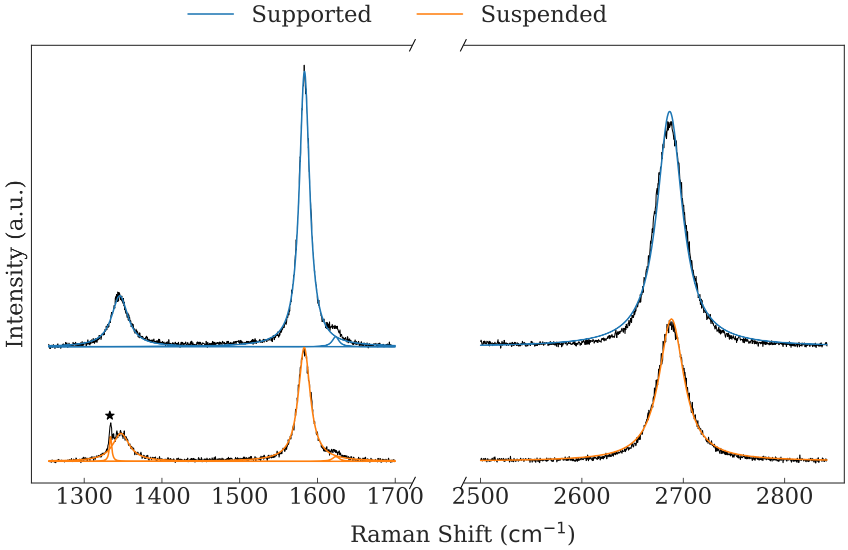

Figure 4.5: Ambient pressure BLG typical spectra measured at the centre of the substrate hole (Suspended: orange dot in Figure 4.4a) and on the substrate (Supported: blue dot in Figure 4.4a). The black line shows the experimental data, and the orange and blue lines the Lorentzian functions that fit the suspended and supported data respectively. A black stars marks the Raman peak of diamond anvil seen through the trench. The spectra are not normalized and they are acquired at the same power and acquisition time.

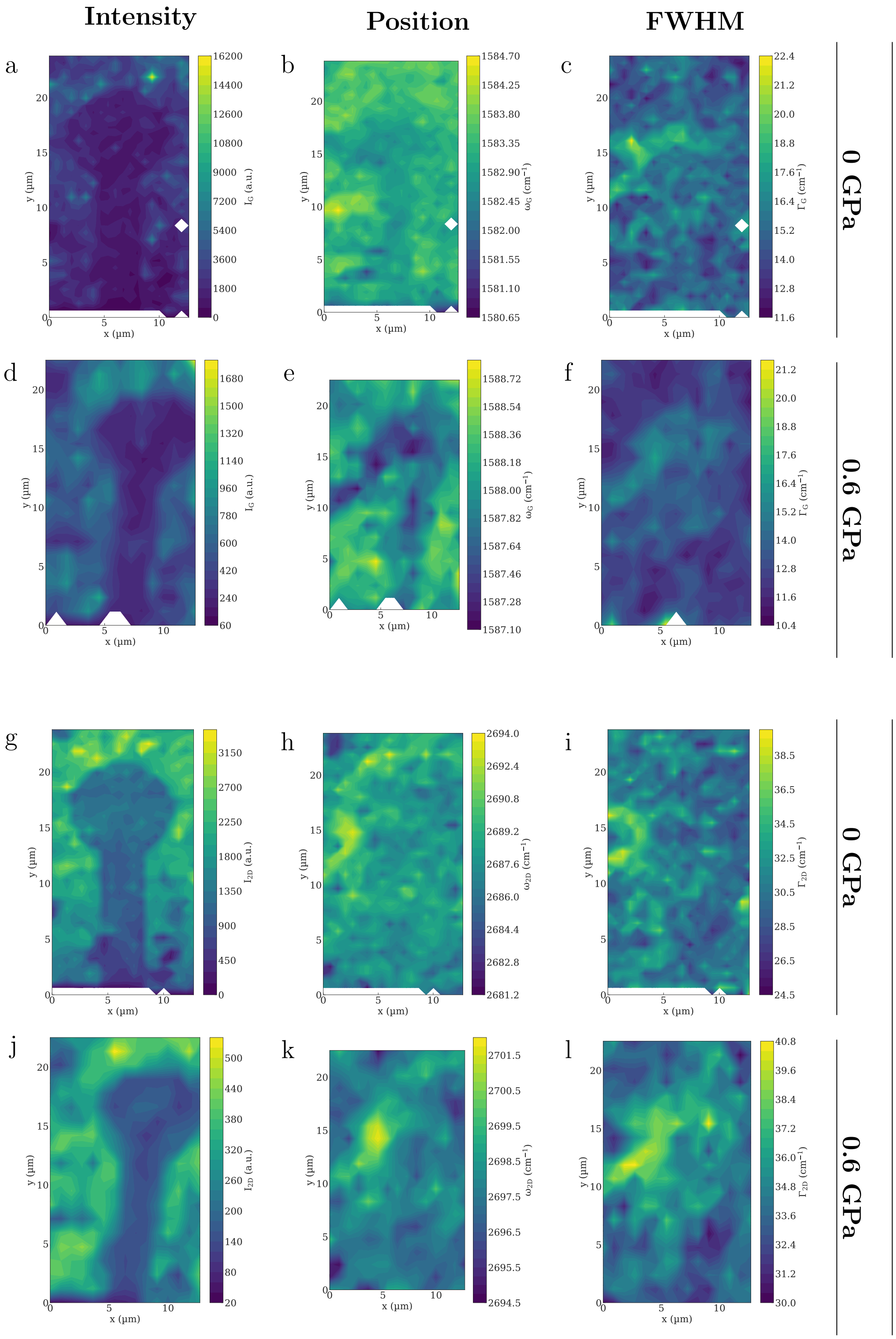

Figure 4.6: Raman mapping of the sample showing the fitted parameters for the G and 2D-band measured at ambient pressure and at 0.6 GPa. The scanned region is highlighted by two black rectangles in Figure 4.4.

cartography of the sample before and after the loading (at 0.6 GPa). The scanned regions are highlighted by black rectangles in Figure 4.4. A typical spectrum of the suspended and supported regions, taken at ambient pressure in correspondence of the orange and blue circles in Figure 4.4a, is shown in Figure 4.5. The Raman features of the bilayer graphene could be well fitted using single component Lorentzian peaks. We can see that the signal of the supported region is strongly enhanced by interference effects of the substrate resulting in a G-band more then twice as intense in the supported region. Moreover, the individual peak identifying the 2D-band indicates that the studied bilayers are composed by two graphene layers in a turbostratic stacking different from the graphitic Bernal stacking (Section 1.1)[161]. Indeed, during the two step transfer procedure for the preparation of the samples, we did not have control on the relative orientation of the two graphene crystals transferred. From our data it was not possible to identify the exact twist angle of the final bilayer sample. Finally the presence of small D and G′ bands indicate that the sample is partially defected. A curious detail is marked by the black star in Figure 4.5 which is only present in the suspended region. The peak originates from the Raman first order signal of the diamond anvil beneath the substrate. Whilst normally this signal is a source of spectral pollution it has been efficiently used in this experiment to systematically distinguish the suspended and supporter regions in our mapping at ambient pressure.

The fitted parameters for the totality of the scan are displayed in Figure 4.6. The first column showing the G-band (a,d) and 2D-band (g,j) intensities sticks out, well defining the shape of the trench. Moreover, we can appreciate that using our spherical aberration corrected objective we can get a clear definition of the shape of the suspended region even if the hole sides are partially blurred out. Nevertheless, a sufficiently large area is identified at the centre of the circular region, removing any doubts of mixed suspended-supported signal. While the other quantities seem to be less sensitive to the presence or not of the underlying substrate, the G-band position (b,e) shows clear differences in the two regions with a more accentuated contrast when the cell is loaded (e). To help the visualization of the individual parameters, the variables frequency count is plotted in the histograms in Figure 4.7. We can observe a neat separation in the G-band frequency ω_G between the two regions both at ambient pressure and at 0.6 GPa with a redshift of the frequency in the suspended region. The G-band FWHM Γ_G also shows a significant difference with a larger peak in the suspended area. By contrast, no clear differences are shown for the 2D-band frequency ω_{2D} and FWHM Γ_{2D}.

4.3.3 Pressure evolution of the Raman features of bilayer graphene

Together with Dr. Rajaji Vincent I monitored the two regions shown in Figure 4.4 in a pressure run up to 5.9 GPa. Above this pressure the top anvil diamond touched the sample so we stopped the experiment. The evolution of the G and 2D bands with pressure is shown in Figure 4.8. A similar evolution is observed for the spectra in the two regions at low pressure with a blue shift of the suspended features at higher pressure. The fitted parameters are plotted in Figure 4.9. A purple dashed

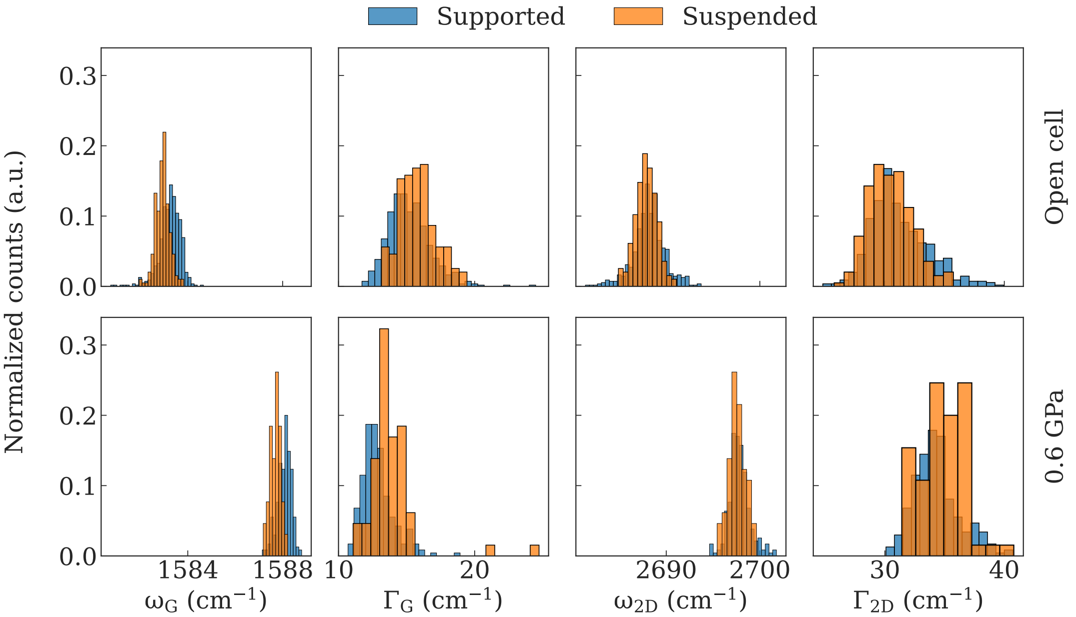

Figure 4.7: Histograms showing the frequencies of the parameters of the G and 2D-bands extracted from the Raman cartography in Figure 4.6.

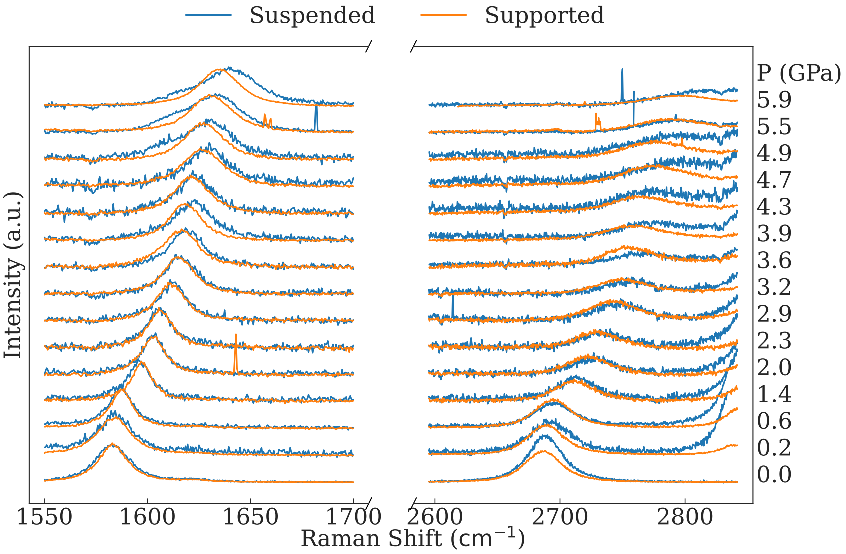

Figure 4.8: Raman spectra of the suspended and supported bilayer graphene collected in the high pressure run. The two regions correspond to the G-band (below 1700 cm^{-1}) and the 2D-band (above 2600 cm^{-1}). The spectra are normalized to the G-band maximum intensity for each pressure.

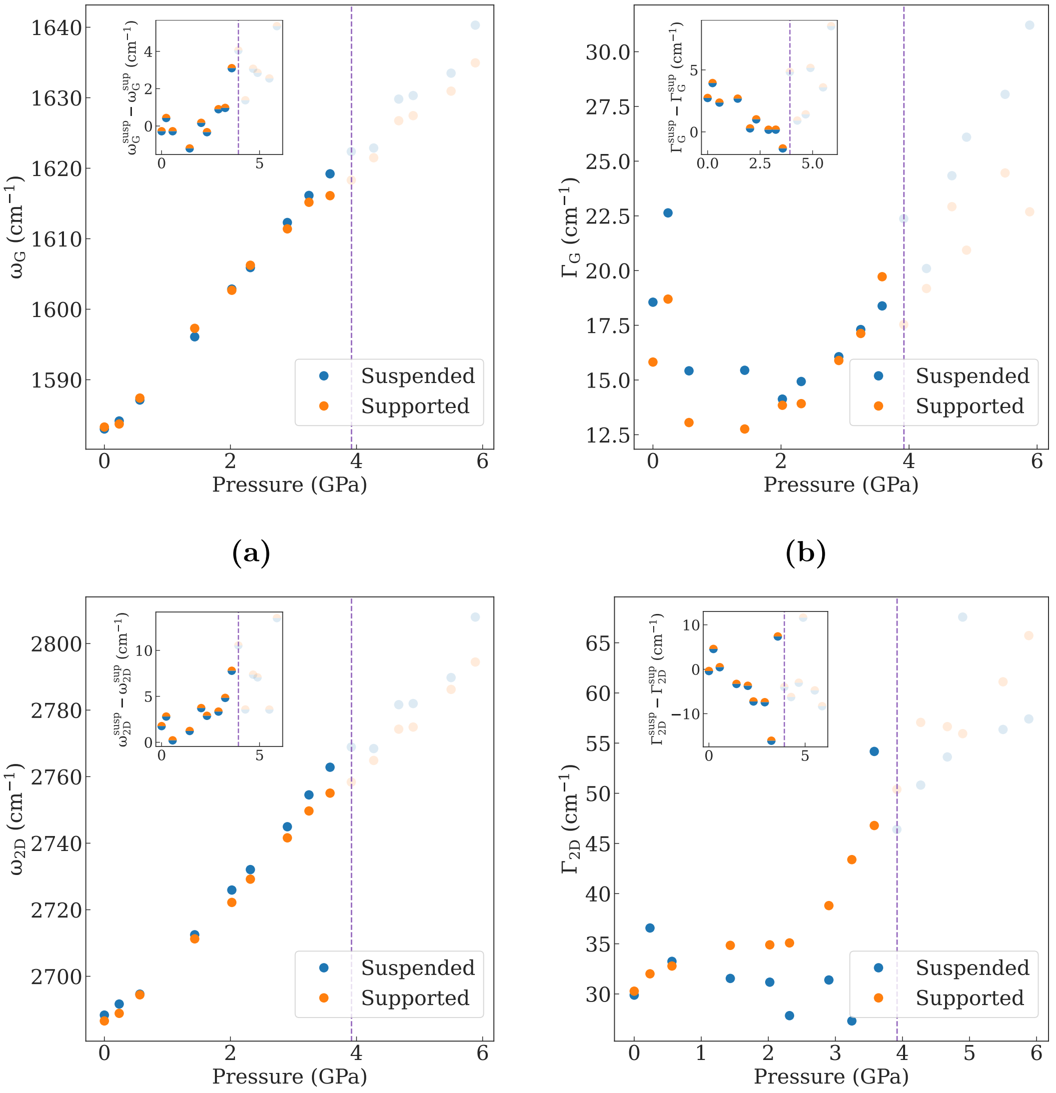

(a) **(b)**

(c) **(d)**

Figure 4.9: Pressure evolution of the fitted G and 2D bands parameters for the spectra in Figure 4.8. A purple dashed line highlights the delamination of the oxide layer of the substrate. The pressure points above this pressure have been faded as they have not been taken into consideration in our analysis but they have been reported for completeness. The insets in each figure show the pressure evolution of the difference between the corresponding parameter measured in the suspended and supported regions.

line highlights the pressure at which the SiO_2 layer delaminates, occurring at 3.9 GPa. The points above this pressure have been faded as this transition severely compromise the interpretation of the experimental results but they have been kept for completeness. We will thus focus on the lower pressure region in our analysis. We observe a similar evolution of the frequencies both for the G-band (Figure 4.9a) and the 2D-band (Figure 4.9c). A small blueshift is observed in the case of ω_{2D} in the suspended region above 2 GPa. In the insets we plotted the difference between the frequency of the suspended ω_i^{susp} and supported ω_i^{supp} graphene ($i = G, 2D$) helping the visualization of the small splitting of ω_{2D} with increasing pressure. This first result is quite striking as intuitively we would expect a larger blueshift in the supported graphene. The major contribution of the G-band and 2D-band shift with pressure is introduced by the biaxial strain of the substrate[34, 36, 45]. Those results indicates that the strain is efficiently transferred from the supported to the suspended part of the sample. Beside strain when using 4:1 Methanol:Ethanol as pressure transmitting medium previous groups reported an important doping of graphene[34, 44]. In our case this is also observed by the strong decrease of Γ_G at low pressure (see Section 1.5.3). While the value of Γ_G is lower in the supported region, the inset showing the difference between the width of the suspended and supported graphene $\Gamma_G^{susp} - \Gamma_G^{susp}$ indicates that, relatively, Γ_G^{susp} get thinner with increasing pressure. This effect could be explained by a larger amount of charges injected in the suspended region due to the presence of the PTM on both sides of the sample. On the other hand, another possibility is that a local inhomogeneous strain field is present on the suspended graphene due to the substrate's roughness. The observed G-band is thus averaged over the probing laser spot size resulting on the strong widening of the G-band width in the supported region. This second option is backed up by the observed increase of Γ_G above 2 GPa. Furthermore, when we look at the 2D band width in Figure 4.9d we observe a different trend in the two regions. The 2D-band is fairly constant before delamination beside a singular point at 3.6 GPa. This result is compatible with the observations of Froelicher et al. in electrochemically gated samples shown in Figure 1.15b where the width of the 2D band is found not to be affected by doping[70]. On the other hand, the supported BLG feature an increase of Γ_{2D} which is more marked above 2.3 GPa supporting the hypothesis of a inhomogeneous strain field introduced by the substrate. In reality the mutual contributions of both effects is the most probable scenario.

Finally, the close observation of Γ_G in Figure 4.9b at the first pressure point at 0.2 GPa is found to be higher than the ambient pressure point. We can explain this peculiar signature by the presence of an opposite charge doping of graphene at ambient conditions which is neutralized when pressure is increased. Several groups have reported the presence of partial doping of graphene at ambient pressure principally due to impurities on the substrate as well as to environmental pollution[32, 33, 94].

In order to clearly discern the doping and strain contributions of graphene's Raman features we performed a similar procedure to that followed by Lee et al. (Section 1.5.4) which will make the object of the following section.

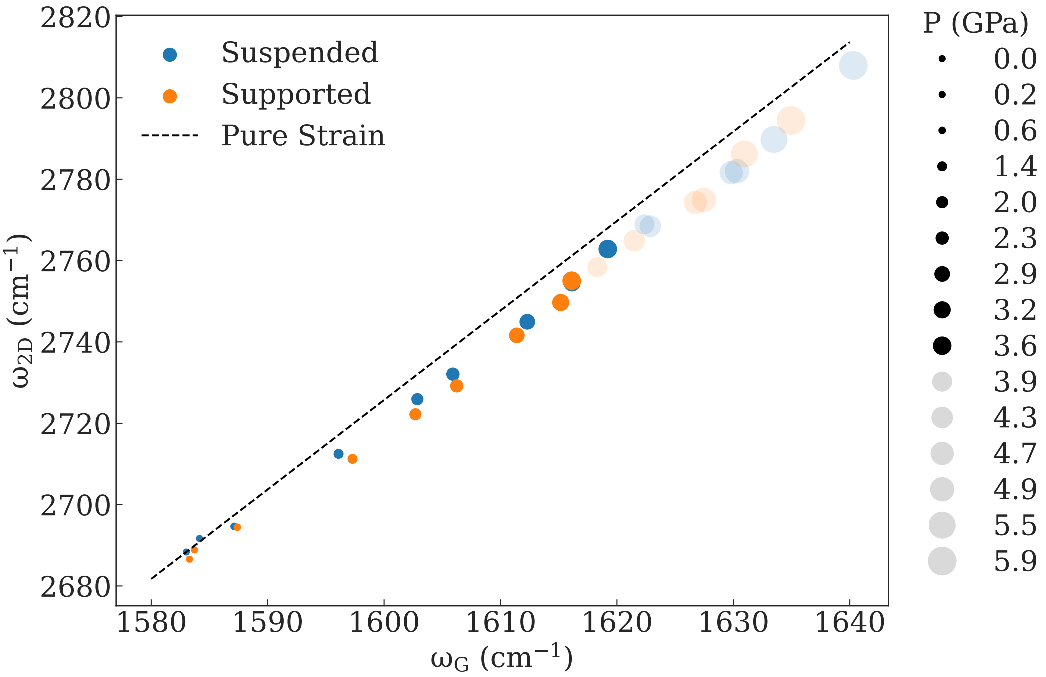

Figure 4.10: Correlation plot for the 2D-band frequency ω_{2D} as a function of the G-band frequency ω_G. A black dashed line indicates the slope the points would have to lay on in the case of pure biaxial strain transfer. A pressure scale has been defined by sizing the markers proportionally to pressure.

4.3.4 Disentangling strain and doping contributions

The procedure proposed by Lee et al. for disentangling the strain and doping contributions on graphene is based on the study of the correlation of ω_G and ω_{2D}. The plotted values for our experiment are shown in Figure 4.10. Each point have been sized to show the pressure at which the data was acquired. The slope $\partial\omega_{2D}/\partial\omega_G$ is found to follow the black dashed line in the case of pure strain applied to graphene. The latter corresponds to a slope $(\partial\omega_{2D}/\partial\omega_G)^{strain} = 2.2$[69, 68] crossing the suspended ambient pressure point. We note that most of the points lay in the region beneath. This evidence indicates that strain alone is not sufficient to describe the pressure evolution of the G and 2D-bands but doping must also be included. We thus calculated the strain ϵ and the charge carrier density n levels relative to the ambient pressure values (for details refer to the review of Bendiab et al. on the subject[73]). The evolution of the two quantities are shown in Figure 4.11a and Figure 4.11b. Due to the impossibility of knowing in our experiment if doping was introduced by holes (h^+) or electrons (e^-) we calculated doping and strain for the two scenarios.

For what concerns ϵ (Figure 4.11a), we obtain the remarkable result that there is no significant difference between the suspended and the supported regions within our experimental resolution. This apparently counter-intuitive results indicate that our suspended bilayer graphene acts as a rigid membrane efficiently transferring

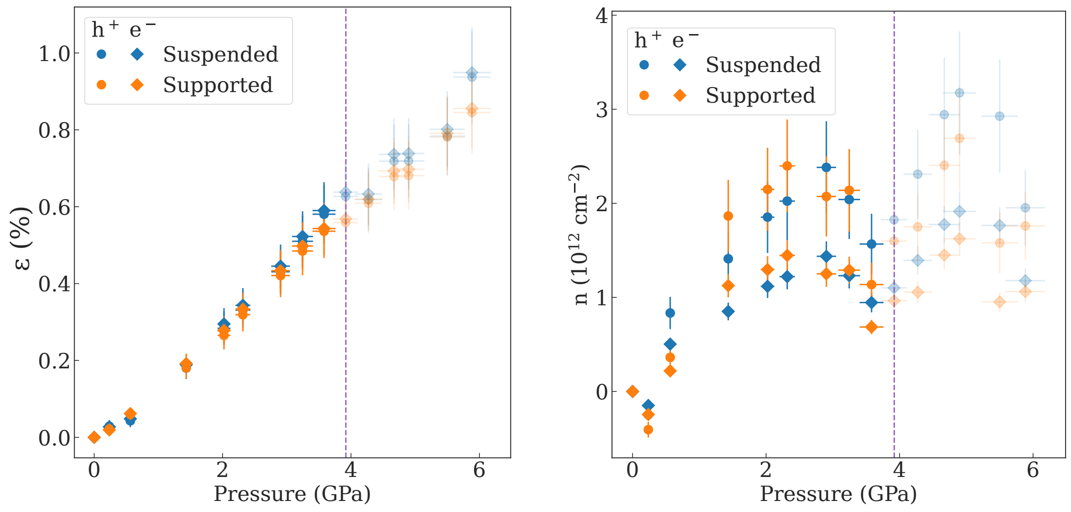

(a) **(b)**

Figure 4.11: Calculated biaxial strain ϵ and doping n on the suspended and supported bilayer regions as a function of pressure. Solid circles have been used for the results calculated in the hypothesis of hole doping (h^+) while diamond symbols in the case of electron doping (e^-).

the strain from the substrate to the suspended region. A monotone, almost linear increase with pressure is observed. This observation suggests that the strain transfer efficiency from the substrate to the sample does not strongly depends on pressure.

The plot of the evolution of n confirms the hypothesis of pressure induced doping effects in graphene peaking values of $\sim 2.4 \cdot 10^{12}$ cm^{-2} for the hole doping scenario and $\sim 1.4 \cdot 10^{12}$ cm^{-2} for electron doping. Within the experimental uncertainties the doping levels are equivalent in the two regions, for the majority of the data points. A small additional doping of the suspended region is observed at low pressure compatible with a doping effect induced by the PTM sandwiching the BLG on two sides. Above 2 GPa n peaks to its maximum value retaining a seemingly constant behaviour until delamination of the substrate occurs. It is interesting to note that, similarly to what was observed in the evolution of Γ_G, we observe a decrease of the charge density at 0.2 GPa. This observation confirms our hypothesis of an inversion of the type of charge carrier from ambient condition to the pressurized system.

4.3.5 Conclusions

We reported in this section our results on the study of the pressure response a bilayer sample which was partially suspended on a drilled substrate. To our knowledge this is the first reported case of such a system studied at high pressure. Due to the sample fragility several attempts failed leading to find that the best geometry for suspension necessitates for a lateral aperture in the substrate to let the PTM easily enter the hole underneath the suspended sample.

The sample has been thoroughly characterized by Raman cartography before and after the PTM insertion in the DAC. This allowed us to identify the G-band as the mainly impacted feature by the suspension. To our knowledge this is the first case of a Raman cartography measurement at high pressure. Following the evolution of the Raman features at high pressure we identified the signatures of both doping and strain induced in our sample. To disentangle the individual effects of each contribution we plotted the evolution of the 2D-band frequency against that of the G-band. Our result shows that both strain and doping are not strongly affected by the suspended geometry, attending comparable values within the studied pressure range and uncertainties. Finally, the charge carrier density is shown to saturate fairly quickly within the first 2 GPa from where it becomes constant. We obtained at its maximum value $(2.4 \pm 0.5) \cdot 10^{12}$ cm^{-2} and $(1.4 \pm 0.2) \cdot 10^{12}$ cm^{-2} in the hypothesis of hole and electron doping respectively.

The use of bilayer samples in the suspended geometry is limited by the sample fragility. For this reason we performed several other experiments in this geometry using few-layer graphene samples allowing us to explore the use of different pressure transmitting media as well as changing the sample geometry. Our results in this topic will make object of the following section.

4.4 Suspended few-layer graphene at high pressure: geometrical and chemical effects

In the previous section we introduced the interest of studying samples which are both suspended and supported on a substrate. The use of such a geometry allows us, within the same experiment, to compare the evolution of a sample submitted to two different environments at high pressure and extract the salient features which emerge from it. In this section we continued studying such systems but focusing now on the use of thin few-layer graphene (FLG) samples. A first initial series of experiments we will be showing the results on samples immersed in the same PTM, 4:1 Methanol:Ethanol, but placed in different geometric configurations on the suspended region. These results will be shown in Section 4.4.2. In the following section, Section 4.4.3, we conducted experiments on suspended FLG using pure water as PTM identifying strong differences in the pressure evolution in the two regions.

4.4.1 Suspending graphene

We prepared our samples by mechanical exfoliation of bulk graphite onto PDMS. The samples were then transferred on silicon cubes with triangular trenches by room temperature stamping. The suspension of FLG samples over trenched substrate involves taking extreme care in the transfer process. The suspended area reduces the contact surface between the substrate and the sample thus limiting the success rate of the transfer process. A major improvement was achieved by the upgrades on the new transfer system I performed during my thesis. In order to increase the probability of successfully transfer the sample, when the PDMS is

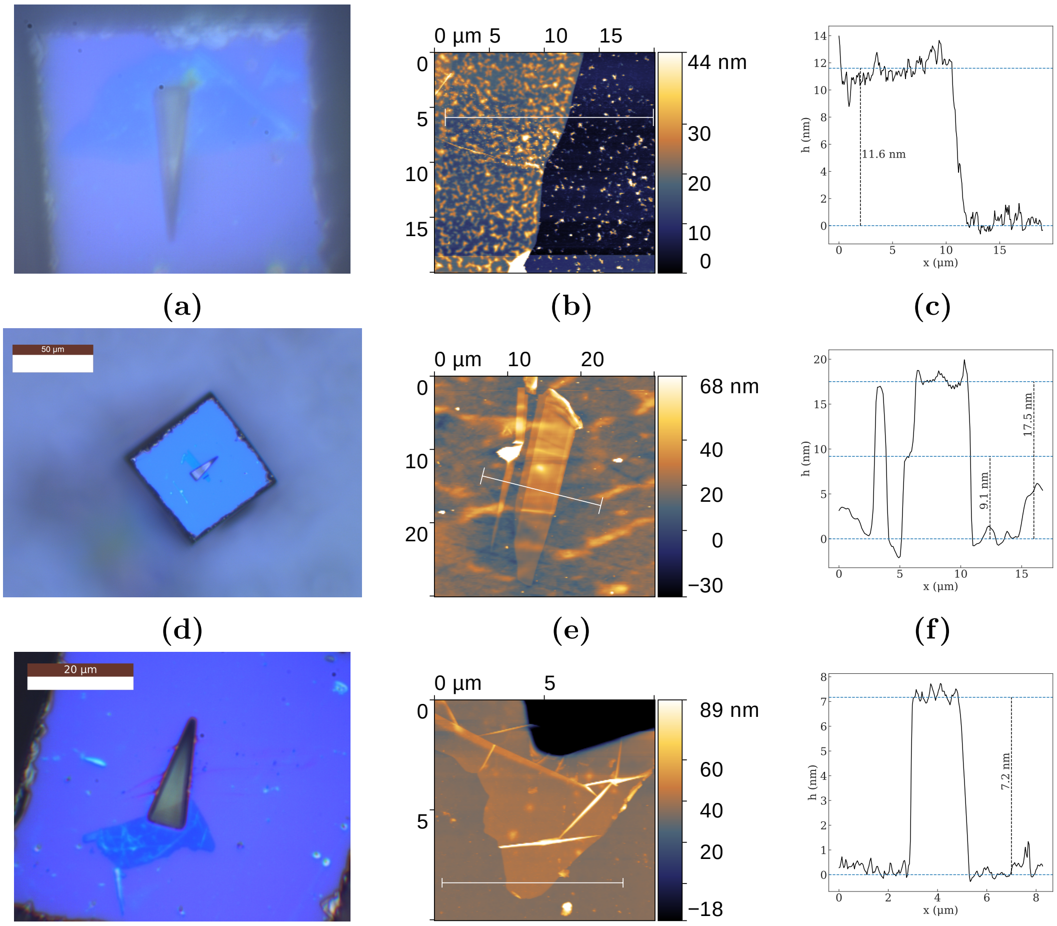

(a) **(b)** **(c)**

(d) **(e)** **(f)**

(g) **(h)** **(i)**

Figure 4.12: Optical images of the samples used in our studies of suspended FLG in 4:1 Methanol:Ethanol (a,d) and in water (g). AFM imaging of those sample (b,e,h) was used to measure the height profiles (c,f,i) in correspondence of the white solid line.

slowly removed after contact with the target substrate, it is necessary to maximize the peeled off sample surface before reaching the suspended region. The already transferred fraction of the sample will pull the remaining part of the flake onto the suspended region finalizing the transfer. The use of an out-of-plane tilt of the target substrate allows to identify a peel-off direction thus easing the transfer. For samples of more then 10 graphene layers and sufficiently large area i.e. 4-5 times the suspended area on clean Si/SiO$_2$ substrates, the success rate was increased to 100% in one shot transfers through this improvement.

We prepared two samples by testing different geometries which were measured in hydrostatic medium by using 4:1 Methanol:Ethanol PTM. The sample shown in Figure 4.12a, transferred and measured by Alexis Forestier, featured a large supported area almost completely surrounding the suspended region. AFM profile measurement, Figure 4.12b and Figure 4.12c show a thickness of 11.6 nm corresponding to a sample of $\sim$ 35 layers. I prepared a second loading where the sample was bridged across the trench. Figure 4.12d shows this sample after transfer on the

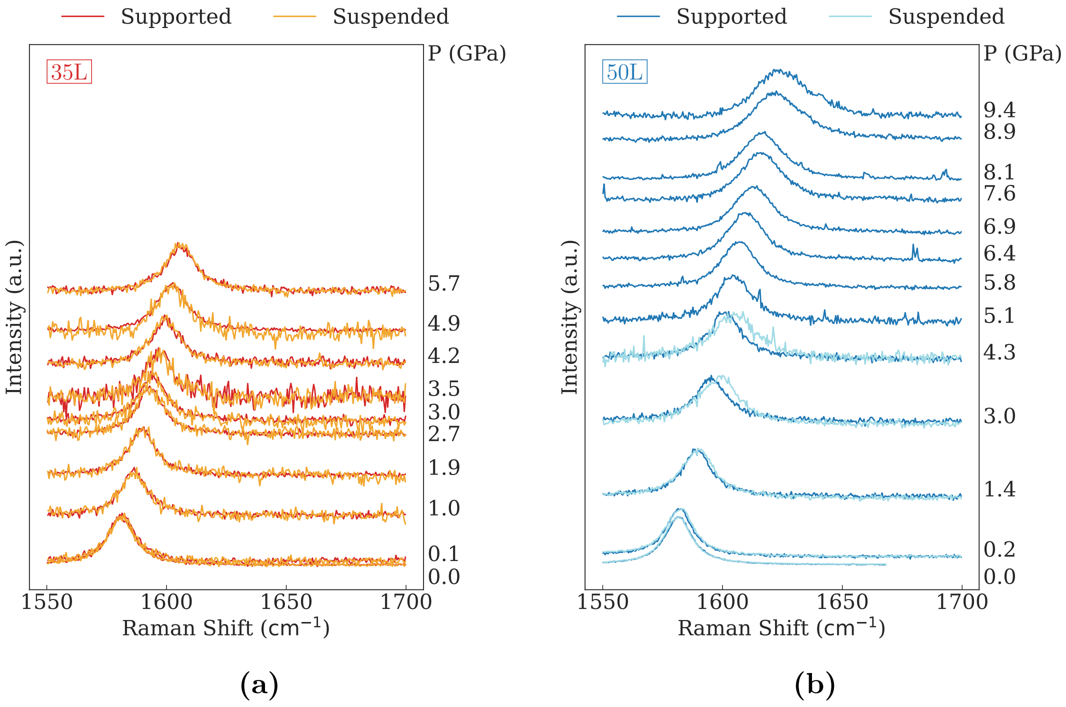

Figure 4.13: G-band spectra evolution for the experiments on the suspended FLG in 4:1 Methanol:Ethanol. The spectra are normalized to their maximum value and shifted proportionally to the pressure at which they have been acquired.

Si/SiO$_2$ substrate. Its thickness was slightly bigger than the previous one as shown by the AFM image and profile (Figure 4.12e and Figure 4.12f) measuring 17.5 nm (approximately 52 layers). To avoid confusion, we will label in Section 4.4.2 each experiment with the sample number of layers i.e. 35L for the first geometry and 52L for the second one. Finally, I prepared, with the help of post-doc Rajaji Vincent, a third sample of 7.2 nm in thickness ($\sim$ 21 layers) which we studied using pure water as PTM (Figure 4.12g). Due to the expected great importance of the sample-PTM interaction in this experiment we kept a large uncovered part of the trench to ensure a good access of the PTM in the trench. Precautions have been taken to have a big enough fraction of the flake suspended compared to the probing laser spot size. In our case the suspended region was around 18 µm^2. The results of our study on this sample will make object of Section 4.4.3

4.4.2 Suspended few layer graphene in 4:1 Methanol:Ethanol

We loaded the two samples shown in Figure 4.12a and Figure 4.12d in the DAC filling the compression chamber with 4:1 Methanol:Ethanol. We then used a 532 nm excitation wavelength laser to probe the sample response to high pressure using Raman spectroscopy. The G-band evolution with pressure is shown in Figure 4.13a and Figure 4.13b for the 35L and the 52L experiments. We can see a neat difference in the pressure evolution of the G-band in the two experiments. In the

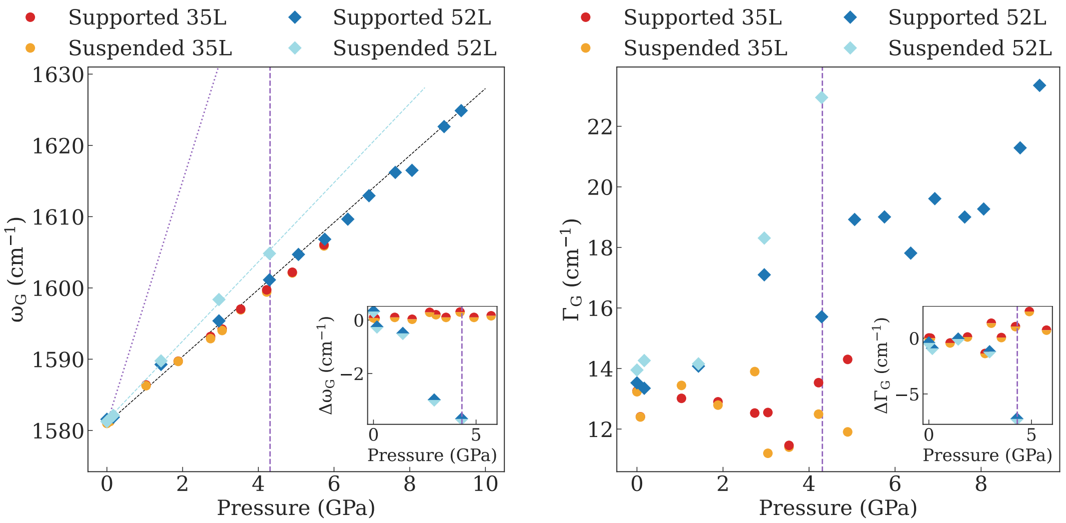

(a) **(b)**

Figure 4.14: Fitted G-band parameters for the spectra in Figure 4.13. Evolution of the frequency ω_G (a) and width Γ_G (b) of the G-band as a function of pressure. Two insets show the difference between the supported and suspended frequency $\Delta\omega_G$ and width $\Delta\Gamma_G$. The vertical purple dashed line indicate the pressure at which delamination of the SiO_2 layer of the substrate occurs. In (a) the black dashed line indicate the G-band shift in bulk graphite. The purple dotted line shows the calculated G-band shift expected by our model to explain the different evolution of the G-band in the suspended 52L sample. The light blue dashed line shows the linear fit of ω_G for the suspended 52L sample.

first experiment using the thinner 35 layers sample the two studied regions show a similar behaviour whilst a divergence at low pressure is present in the case of the 52 layers sample. To have a clearer view on the difference in behaviour between the two samples we plotted both the position and the width of the G-band peak as a function of pressure, fitted by Lorentzian peaks, which are shown in Figure 4.14a and Figure 4.14b respectively. In both experiments we observe the expected hardening of the G-band with pressure. This hardening is found to be compatible with that of bulk graphite for the supported regions showing a slope $\partial\omega_G/\partial P$ of 4.7 $\mathrm{cm^{-1}GPa^{-1}}$ [26]. The bulk graphite slope is described by the black dashed line in Figure 4.14a. A peculiar behaviour is however observed when we compare the evolution of the suspended regions in the two experiments. The experiment conducted on the 35 layers sample, where we adopted a three sides bridging geometry for suspended region, shows no clear differences between the suspended and supported G-band. Previous experiments showed that in hydrostatic conditions, FLG samples composed of more than two layers of graphene majorly slide on top of the silicon substrate due to their high bending stiffness that does not allow for conformation to the rough surface of the substrate[45]. On a microscopic scale the flake is thus essentially suspended not allowing for efficient strain transfer from the substrate to the sample. The experiment on the 52 layers sample, however, shows a striking high slope for the suspended region evolution for pressures below 4.3 GPa. Linearly fitting the points in this pressure region we obtain a slope $\partial\omega_G/\partial P$ of 5.56 ± 0.02 $\mathrm{cm^{-1}GPa^{-1}}$. For a clearer visualization of this effect we plotted the difference between the supported and suspended G-band frequency $\Delta\omega_G = \omega_G^{Supported} - \omega_G^{Suspended}$ in the inset in Figure 4.14a. From this plot it is clear the difference in behaviour for the two experiments with a constant flat evolution of $\Delta\omega_G$, close to zero, for the 35 layer sample and a monotone decrease for the 52 layer sample up to 4.2 GPa. Above this pressure the substrate completely delaminates as observed in the experiments in Section A and Section 4.3 for samples on $\mathrm{Si/SiO_2}$ at similar pressures. A vertical purple dashed line in Figure 4.14a and Figure 4.14b highlights this transition. Due to the poor *in-situ* imaging quality integrated with the Raman microscope used in the 52 layers sample experiment it was not possible to clearly distinguish the suspended region above this pressure. The FWHM of the G-band peak Γ_G shown in Figure 4.14b also shows small discrepancies between the two experiments. For the 35 layers the FWHM remains constant throughout the pressure range up to the maximum studied pressure. The difference between the supported and suspended region FWHM values $\Delta\Gamma_G = \Gamma_G^{Supported} - \Gamma_G^{Suspended}$ also do not show significative differences, in agreement with $\Delta\omega_G$. On the other hand, the width Γ_G of the 52 layer sample increases with pressure. A decrease of $\Delta\Gamma_G$ is also observed indicating a difference in the pressure response between the two regions.

This divergence from the graphitic behaviour observed in the suspended region of the 52 layers sample is counter-intuitive. For this part of the sample one would expect to remove the $\mathrm{Si/SiO_2}$ substrate potential additional strain thus obtaining the pure graphitic behaviour in hydrostatic conditions. Moreover, due to high number of layers on the sample, we excluded the connection of the observed behaviour to chemical interactions with the PTM as they would affect mainly few superficial layers whilst the majority of the contribution of the Raman spectrum would arise from the greater number of inner layers. In order to understand this phenomenon we need to consider the difference in geometry adopted in the two experiments. As we have already mentioned, in the experiment using the 35 layer sample we suspended the sample in such a way that three sides of the suspended region were in contact with the substrate (see Figure 4.12a). In this configuration the rigidity of the flake retains it flat onto the top surface as shown schematically in Figure 4.15a. When pressure is applied the hole shrinking does not largely affects the flake and its in-plane response is mainly dominated by the PTM compressing the sample side (Figure 4.15b). This hypothesis is backed-up by the observation that both the suspended and supported region behave similarly to graphite when compressed. On the other hand, the bridge geometry adopted for the 52 layers sample allows the flake to interact electrostatically or through Van der Waals forces with the trench walls. The sample is attracted by the walls and partially enters inside the trench as shown schematically in Figure 4.15c. The sample clamped by the trench is now compressed by the substrate shrinking when pressure is increased. A simple model can be made by assuming that the totality of the compression is transferred from the substrate to the suspended flake into uniaxial compression. The relative shrinking of the substrate volume $\Delta V/V_0$ is related to the bulk modulus of silicon B_S and the variation of pressure ΔP as:

$$\frac{\Delta V}{V_0} \equiv \left(\frac{\Delta L}{L}\right)^3 = -B_S\frac{\Delta P}{P} \tag{4.1}$$

where $\Delta L/L_0$ is the relative redaction of the cube side in one dimension. We can thus express the evolution of the G-band as a function of pressure $\omega_G(P)$ by relating it to the variations of the in-plane lattice parameter $a(P)$[26]:

$$\frac{\omega_G(P)}{\omega_G^0} = \left(\frac{a(P)}{a_0}\right)^{3\gamma} = \left(1 - \frac{\Delta a(P)}{a_0}\right)^{3\gamma} \tag{4.2}$$

with ω_G^0 and a_0 the ambient pressure G-band frequency and lattice parameter, γ the Grüneisen parameter of graphite and $\Delta a(P)$ is the variation of the lattice parameter with pressure relative to the ambient pressure one. We can note that the quantity $\Delta a(P)/a_0$ corresponds in Equation 4.1 to the uniaxial relative shrinking of the trench $\Delta L/L_0$ if the lattice parameter is aligned perpendicularly to the trench's wall. Combining Equation 4.1 and Equation 4.2 we can then obtain the expected G-band frequency in the case of equal reduction of the trench and sample dimensions:

$$\omega_G(P) = \left(1 - \left(\frac{P}{B_s}\right)^{\frac{1}{3}}\right)^{3\gamma}\omega_G^0 \tag{4.3}$$

This G-band evolution in this ideal case is shown in by the dotted purple line in Figure 4.14a. It is clear that this simplified vision of the substrate-sample interaction largely overestimates the strain transfer to the FLG. In our model we did not included the possibility of allowing out-of-plan stretching. As we are in hydrostatic conditions the sample can bend Figure 4.15d and ripple Figure 4.15e

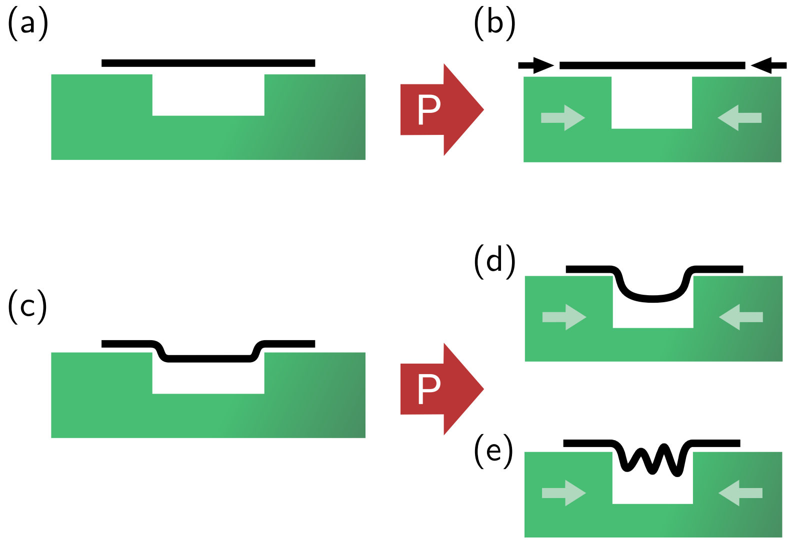

Figure 4.15: Schematic section view of the different geometries of suspended FLG in 4:1 Methanol:Ethanol. (a) When the sample is supported on three of its sides it lays flat on top of the trench. (b) Applying pressure the compression of the substrate is not transferred to the sample and we obtain a graphitic behaviour. (c) In the bridged configuration the sample partially enters the hole. When pressure is increased the substrate compression is transferred to the sample by the substrate walls. Part of the strain is loss into (d) bending and (e) rippling of the sample.

within the trench. Those two mechanisms will reduce the in-plane compression of the flake reducing the expected G-band frequency. Finally partial sliding outside the trench can contribute to lower the G-band slope.

In this section we demonstrated that even for samples composed of several graphene layers the suspended geometry can affect the sample response to high pressure. This was demonstrated by comparing different geometries in the same environmental configuration considering mostly mechanical effects. In the following we will change the PTM to pure water revealing the potential of the suspended geometry in a chemically interacting environment.

4.4.3 Graphene high pressure phase transition tuning via suspension: the water case

The sample in Figure 4.12g has been prepared to study the effect of water PTM on suspended samples. As we have seen in the previous section, suspending the sample across a central area of the trench might introduce additional stresses. We thus preferred to transfer our sample on one of the corner of the hole in order to simplify the data interpretation.

The evolution of the G-band spectrum with pressure is shown in Figure 4.16. We can note a remarkable difference between the sample in the suspended and supported regions which are shown by respectively red and pink solid lines. In particular a strong divergence both in the position and width of the peaks of the two regions is observed above 1.8 GPa. It is important to remind that a solid-solid

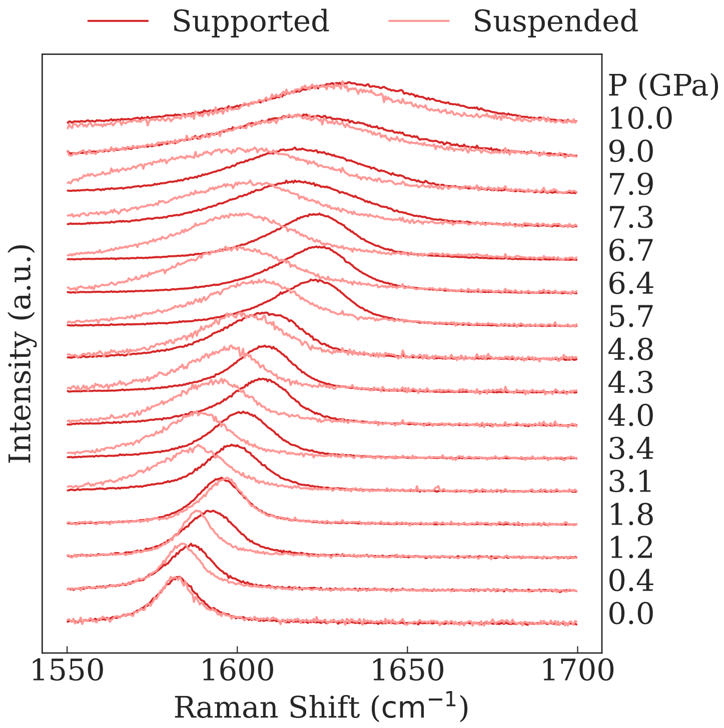

Figure 4.16: G-band spectra evolution with pressure in the experiment comparing suspended and supported FLG in water PTM.

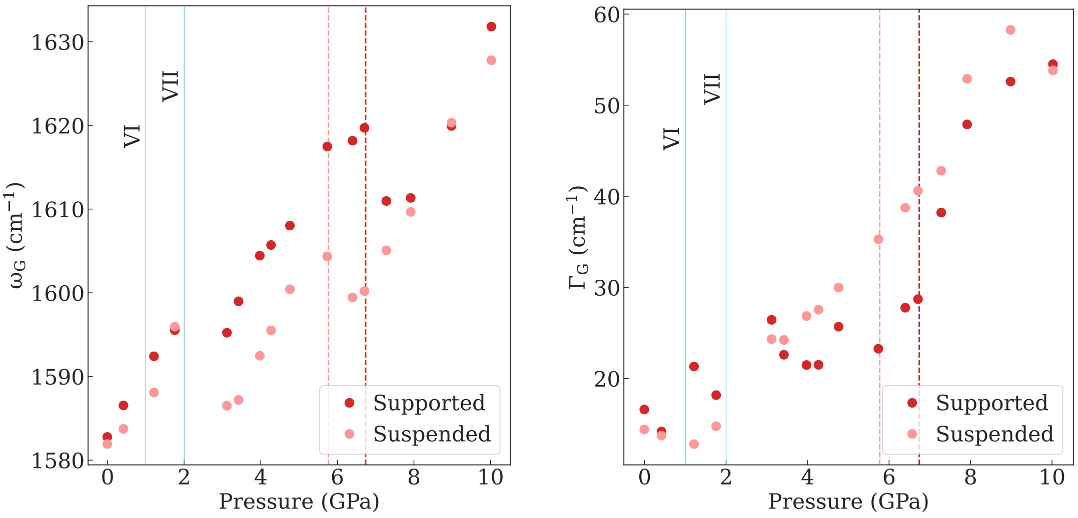

(a) **(b)**

Figure 4.17: Pressure evolution of the G-band frequency ω_G (a) and width Γ_G (b) as a function of pressure. The phase transitions of water to ice VI at 1 GPa and to ice VII at 2 GPa are highlighted by blue solid lines. Two dashed lines indicate the transition to diamondene for the suspended (pink) and supported (red) regions of the flake.

phase transition of the pressure transmitting medium from the ice-VI to the ice-VII phase occurs at 2 GPa. The Raman peaks have been fitted using Voigt functions to account for the Gaussian widening of the peaks due to the quasi-hydrostaticity of the PTM. The fitted peaks' centre and width are shown in Figure 4.17. The G-band frequency (Figure 4.17a) experience two clear discontinuities at intermediate pressures:

- around 2 GPa the G-band shows a sudden drop. After this transition the response in the suspended and supported region dissociate with a more pronounced red-shift of the G-band in the suspended region of the sample.
- A second drop in the G-band frequency is experienced between 5 and 8 GPa. The transition occurs at lower pressure (5.7 GPa) for the suspended part compared to the supported one (6.7 GPa). A pink and a red dashed lines highlight those two transitions in Figure 4.17.

The transition observed around 2 GPa is strictly connected to the ice VI to ice VII phase transition. When solidification of the PTM occurs the G-band features have shown to be highly sensitive to it in different PTMs[34, 36]. Additional strain and shear can be induced on the sample by non-hydrostatic forces. In the case of water the first solidification transition takes place at 1 GPa but visibly does not affect much the hydrostaticity. Large effects are observed in the case of the solid-solid transition at 2 GPa[36]. In addition to that, our sample experience a different response to the transition in the two studied regions. The G-band frequency, that up to 2 GPa shifted similarly in the two cases, experiences a larger drop in the case of the suspended part of the sample. This effect can be straightforwardly explained by considering the change in volume of ice at the phase transition. Just before the transition the sample covering the suspended area would be sitting on a slab of solid ice VI which filled the trench. When the transition to ice VII occurs, the ice experience a sudden reduction of volume of $\sim 9\%$[162]. Due to the solid nature of the medium the PTM can not readily fill the vacant space in the trench so the FLG is stretched by the covering PTM to accommodate this change. The tensile force induced by this stretch results in a redshift of the G-band frequency.

While the singular behaviour of this transition was well explained by the role of the phase transition of ice at 2 GPa, the ice-VII phase is stable at room temperature above this pressure up to 31 GPa[163]. Structural changes in the PTM can not justify the discontinuities found in the G-band frequency at 5.7 and 6.7 GPa. Several groups reported a transition around 7 GPa in bilayer graphene and few-layer graphene[23, 46] shown by both a drop in the G-band frequency and its rapid widening. Those evidences are well in agreement with the observed behaviour of our supported sample with the transition highlighted by the red dashed line in Figure 4.17a for the G-band position and in Figure 4.17b for its width. The transition was associated to a conversion of part of the sp^2 bonds of carbon into a sp^3 network mediated by the functionalization of the top graphene layer by the water molecules[23]. The authors of that work proposed a cascade effect that propagate the sp^3 bonds throughout the inner layers until total re-hybridization.

A similar behaviour is experienced by the frequency response of the suspended portion of the sample, however the transition is shifted to lower pressures by one

GPa as shown by the pink dashed line in Figure 4.17a. One possible explanation for this reduction of pressure is that, by having the PTM on each side of the sample, the functionalization occurs on both terminal surfaces of the flake thus helping the transition and propagation of the sp^3 bonds in the sample. Remarkably, there is no neat signature of this transition in Γ_G which increase linearly with pressure. Finally, we can observe that after the transition in the suspended region both ω_G and Γ_G of the two regions merge back at higher pressure. Overall, the hypothesis proposed by Pimenta et al.[23] of a propagation of the transition throughout the inner layers of the flake seems to be supported from our data.

4.4.4 Conclusions

In this section we studied the possibility of exploiting the suspended geometry at high pressure for studying thin graphite samples composed of several graphene layers. Going beyond superficial effects we demonstrated the advantage of this geometry in affecting bulk properties both mechanically and chemically.

Using 4:1 Methanol:Ethanol PTM we showed that without changing neither the sample surrounding environment nor its nature we can obtain different pressure responses on the suspended and supported regions based on the chosen suspended geometry. Those results allowed us to choose the most suitable geometry for conducting experiments using pure water as PTM. By using this PTM we experienced the presence of several discontinuities on the sample response due to both mechanical and chemical interactions. In particular, we observed the previously reported water mediated transition to a 2D sp^3 rich phase. However, we demonstrated that by suspending the FLG using our drilled substrates it is possible to lower the transition pressure by at least 1 GPa showing the potential of using those substrates on FLG samples.

Several questions remain, however, unsolved on the mechanism that is involved in this water mediated transition at high pressure to a diamond like 2D material. Consequently, we further investigated the environmental effects due to the use of water as PTM in order to rule out the underlying mechanisms that are involved. The following section will thus be fully dedicated to the study of multilayer stacking of graphene using water as PTM.

4.5 Novel insights in the characterization of the phase transition to diamondene at high pressure in water medium

In our quest of understanding the role of the substrate and PTM in the pressure response of carbon based two-dimensional materials great interest was drawn by the possibility of tailoring the environment in order to induce phase transitions. More precisely, the two-dimensional sp^3 rich carbon phase, often referred as diamondene in the literature, drew great attention in the nanomaterials community for its predicted properties such as diamond like hardness[164], a direct dielectric band gap[165], and ferromagnetism[166]. In order to stabilize this phase it has been shown that a high degree of functionalization of the surface layers is necessary. In fact, recent studies showed that at ambient pressure and temperature chemical functionalization and sp^2 to sp^3 conversion was induced by using hydrogen and hydroxyl groups as well as fluorination[167, 168]. From those experiments it is evident that the environment surrounding the sample plays a fundamental role in this phase transition. Furthermore, Pimenta et al. showed that it is possible to produce diamondene by applying high pressure on two and few-layer graphene samples[23]. They showed that the use of water as PTM favoured the formation of sp^3 bonds between the layers of graphene at pressures as low as 7 GPa. When mineral oil PTM was used they did not observe the transition, highlighting the role of the chemical nature of the PTM in the induced phase transition of those graphene stacking materials. They performed DFT calculations to support their experimental results. They showed that by imposing the functionalization of the top layer using hydrogen and hydroxyl groups an sp^3 network established, connecting the carbon atoms, propagating from the top layer to inner ones. The obtained structure was found to be stable at room temperature above 4.9 GPa. However, those calculations where performed at 0 K on a small number of atoms of one and few-layer graphene stacking far from experimental conditions. Moreover, the artificial functionalization of the top layer may induce computational artefacts as a more realistic model would consider the gradual formation of nucleation sites across the surface.

A minimal number of studies were conducted following this line of thoughts showing evidences of water mediated diamondene formation at high pressure[46, 125]. Several uncertainties are, however, still present both in the experimental and theoretical evidences brought out from those works. In particular the necessity of water as a trigger for the top layer functionalization is still not clear. The role of substrate in the transition has also not been thoroughly explored leaving doubts on whether non-hydrostatic pressure plays a role in the transition. From the computational point of view a more realistic model would also need to include the contribution of finite temperature that may contribute to weaken metastable phases issued by computational local minima.

In our experiments we tackled those question both from an experimental and theoretical point of view. We performed Raman measurements at high pressure of few-layer graphene deposited on Si/SiO_2 using pure water as a PTM. Experimentally, we studied the water contribution in the functionalization of the top surface by transferring two separate samples on the Si/SiO_2 substrate. One of the samples was covered by a thin layer of hexagonal boron nitride (hBN) and showed no signature of the phase transition which, on the other hand, was present in the uncovered sample. We also studied the incidence of the substrate nature by measuring thin flakes deposited on bare diamond. In this case, on both covered and uncovered samples, we did not observe the diamondene phase transition in the 6-8 GPa range, evidencing the role of the substrate in inducing the transition. The experimental results have then been backed up by molecular dynamics (MD) studies which showed that the formation of sp^3 nucleation sites are favoured by the additional biaxial strain present when Si/SiO_2 substrates are used.

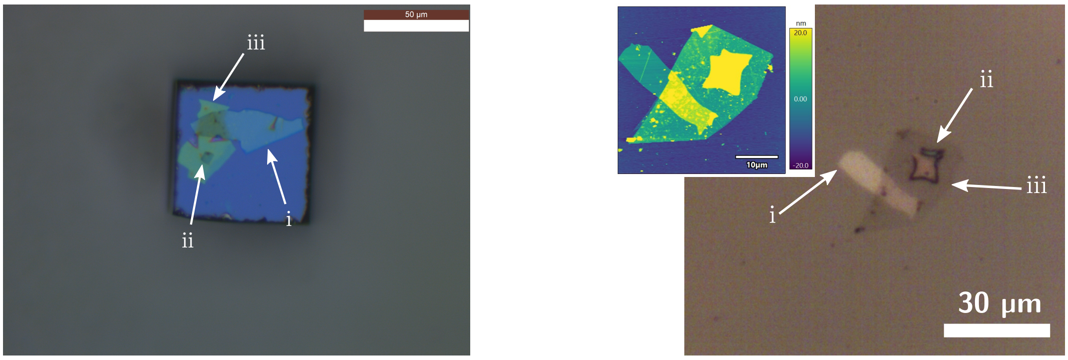

(a) Si/SiO$_2$ substrate **(b)** Diamond substrate

Figure 4.18: Optical images of the samples used in the diamondene experiments. In both figures (i) shows the free uncovered few-layer graphene sample, (ii) the covered one and (iii) the hBN flake. In (b) on the top left an inset shows the AFM topography of the sample on diamond.

4.5.1 Sample preparation

The samples we studied were carefully prepared by subsequent transfers of the flakes either directly on diamond or on a bare Si/SiO$_2$ cube previously glued on the diamond. Direct exfoliation of graphite on a PDMS stamp was privileged in those experiments for the production of thin flakes. Once samples of the desired thickness were located, we transferred for each experiments two few-layer graphite samples by dry transfer PDMS stamping (see Section 2.4.1). One of the samples was then fully covered by an hBN flake which was exfoliated from bulk hBN synthesised by Camille Maestre of the Laboratoire des Multimatériaux et Interfaces (Lyon) and transferred using the same procedure. It is important to highlight that throughout the multistep transfer process of the sample extreme care was taken to avoid that an already transferred sample entered in contact with the following PDMS stamps, avoiding eventual damaging. This was easily achieved thanks to the improvements I developed in the transfer set-up described in Section 2.4.1 which allowed for control of the out-of-plane rotational angle and thus the direction of stamp contact. The samples we prepared are shown in Figure 4.18. The hBN and FLG on Si/SiO$_2$, shown in Figure 4.18a, are easily distinguishable by their difference in colour. When on top of the thin SiO$_2$ substrate they appear greenish and blue respectively. The number of layers of each flake has been estimated by optical contrast due to the lack of AFM measurements to be between 30 and 50 layers. Light interference is not present when the samples are directly transferred on diamond (Figure 4.18b). However, hBN is almost transparent allowing for the identification of each sample by optical contrast. The measurement of the sample height through the AFM measurement, in the inset in Figure 4.18b, showed that the uncovered FLG sample measured $\sim$ 13 nm ($\sim$ 40 layers), the covered one $\sim$ 110 nm ($\sim$ 329 layers) and the hBN flake $\sim$ 16 nm (48 layers). I conducted the experiment on Si/SiO$_2$ together with Dr. Rajaji Vincent who entirely performed the experiment on diamond.

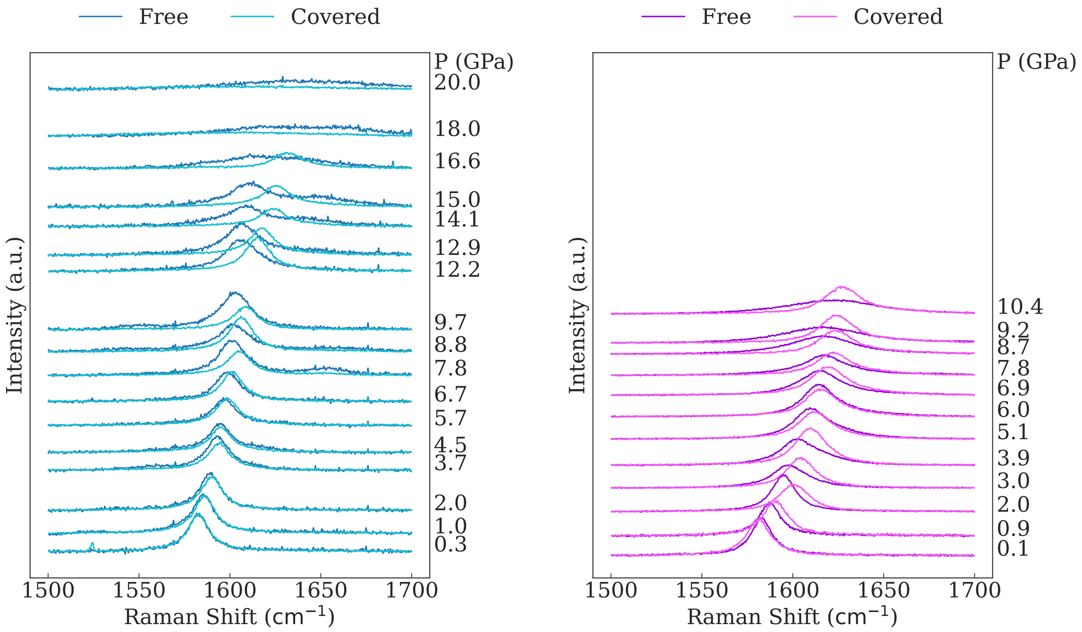

(a) Diamond substrate

(b) Si/SiO$_2$ substrate

Figure 4.19: G-band spectra evolution with pressure for the two experiments comparing the effects of FLG in contact with water (Free) or covered by an hBN flake (Covered). The same colour convention for the substrate and samples will be kept throughout this section during the analysis. The spectra are normalized to the lowest pressure point for each sample. A shift of the intensity proportional to the pressure at which the spectrum is acquired has been introduced to help the visualization.

4.5.2 High pressure Raman studies

Those two sets of samples have been submitted to high pressure using a Letoullec DAC featuring a 600 µm diameter cullet size. Due to limitations introduced by the Si/SiO$_2$ substrate thickness we used Rhenium gaskets instead of the traditional steel ones in the experiment where the substrate was present. We had observed in previous experiments that increasing pressure lead to the contact between the substrate top surface and the top diamond cullet at pressures as low as 5 GPa. Employing Rhenium gaskets we reached 12 GPa without contact with the anvil.

We measured the evolution of the Raman features of our samples in order to detect the signatures of the sp^2 to sp^3 transition. We used a Horiba LabRam Raman spectrometer equipped with a 532 nm wavelength laser for *in-situ* sample probing. We also performed wavelength dispersive measurements of the Raman spectrum using an Horiba Aramis for measurements at wavelengths of 473 nm and 633 nm.

The G-band spectra evolution with pressure measured at 532 nm is shown in Figure 4.19a for the experiment with the sample transferred directly on diamond and Figure 4.19b for the sample supported on the Si/SiO$_2$ substrate. In both

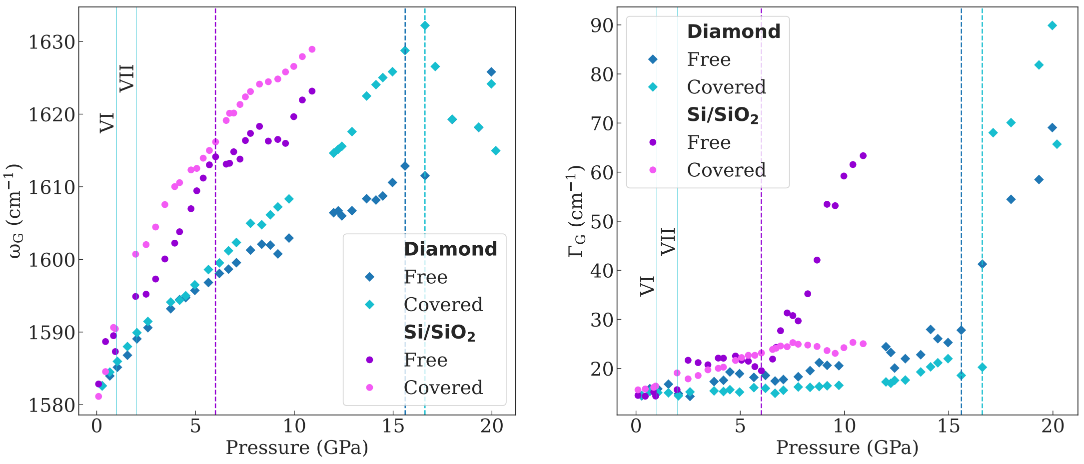

(a) **(b)**

Figure 4.20: G-band frequency ω_G (a) and width Γ_G (b) evolution as a function of pressure. The blue solid line highlight the transitions of water to ice VI at 1 GPa and to ice VII at 2 GPa. The purple dashed line indicated the pressure at which the diamondene formation occurs in the uncovered sample supported on Si/SiO$_2$. The dark and light blue dashed lines help the visualization of the pressure at which the transitions to sp^3 rich phases occur for the samples on diamond.

experiments a clear difference in the features' behaviour is observed between the hBN covered region and the free, uncovered one. An increasing blue shift of the G-band frequency is observed when compressing, augmenting at a higher rate for the covered region.

The fitted G-band frequency ω_G is displayed in Figure 4.20a. We observe a clear difference in the increasing rate between the two experiments with a stronger blue shift with pressure experienced by the sample on the Si/SiO$_2$ substrate. This observed feature originates from the much higher compressibility of the silicon compared to both graphite and diamond. The former introduces the additional biaxial strain that shifts the G-band to higher energy[45]. Moreover, a discontinuity in the slope of the G-band is observed in the experiment using the Si/SiO$_2$ substrate in occurrence of the ice VI to ice VII phase transition of the PTM. This transition is not as marked when the sample was directly supported by the diamond.

A second discontinuity is observed in the evolution of ω_G at 6 GPa (purple dashed line in Figure 4.20a) in the uncovered part of the sample supported on Si/SiO$_2$. Similarly to our experiments in water PTM of Section 4.4.3 as well as to the result proposed by Pimenta Martins et al.[23] this transition is identified as the passage from the sp^2 phase of graphene to the sp^3 rich phase referred as diamondene. To further confirm this hypothesis we can turn to the analysis of the evolution of the G-band width in Figure 4.20b. At 6 GPa the width, which remained constant after the phase transition to ice-VII at 2 GPa, steeply increases. The abrupt widening of the G-band has been reported as a clear indication of a partial transformation of the sp^2 carbon bonds into sp^3 bonds[26, 169]. The presence of a weak G-band indicated that not the totality of the sp^2 bonds have changed their hybridization. Remarkably, we did not report any discontinuities at similar pressures of ω_G and Γ_G for the simple covered by hBN on Si/SiO_2 nor for either sample directly deposited on the diamond.

For what concerned the graphene/hBN heterostructure on the Si/SiO_2 substrate, the construction of such a sample geometry was developed to investigate the fundamental role of water in the pressure induced diamondene formation. Isolating graphene from the water PTM by means of the hBN flake, we aimed to prevent the functionalization of graphene by the ice molecules thus forbidding the diamondene formation. The experimental results we just described are in complete agreement with our initial hypothesis showing the potential of building heterostructure to affect environmental effects even on samples composed of several layer of graphene.

An *a priori* unexpected result concerned the experiment conducted with the sample directly transferred on the diamond. While none of the previous works reported any substrate dependency in the water mediated diamondene phase transition[23, 126], we did not observed any spectral signatures associated with it within the expected 6-8 GPa range. The G-band frequency steadily increases up to $\sim$ 15 GPa with a slightly higher slope for the covered sample. The width Γ_G also does not show any major variations up until $\sim$ 15.6 GPa for the uncovered sample and $\sim$ 16.6 GPa for the hBN covered one. Above those pressures a rapid increase of Γ_G is observed. We can observe in Figure 4.19a that at 20 GPa the G-band is very wide and weak and it has almost completely disappeared in the case of the covered sample. The pressure at which this transition occurs is compatible with the previously reported values of 10-18 GPa for the transition to a diamond-like phase in cold compressed graphite[26, 169, 170, 171]. Those results make us conclude that water and its ice phase in contact with few layer graphene are not sufficient to induce the diamondene formation we observed in the sample deposited on Si/SiO_2.

To further confirm our observation we performed wavelength dispersive Raman measurements on our samples at 633 and 473 nm excitation wavelength. Being a first order Raman scattering process at the origin of the G-band, intrinsically suggests that it should not disperse when varying the excitation energy. However, Ferrari et al. reported a frequency increase with increasing excitation energy when graphite presents a part of the carbons hybridized sp^3[71]. This argument had also been employed by Pimenta Martins et al. to prove the water assisted formation of diamondene in bilayer samples[126].

Due to the length of such a measurement in the DAC only a few dispersion measurements have been performed on our samples. The measured spectra are shown in Figure 4.21a. The fitted G-band position is shown in Figure 4.21b as a function of the exciting wavelength. We note that for the diamond experiment no dispersion is observed for the two measured samples. In the experiment on Si/SiO_2 we observe a small variation of the frequency with the wavelength for the covered sample on Si/SiO_2 at 5.1 GPa and a larger one for the uncovered one at 8.7 GPa. In order to verify the accuracy of those measurements we estimated the uncertainties on the frequency by linearly summing the fitting error and an experimental error

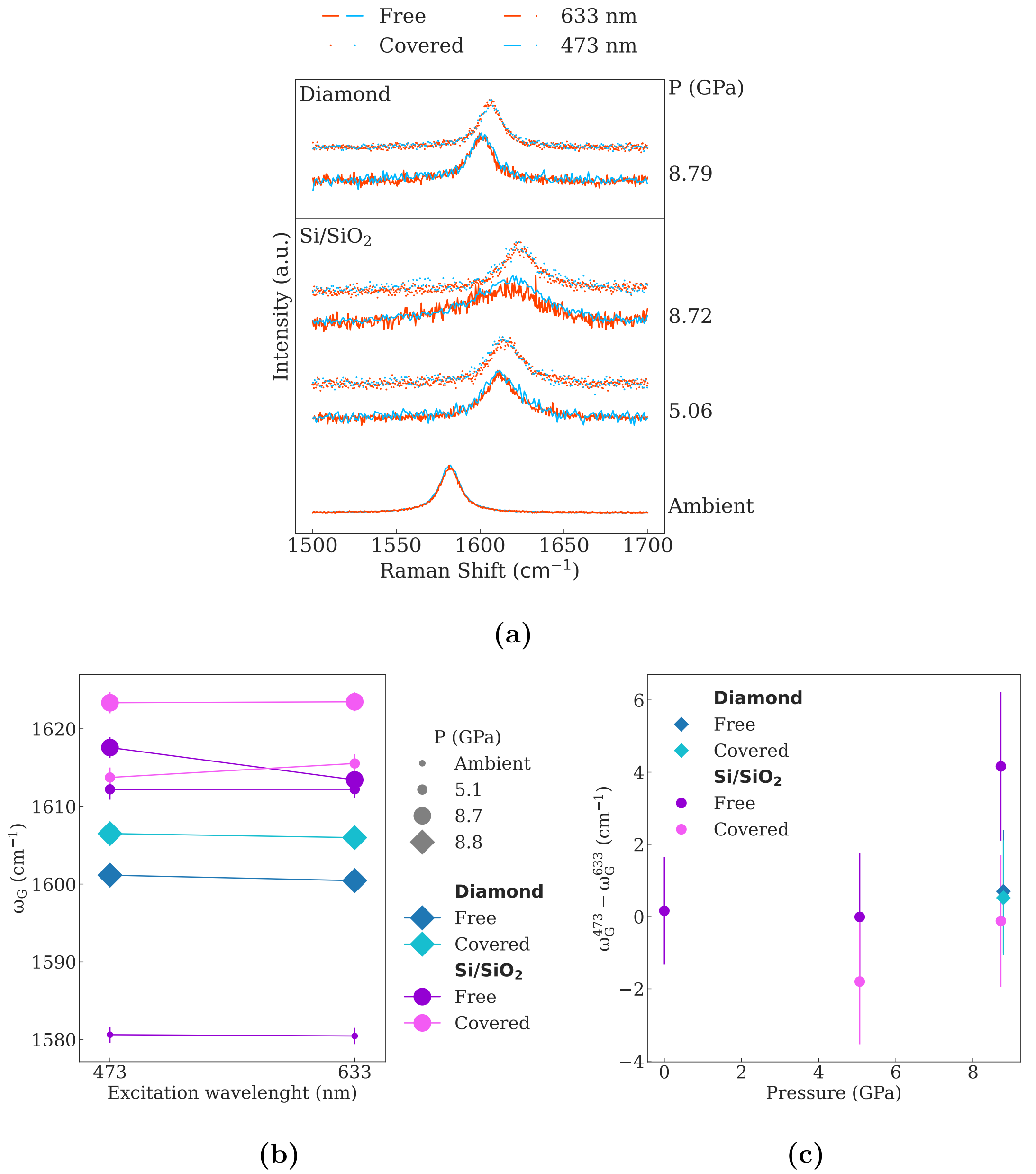

(a)

(b)

(c)

Figure 4.21: Summary of the wavelength dispersive measurements performed on our samples. (a) shows the normalized background subtracted spectra in the G-band region. The fitted G-band position is plotted in (b) as a function of the excitation wavelength. Markers of different size have been used to indicate the pressure at which each spectrum has been acquired. The frequency shift $\omega_G^{473} - \omega_G^{633}$ is plotted showing dispersion only for the uncovered sample on Si/SiO$_2$ at 8.7 GPa (c).

of 1 cm^{-1} which includes the instrumental contribution to the uncertainties[172]. We also plotted the difference between the frequency of the G-band measured at 473 nm ω_G^{473} and that at 633 nm ω_G^{633} which is plotted in Figure 4.21c as a function of pressure (the uncertainties are here summed quadratically to account for the independence of the measurements[172]). Between all the measurements only the uncovered sample on Si/SiO$_2$ at 8.7 GPa is found to be different from zero within the experimental error. Those measurements are in agreement with our conclusions that only the uncovered sample on the Si/SiO$_2$ presents the signatures of a diamond like phase at 8.7-8.8 GPa. For what concerns the covered sample on the silicon substrate at 5.1 GPa we measured a value of $\omega_G^{473} - \omega_G^{633} = -1.8 \pm 1.8$ cm^{-1} making it consistent with zero only at the limit of the uncertainty. The value of the higher pressure point as well as the fact that for an sp^3 rich phase of graphite would result in a positive value of $\omega_G^{473} - \omega_G^{633}$ makes us safely state that this value is also consisted with zero within the experimental uncertainties.

The spectroscopic signatures we gathered during our experiments indicate that we can prevent the formation of sp^3 bonds in few layer graphene by covering it with an hBN flake as well as by using diamond as a substrate for our sample. While the first method has been traced back to the isolation of the flake from the water environment, a straightforward conclusion on the role of diamond is not clear. In the next section we will describe the underlying mechanism ruling this phenomenon which we backed up by computational results using molecular dynamics.

4.5.3 Biaxial strain induced diamondene. Discussion and theoretical calculations

From our experimental observation it results that two factors play an important role in the formation of the diamondene phase transition at pressure values between 6 and 8 GPa. The presence of water and of a suitable substrate. Water has shown to be a necessary ingredient in the transition as we did not observe any transition when water molecules where not in contact with graphene. This result might indicate that the mechanism proposed of the functionalization of the surface layer of the few-layer graphene sample by water's hydroxyl and hydrogen groups is indeed accurate. This model, however, does not appear to be compatible with the experiment conducted using diamond as a substrate. Indeed, it predicts that the simple presence of water on the surface and pressure would trigger the transition.

In order to explain the observed behaviour we need to take into consideration the additional biaxial strain induced by the Si/SiO$_2$ substrate on the sample. In Figure 4.20a we have already remarked that when the sample is supported by this substrate the G-band frequency increases at a higher rate compared to its corresponding on diamond. Moreover, from our data it results that, when the diamondene transition at 6 GPa on Si/SiO$_2$ occurs, the FLG G-band frequency is comparable with that of the uncovered sample on diamond at the transition at 15.6 GPa. In practice, if we consider that the pressure induce strain is the main contributor to the shift of ω_G, we find that the in-plane lattice parameters at the two transitions have similar values. From this observation we can conclude that,

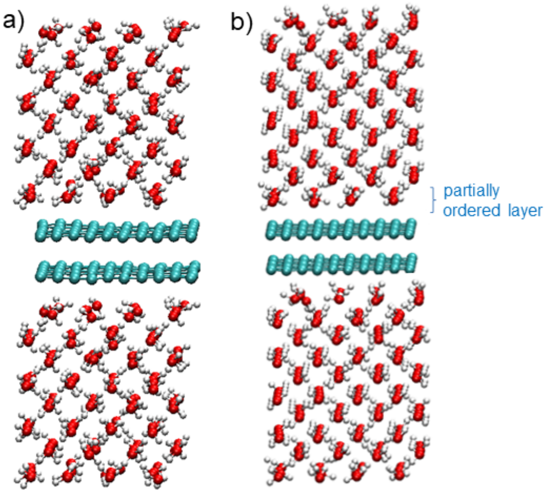

Figure 4.22: Initial cell for the molecular dynamic simulations. In green are schematized the carbon atoms of the bilayer graphene. In red and white the oxygen and hydrogen of water molecules. In (a) the water molecules, in ice-VII configuration, are proton disordered while in (b) we find a proton ordered ice layer in contact with the surfaces of graphene.

as well the presence of water in contact of the FLG, biaxial strain also plays a major role in governing the transition to an sp^3 rich phase.

Theory

To support our experimental observations with theoretical calculations our collaborators Mohammad Hellani, Flavio Sirio Brigiano and Fabio Pietrucci of the University of Sorbonne in Paris performed molecular dynamics (MD) calculation on a bilayer graphene sample surrounded by water molecules in the ice-VII phase. Previous computational methods performed in similar system were based on DFT calculations at 0 K. The totality of the sample surface of a small periodically repeated cell was initially factionalized by -H and -OH groups[166, 173, 174, 23]. In such conditions the conversion of sp^2 bonds into sp^3 was observed and the bilayer diamond-like structure obtained was found to be stable above 4.9 GPa[23]. Such conditions are, however, distant from the conditions found in experiments. More realistic large models which include temperature effects should be computed using MD.

The simulations of out team were performed on a bilayer graphene sample composed of 120 atoms in an initial AB stacking configuration. At the interfaces 128 water molecules were disposed forming ice-VII along a (001) facet (generated using the GenIce software[175]). The initial cell parameters were calculated by imposing static out-of-plane pressure $P_{zz} = 6.82$ GPa and in-plane ambient pressure $P_{yy} = P_{xx} = 100$ kPa resulting in a cell with dimensions $12.48 \times 12.91 \times 19.65$. Further simulations were performed at constant volume. The obtained cell is shown in Figure 4.22a. The stability of the functionalization of the graphene surface by epoxy, hydroxyl and hydrogen groups was tested by artificially bonding the

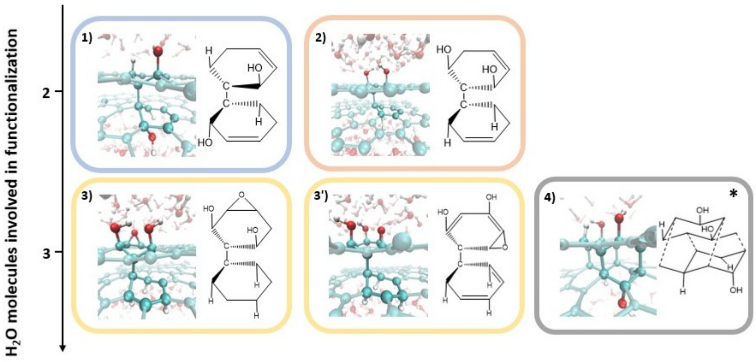

Figure 4.23: Schematic representation of the stable structures studied by molecular dynamics.

Table 4.1: Calculated potential energy and enthalpy values obtained for each structure.

Structures		1	2	3	4
Potential Energies (kcal/mol)	without in-plane pressure	145±20	162±20	324±20	187±18
	with in-plane pressure	147±18	183±17	344±17	198±19
Enthalpy (kcal/mol)	without in-plane pressure	333±160	376±150	669±150	332±160
	with in-plane pressure	321±180	299±170	437±160	139±170

molecules to the carbon atoms and conducting Bohm-Oppenheiler molecular dynamics (BOMD) simulations. All the explored configuration with such a system resulted in the cleavage of the bond between the carbon atom and the functionalization molecule which recombined into water after few tens of femtoseconds.

The crystalline structure of ice-VII is a proton disordered phase, however, experimental evidences shows that proton ordering is found in nano-sized domains[176, 177]. With that in mind a second model was built featuring a proton ordered ice-VII layer at the graphene interface. The resulting structure is shown in Figure 4.22(b). In this configuration several initial structures were generated by functionalizing individual carbon sites and creating sp^3 interlayer carbon-carbon bonds. Furthermore, in order to explore the effect of biaxial strain on the stability of sp^3 bonds those two systems have been explored by applying in-plane pressure of 6.8 GPa as well as 15 GPa. Figure 4.23 shows the structures that featured sp^3 hybridized carbon bonds and that have found to be stable within several picoseconds of MD simulation. The potential energy (PE) and enthalpy were calculated for those structures and the results are shown in Table 4.1. The values are displayed with respect to the pristine BLG configuration.

In structures 1 and 2 two water molecules have been split and functionalized the top and bottom layers. The former featured an -OH and -H functionalization of both layers while in the latter the two -OH were disposed on the carbon atoms of one layer and the two -H on the opposite one. Both the stable structures show similar values of PE and enthalpy with weak effects introduced by the additional in-plane pressure. Several other configurations can be achieved by splitting an additional water molecule. Stable configurations were formed by placing -OH groups on the same BLG layer at second-neighbour distance. After some simulation time, one of the hydroxyl group lost one of the hydrogen converting into an epoxy group. This resulted in structure 3 when no in-plane pressure was applied and $3'$ otherwise. A decrease in the enthalpy as well as an increase in the potential energy is observed when in-plane pressure is applied. We remark that those structures are highly energetic when compared to the other ones. The presence of the epoxy group might induce this increase by leading to a less stable structure. Finally, by placing two -OH groups on one side (on nearest-neighbour carbons) and one on the other we obtain structure 4. The position of the individual -OH had to be placed on a specific site in order to lead to a stable structure, more favourable in terms of interactions with the ice layer. This structure retained all the initial -OH and -H groups and formed three interlayer carbon-carbon bonds. Moreover, an additional carbon-carbon bond spontaneously formed after 1.8 ps of MD simulation. All the interlayer sp^3 bonds formed on sites adjacent to functionalized carbons, underlying the importance of the presence of water in the stabilization of the sp^3 bonds. Remarkably, the presence of in-plane pressure leads to a decrease in the average enthalpy and an increase of the potential energy. The presence of the four C-C interlayer bond results in a decrease in the overall pressure, so a decrease in the enthalpy and increase in stability of the structure.

To summarize, through molecular dynamics simulations at 300 K the explored structures revealed the stability of interlayer bonds favoured by water functionalization of individual carbon sites. Moreover, we observed that increasing the number of sp^3 sites from two (structure 1 and 2 in Figure 4.23) to four (structure 4 in Figure 4.23) leads to an increase of the overall potential energy and a decrease of the enthalpy indicating that the stability of the system is improved. Remarkably, this effect is enhanced by the introduction of biaxial strain which ulteriorly reduces the enthalpy and increase the potential energy. Overall, the calculations suggest that those sites might operate as nucleation sites for the formation of a long-range network of sp^3 interlayer bonds. We can expect that, increasing the number of sp^3 sites, we achieve a threshold critical size that favours the formation of diamondene.

4.5.4 Conclusions

In this work we presented novel methods to enrich our understanding of the water mediated high pressure diamondene phase transition in few-layer graphene samples. By creating a heterostructure composed of few-layer graphene covered by a flake of hexagonal Boron Nitride beside an uncovered few-layer graphene sample on a Si/SiO_2 substrate, we ruled out the role of water in the transition. In our experiment we observed clear spectroscopic signatures of the transition on the uncovered sample showed by a drop in the G-band frequency, a rapid increase of its width and a wavelength dispersive character of this mode above 6 GPa. On the other hand, we did not observe discontinuities on the hBN covered sample features in the pressure studied range. In this case the G-band was found to not be dispersive when changing the excitation wavelength up to 8.7 GPa. Those observations allowed us to conclude that water plays a fundamental role in the diamondene phase formation at 6 GPa by triggering the functionalization of the superficial graphene layer of the stacking.

Furthermore, in a second experiment we investigated the role of the substrate as a mediator for the sp^2 to sp^3 transition by transferring an equivalent pair of samples to that of the first experiment directly on the diamond anvil. Strikingly, in such a configuration we did not observe any spectroscopic signatures of the phase transition in the expected 6 to 8 GPa pressure range. The transition to a sp^3 rich phase occurred at ~ 15.6 and ~ 16.6 GPa for the uncovered and covered samples respectively. Those pressures are comparable to the values obtain for the transitions to a sp^3-bonded phases (M-carbon or Z-carbon) in graphite using different PTMs[26, 169, 170, 171]. From the observation that the shift of the G-band frequency of the sample on Si/SiO_2 denotes higher in-plane pressure than that experienced by the sample on diamond, we can concluded that the additional biaxial strain induced by the silicon substrate is essential for the formation of diamondene at low pressure.

To consolidate our conclusion our collaborators performed molecular dynamics computation on a similar system formed by a bilayer sample surrounded by water molecules in an ice-VII solid phase under pressure. Differently to previous calculations in the literature on systems resembling our one, they studied a model closer to the experimental conditions. They introduced the effects of temperature by performing our calculations at 300 K. Moreover, instead of departing from a fully water functionalized surface they gradually incremented the number of sp^3 sites simulating the growth of nucleation sites. Finally, they explored the effects of biaxial strain on the sample by applying on the same system hydrostatic pressure at 6.8 GPa as well as a in-plane biaxial pressure of 15 GPa when the out-of-plane pressure was 6.8 GPa. The calculations show that, despite the structure of ice-VII is proton disordered, a local proton order at the graphene water interface is necessary to stabilize the functionalized sites. Furthermore, we found several stable structures that featured sp^3 bonds after several picoseconds of molecular dynamics simulation. Additionally, we observed the spontaneous formation of a supplementary interlayer sp^3 bond after some simulation time in one of the structure. Energetically, the increase of the number of sp^3 interlayer bonds from one to four resulted in a decrease of the enthalpy and an increase of the potential energy indicating that an enlarging nucleation region might favour the transition to the diamondene structure. Finally, the introduction of the in-plane biaxial strain component resulted in energetically favourable structures with an augmentation of the potential energy and the decrease of the enthalpy in agreement with our experimental observations.

To conclude, the outcome of our experiments revealed that in addition to the presence of water as pressure transmitting medium, additional biaxial pressure on the sample is necessary to induce the diamondene phase transition in the pressure range of 6-8 GPa. In the quest of stabilizing and reducing the transition pressure of the diamondene phase of carbon, our results introduce a novel tuning parameter in the form of in-plane biaxial strain. Our observation, opens up the opportunity to extend the concept beyond diamondene to other two-dimensional materials, potentially revolutioning the accessibility of the domains of pressure induced phase transitions.

Chapter 5

Conclusions

The present work was devoted to the investigation of the pressure response of carbon-based low-dimensional systems and how their properties can be tuned using pressure when surrounded by different environments. We performed experiments on carbon nanotubes, graphene and few-layer graphene which we submitted to high pressure using diamond and sapphire anvil cells. The main probe of our samples was resonant Raman spectroscopy which gives us access to *in-situ* characterization of their vibrational and electronic properties in high pressure experiment.

In Chapter 2 we described the major instrumental developments carried on during my PhD. To increase the maximal pressure limitations of sapphire anvil cells (see Section 2.3) we performed measurements for the characterization of sapphire anvils which led to the selection of the most suitable anvils for our experiments. Moreover, we diminished the anvil stresses by reducing the indentation pressure and using soft grade steel gaskets. After those two adjustments we managed to top 4.2 GPa *in-situ* pressure without anvil failure (1.2 GPa higher than the pressure which previously led to anvil breakage). The use of those anvils allowed to obtain the experimental results on carbon nanotubes of Chapter 3 by opening the Raman D-band spectral window otherwise masked by the diamond signal. Our prospective is to extend their use to the characterization of defects formed in carbon based low-dimensional systems at high pressure and to detect the creation of sp^3 interlayer bonds in graphene and few-layer graphene at high pressure.

Another major development concerned the integration of a mapping system to our custom Raman spectrometer (see Section 2.4.2). The communication between the spectrometer, cameras and motor stages, all interfaced with LabView, led to the systematic location of the individualized carbon nanotubes studied in Section 3.4, the comparison of spectral mapping of the suspended and supported bilayer samples of Section 4.3 at ambient pressure and at 0.6 GPa, and perform several other characterizations not included in this thesis. The perspective is to extend its application to an entire pressure run to identify the evolution of local features such as spatial inhomogeneities due to non-hydrostatic PTMs or heterogeneous samples, as well as the detection of nucleation sites and domains in high pressure phase transitions.

In Chapter 3 we showed how, through the use of the Raman D-band, we could follow the signature of the collapse of single walled carbon nanotubes. Those results were possible thanks to the employment of a sapphire anvil cell which proved to be and excellent replacement for diamond anvils cells when studying carbon based materials. Our results on bundle samples show the gradual collapse of the tubes with increasing pressure, highlighted by a good agreement between the increase of the ratio of the intensity of the D and G bands A_D/A_G , and the decrease of the RBMs intensity. Upon pressure release we observed the tubes returning to their original circular cross-section geometry with an observed hysteresis behaviour. The comparison between experiments in 4:1 Methanol:Ethanol and nitrogen pressure transmitting media did not show substantial differences indicating that the collapse is independent on the nature of the PTM for the studied media.

In addition to bundle samples, we successfully performed experiments on individualized SWCNT at high pressure. Using those samples we could follow the collapse of an individual chirality tube through the use of A_D/A_G . This parameter showed a sigmoid-like increase during compression. We could identify three regions: at low pressure the tube is in its circular geometry; an intermediate phase showing a rapid increase of A_D/A_G which we assigned to the tube starting to ovalizing; at higher pressure A_D/A_G becomes almost constant identifying the completion of the collapse. The use of those samples, combined with the signature of the D-band at the collapse, opens up opportunities for chirality dependent studies of the collapse of carbon nanotubes as well as allows for the study of environmental and substrate effect as tuning parameters for the transition. Furthermore, by matching the experimental evolution of the D-band with theoretical calculation it would be possible to well characterize the intermediate oval geometries opening up opportunities for the fabrication of pressure assisted tunable devices and switches as well as nanometric pressure probes. Finally, those techniques could be extended to more exotic systems obtained by intercalating atoms and molecules in the nanotubes[27, 28, 29, 178]. They could be used to optimize aspects such as the collapse pressure, intermediate states, collapse reversibility and tune the associated physical properties.

In Chapter 4 we concentrated in getting a deeper understanding of the interaction between the environment and graphene. We performed a series of experiments where we carefully combined different substrates and pressure transmitting media in order to discriminate their contribution in the pressure response of graphene at high pressure. Our initial approach was to construct Si/SiO_2 substrates that would allow for suspension of graphene and would be compatible with the diamond anvil cell. We performed experiments using those substrates with samples of CVD grown bilayer graphene and mechanically exfoliated few-layer graphene. Using the bilayer samples (Section 4.3) we performed a Raman cartography of the sample before the 4:1 Methanol:Ethanol PTM loading and at 0.6 GPa and exploited the high statistic outcome of the mapping to show that the main feature affected by the suspension is the G-band frequency. This is to our knowledge the first reported case of both a bilayer graphene sample suspended and a spatially resolved Raman cartography at high pressure. By using the procedure firstly proposed by Lee et al.[69] we disentangle the strain and doping contributions principally due to the substrate and the PTM respectively. Our results show a high efficiency in the strain transfer from the suspended and the supported region of the sample by showing comparable strain values throughout the pressure run. For what concerns doping we found a quick increase of the charge density topping around 2 GPa $\sim 2.4 \cdot 10^{12}$ cm^{-2} for the hole doping scenario and $\sim 1.4 \cdot 10^{12}$ cm^{-2} for electron doping. Comparable values are found in the two regions, with a slightly higher doping level in the suspended part at low pressure. Those results motivate the possibility of novel approaches for the study of those samples. In particular, a detailed characterization through Raman mapping in the low pressure regime may reveal the presence of doping gradients which could open up opportunities for the construction of pressure tunable devices for energy harvesting[179] and electronics[180, 181].

Using the few-layer graphene samples (see Section 4.4) we performed experiments both in 4:1 Methanol:Ethanol and water PTMs. When water was used as PTM we observed major differences in the pressure response in the suspended and supported region. A strong redshift of the G-band position is observed in the suspended region compared to the supported one when the ice VI to ice VII phase transition of the PTM occurs. Moreover, we observed a reduction of the transition pressure of the phase transition from nanographite to diamondene i.e. from sp^2 to sp^3 atomic bonds, of ~ 1 GPa in the suspended region. We attributed this phenomenon to the chemical interaction of the PTM on both sides of the few-layer graphene sample, showing the interest of those suspending structures for enhancing the chemical interaction between the PTM and the sample.

Those results obtained in water PTM motivated us to find new pathways to tune the transition pressure of the water assisted formation of diamondene from few-layer graphene. In Section 4.5 we interrogated the role of water in the transition by creating an heterostructure of few-layer graphene covered by hBN beside an uncovered few-layer graphene, both supported on a Si/SiO$_2$ substrate. Up to 10.4 GPa we did not observe any spectroscopic signatures of diamondene formation in the heterostructure. On the other hand, the transition was observed around 6 GPa for the uncovered sample indicating that the interaction with water is fundamental to trigger the transition. Additionally, we performed an experiment with few-layer graphene both uncovered and covered with hBN directly on diamond using water PTM. The two samples show the evidence of formation of a sp^3 phase only at 15.6 and 16.6 GPa. Those pressure are compatible with the formation of sp^3 bonds in cold compressed bulk graphite[26, 169, 170, 171]. Those experiments showed that whilst water is necessary to induce the transition to diamondene at low pressure its presence is not sufficient to trigger it. We concluded that, the biaxial strain transferred from the substrate to the sample needs to be taken into account. Molecular dynamic simulations performed by our collaborators on a similar system are in agreement with the experimental results, showing that biaxial strain may favour the stability of interlayer sp^3 bonds.

Those results on two-dimensional systems are highly promising for possible application. Our results on the characterization of the transition to diamondene showed that biaxial strain can be explored as a novel unique tuning parameter for phase transitions. In particular we could enhanced those transitions by combining highly compressive substrates and the suspended geometry. This approach could ulteriorly reduce the transition pressure and stabilize the diamondene phase at ambient conditions. The same concepts could be extended to other phase transition at high pressure in 2D systems as for the formation of the hBN sp^3 phase [182, 183], the metallization of MoS_2[184] and interlayer bonding formation in heterostructures[185]. Finally, recent studies on graphite intercalation compounds exhibit outstanding electric properties indicating the possibility of room temperature superconductivity[186]. The mechanical exfoliation of those material to few layers materials and their study at high pressure in the view of synthesising novel 2D structures[187] open up new avenues for scientific and technological breakthroughs. Their study was partially initiated during my PhD where I laid the technological foundation for the further exploration and advancement in this field.

Appendices

Appendix A

Delamination of multilayer graphene stacks from its substrate through wrinkle formation under high pressures

In this section we will describe a series of experiments we conducted on thin few-layer graphene (FLG) samples which where deposited on the Si/SiO$_2$ cube substrates described in the Section 4.2. The project was principally lead by Ian Rodriguez do Amaral and Alexis Forestier with my support in the experimental and sample preparation phases. Even if the results were already presented in the PhD thesis of Alexis Forestier, I prefer to summarize here the main results as they constitute an important basis to better understad results from other parts of this thesis. The samples were prepared by mechanical exfoliation from bulk graphite onto PDMS stamps and interesting flakes were found by optical microscopy estimating the sample thickness by optical contrast. They were then transferred directly onto the Si/SiO$_2$ cube priorly glued on the anvil by the one step PDMS-mediated procedure described in Section 2.4.1. We then performed AFM measurement which allowed to determine the thickness of the samples with $\sim 3\%$ accuracy which ranged between 9 and 110 layers. We submitted those samples to high pressure surrounded by different environments by changing the PTM used: we used Nitrogen, water, paraffin oil, 4:1 Methanol:Ethanol, and pure methanol and ethanol.

A.1 Experimental results

In Figure A.1 we can observe the optical micrograph obtained at different pressures for the various PTM used. Each column corresponds to an experiment with seven of them using Si/SiO$_2$ substrates, varying the PTM Figure A.1(a-f), and one with the sample directly on diamond using methanol Figure A.1(g). The first column Figure A.1(a) shows the evolution of the sample on Si/SiO$_2$ when submitted to high pressure in 4:1 Methanol:Ethanol. The sample is easily recognizable by the darker blue patch on the substrate indicating that the interference effect induced by the

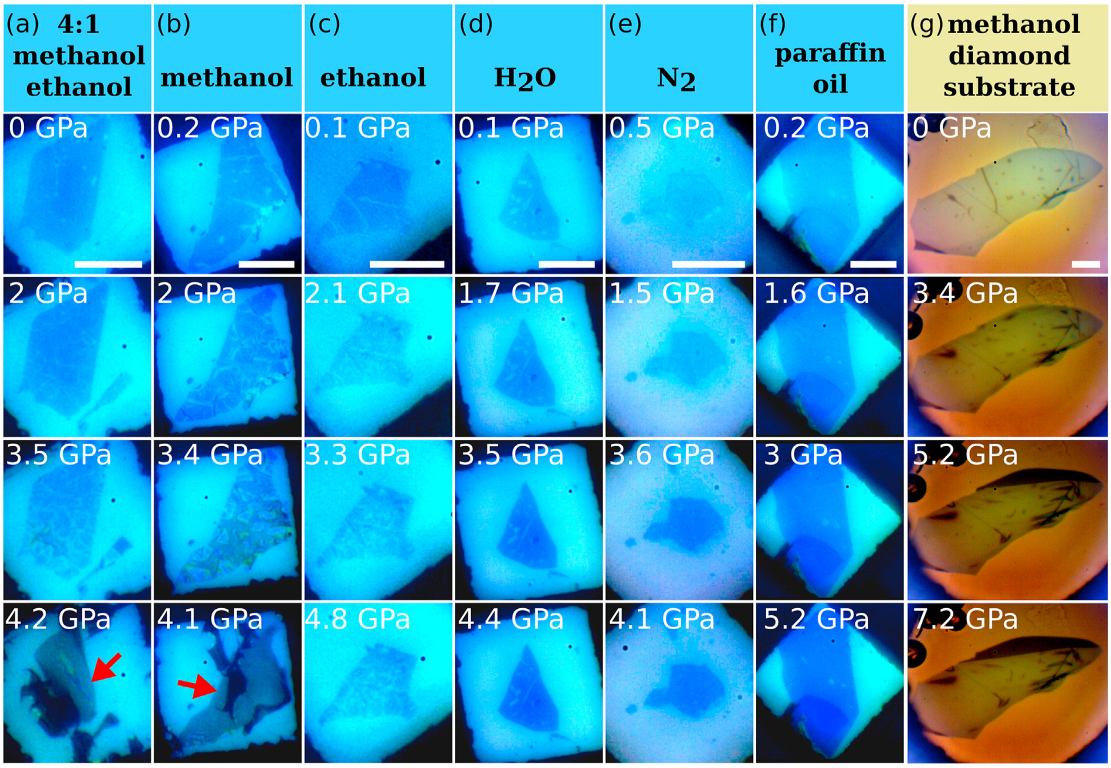

Figure A.1: Optical micrographs of the samples during the pressure cycle in different pressure transmitting media. In (a) and (b) red arrows point out the full detachment of the flake from the substrate.

thin SiO_2 layer of the substrate is present even after the change of refractive index of the medium and the spherical aberration due to the diamond and the PTM. Following the pressure evolution we observe that, with progressively increasing pressure thin whiter regions appear, with the sample turning dark grey when reaching 4.2 GPa. The sudden change in colour of the sample is an indicator of its full detachment from the substrate as the interference effects due to the presence of the silicon oxide layer disappear. Moreover, the sample was sometimes found to be moving around floating in the cell chamber confirming its complete detachment from its original site. Upon pressure release and the cell opening the sample was regularly washed off by the PTM or it ended up sticking to the top diamond surface. In addition to this impressive result, also the formation of the thin white lines can be assigned to the sample progressively detaching from the substrate forming wrinkles. The size and density of the wrinkles increases with pressure leading to the full unbinding of the sample we just described. Beside the sample peculiar behaviour at 4.2 GPa we can observe the appearance of a black region. This effect appears after the SiO_2 layer of the substrate fractures because of the mismatch in compressibility between the SiO_2 and the underlying bulk silicon. The bulk modulus of silicon is in fact found to be around three times higher then that of the oxide.

When we observed the behaviour of FLGs in other PTMs we can note that there is no comparable wrinkling and detachment when the sample is surrounded by pure water, nitrogen or paraffin oil Figure A.1(d-f). In water few wrinkles can be observed at the lowest pressure but no widening and detachment is observed when pressure is increased. One important difference with 4:1 Methanol:Ethanol is that water and nitrogen solidify at relatively low pressure, 1 and 2.4 GPa respectively [133], introducing the physical state of the PTM as a variable that may affect the detachment. Paraffin oil has thus also been used which has a solidification pressure of 7 GPa[133] with increasing viscosity with pressure. Using this PTM, however, no sign of wrinkling is observed up to 5.2 GPa which is the maximum pressure reached. Moreover, in the pressure range where nitrogen is liquid, FLG in 4:1 Methanol:Ethanol shows important wrinkling whilst it remains unchanged when pressure is increased in nitrogen. The question of whether the solidification of the PTM plays a role or not will be further discussed later in this section, however it is clear from those observations that it is not sufficient for explaining the behaviour of the FLG.

In order to get a clearer picture of the wrinkling and detachment that occurs in 4:1 Methanol:Ethanol we also studied the effect of pure methanol and ethanol as PTM. The sample evolution is shown in Figure A.1(b,c). In the case of ethanol we can observe an increasing wrinkling of the sample from 0.1 to 2.1 GPa but no total detachment up to the maximum pressure reached of 4.8 GPa. On the contrarily, above 3.3 GPa a partial flattening of the wrinkles back onto the substrate is observed. Differently, methanol behaves similarly to the 4:1 Methanol:Ethanol mixture with a gradual increase in the portion of detached surface up to 4.1 GPa where complete detachment is observed. To take into consideration when analysing those observations is that ethanol undergoes solidification from its liquid phase when it reaches 1.9 GPa[133]. Methanol, on the other hand, undergoes a gradual crystal-

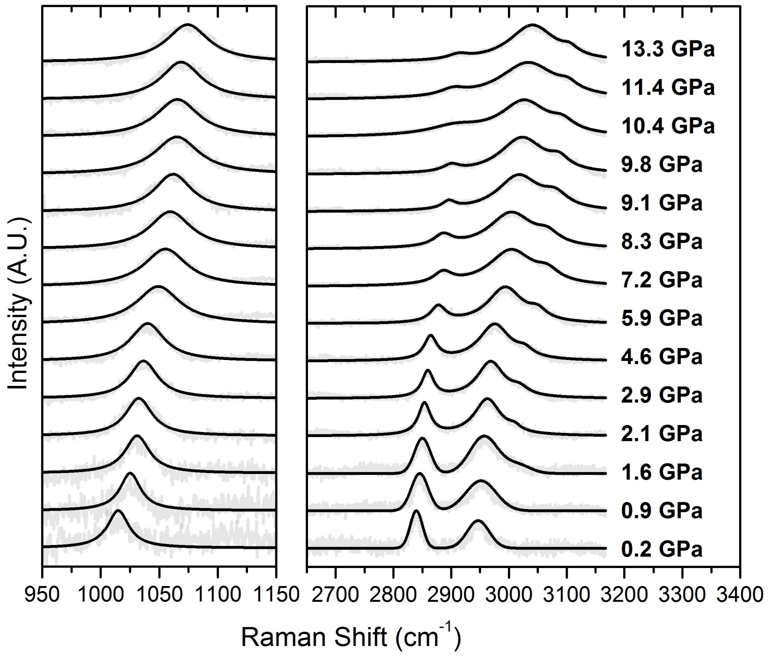

Figure A.2: Evolution of the Raman spectrum of methanol for increasing pressure. The spectra are normalized to their maximum value. The light grey line show the experimental data fitted by the black line.

lization starting from 3.5 GPa, however it is commonly found in a superpressed liquid state between 3.5 and 10.5 GPa due to its low symmetry and the strained hydrogen bonds of its molecules[134]. The Raman spectra of methanol taken at different pressures (Figure A.2) does not show significant changes in the pressure range studied indicating the experiment was performed in its superpressed state.

In addition to that, we performed several other experiments in 4:1 Methanol:Ethanol with samples supported on Si/SiO$_2$ which aimed to determine the dependency of the phenomenon on the number of graphene layers in the sample. We measured samples counting 9, 30, 50 and 110 layers and their pressure evolution is shown in Figure A.3. We observe that the detachment pressure does not depend on the sample thickness but occurs around 4 GPa on each sample. The striking difference is however the morphology of the wrinkles that largely changes from one sample and the other.

In order to get quantitative results on the wrinkling we performed image analysis on the micrographs. Figure A.4 shows a summary the computed ratio of detached sample surface compared to the total sample area for the experiments shown in Figure A.1 on Si/SiO$_2$ substrate and Figure A.3. Due to the low quality imaging in the DAC the boundaries of the wrinkle could not be precisely defined so we estimated the measurement error by taking upper and lower boundaries on their width as shown in Figure A.5. This graph shows an interesting trend that characterize all the experiments involving methanol and 4:1 Methanol:Ethanol PTMs. All the points seem to follow a common trend that is highlighted by the light blue band. The progressive unbinding can be well described by a logistic function which is independent on the number of layers. In the case of ethanol and

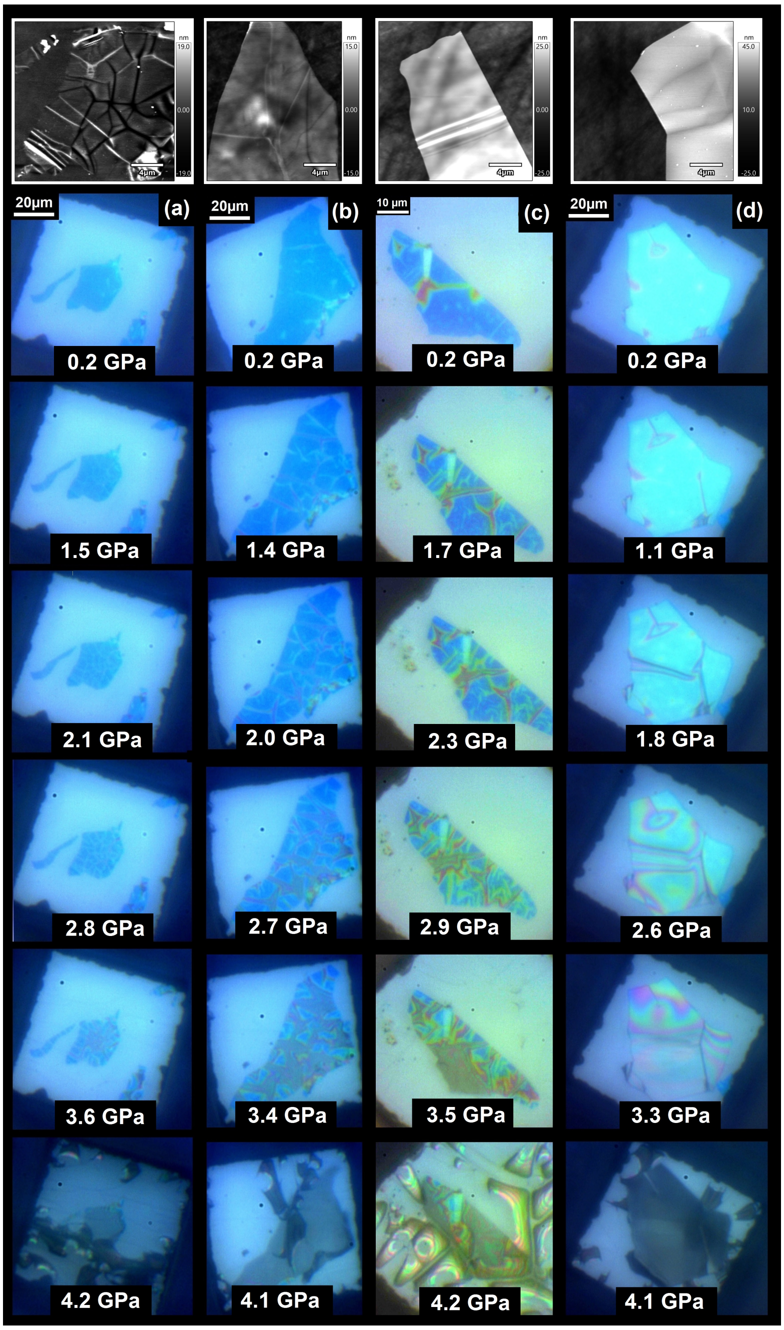

Figure A.3: Optical images of the pressure evolution of the sample morphology for a series of experiments conducted using methanol as PTM and FLG of different thicknesses. From left to right the sample measured (a) 3 nm (9 layers), (b) 10 nm (30 layers), (c) 20 nm (60 layers) and (d) 37 nm (110 layers) in thickness. The top line shows AFM imaging of the sample prior to the pressure cycle.

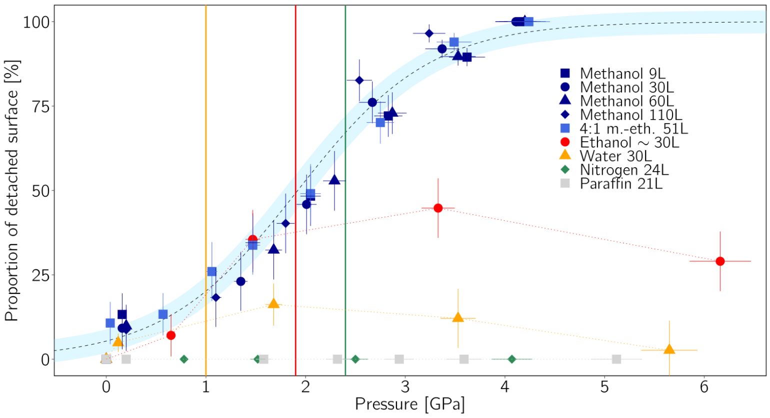

Figure A.4: Evolution of the proportion of detached sample surface as a function of pressure for the performed experiments. The yellow, red and green solid lines show the solidification pressure of water, ethanol and nitrogen respectively. A light blue band and a dashed black line show a sigmoidal fit of the data that help the visualization of the wrinkle evolution in Methanol and 4:1 Methanol:Ethanol. Upper and lower boundaries on the wrinkle width were used to define the error bars on the detached surface portion.

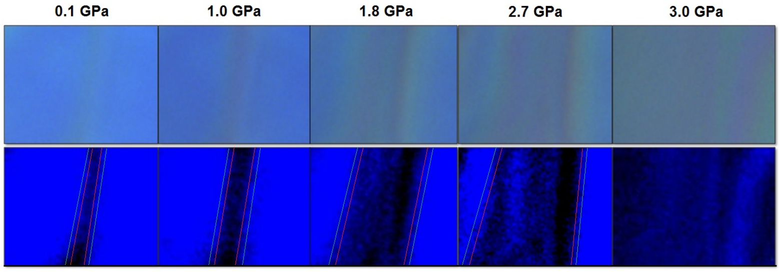

Figure A.5: Optical images of a selected wrinkle for height and width measurements. The top images show the original optical image. The bottom ones are contrast enhanced numerically. The red and green lines show respectively the lower and upper boundaries of the wrinkle.

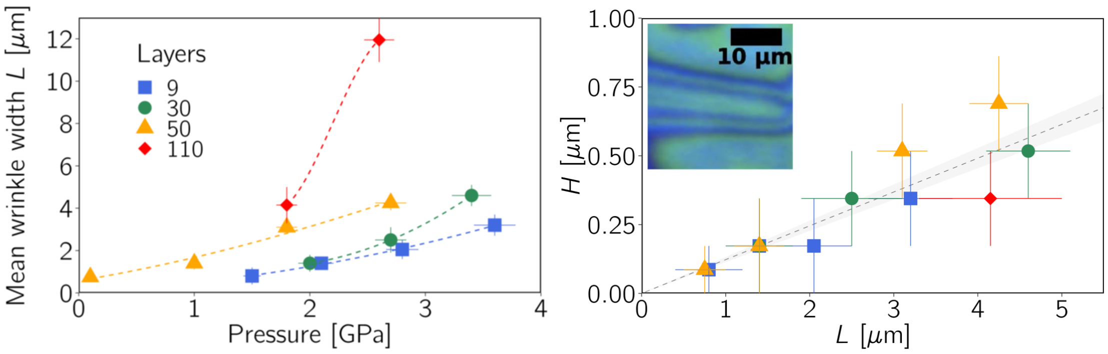

(a) **(b)**

Figure A.6: (a) Mean wrinkle width L plotted as a function of pressure for four sample thicknesses. (b) height of the wrinkle H measured by optical interference with the substrate as a function of the wrinkle width shown in (a). The inset shows the optical interference pattern of a wrinkle in a region of a 110L-graphene used to determine the height. The black dashed line is the linear fit of the heights.

water used as PTMs this trend is also respected up to the solidification point. Finally, as we previously mentioned, no wrinkling is observed in the case of nitrogen and silicon oil. Those analysis lead us to the conclusion that: 1. the sample thickness does not influence the portion of sample detachment and 2. the the observed detachment is not only governed by the mechanical response to pressure but also by a specific chemical interaction between the PTM molecules and the multilayer graphene sample

In our analysis we also measured the dependencies of the wrinkles width L and height H on the number of layers for the experiments in 4:1 Methanol:Ethanol. The results are shown in Figure A.6a and Figure A.6b. We can observe a increase of the wrinkle width with the number of layers. The general trend with pressure is also the increase in the width with increasing pressure. The evaluation of the wrinkle height is done taking advantage of the interference effects produced by the wrinkle. Considering the wrinkle shape as a regular wave we counted the number of fringes (lighter and darker blue fringes) that appeared around the wrinkle due to the incoming incident microscope white light. We could estimate the height at the centre by using the condition of constructive and destructive interference given by:

$$d = (k+1)\frac{\lambda}{2n} \tag{A.1}$$

with an odd k for constructive interference and an even k for destructive interference. λ is the wavelength of light, and n the 4:1 Methanol:Ethanol pressure transmitting medium refractive index in the low pressure range assumed to be $n = 1.45$[188]. From Figure A.6b, H shows no dependency on the number of layers.

Those experimental evidences show that when wrinkles form at high pressure the PTM, if in liquid phase, is absorbed through the newly created nanoporous channels. Increasing pressure favours the PTM injection resulting in the expansion of the wrinkles leading to the total sample detachment from the substrate.

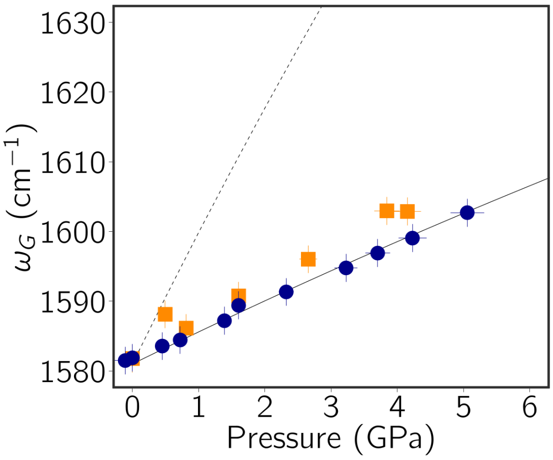

Figure A.7: Pressure evolution of the G-band frequency as a function of pressure for a sample of multilayer graphene 8 nm thick. Orange squares show the measurements with the sample in Nitrogen PTM and blue dots for 4:1 Methanol:Ethanol PTM. The black solid line show the evolution of bulk graphite[26] and the dotted one the scenario where the totality of strain is transferred from the substrate to the sample.

A.2 Discussion and modelling

The phenomenon of pressure-induced wrinkling and detachment of a multilayer graphene sample in alcohol PTM may seem counter-intuitive at first. Normally, applying pressure it would be expected to increase the adhesion between graphene and substrate, due to the reduction of the graphene-substrate distance. However, in this case, the opposite behaviour is observed. In the following paragraphs, we will analyse the experimental data presented in the previous section and propose a model to explain this unexpected behaviour, taking into account the properties of the substrate and PTM.

To understand the formation of wrinkles, we need to consider the difference in compressibility between the nanometric thin graphite sample and the substrate. The in-plane bulk modulus of graphite, $-r\partial P/\partial r \sim 1250$ GPa, is approximately four time larger than that of the substrate material ($\sim$ 294 GPa)[189, 26], resulting in larger strain at the substrate surface compared to the strain in bulk graphite under the same pressure. This strain difference leads to the buckling of the graphene membrane and the formation of wrinkles.

In our *in-situ* Raman spectroscopy experiments, the G-band frequency ω_G evolution with pressure, shown in Figure A.7, behave similarly in the multilayer graphene sample as in bulk graphite (solid black line) indicating that the adhesion between the sample and substrate does not induce additional strain in the sample. However, the sample is still in contact with the compressed substrate and can be displaced at specific regions or points due to adhesion. These displacements are likely to dissipate through out-of-plane displacements of the membrane, resulting in the observed wrinkling. Similar wrinkling effects have been observed in previous works where graphene was strained through thermal expansion mismatch[190, 191] or using flexible polymer substrates[192].

While the mechanical considerations explain the formation of wrinkles, they do not fully explain why this phenomenon is observed with alcohol PTMs like methanol and ethanol but not with other PTMs such as water, nitrogen, or paraffin oil. The physical state of the PTM plays a role here. A solid PTM at the sample surface can hinder wrinkle formation, preventing the membrane from buckling in the perpendicular direction. On the other hand, a liquid PTM allows for buckling and can even diffuse between the sample and substrate, enlarging the wrinkles' channels.

The crystallization of water and pure ethanol PTMs at respectively 1 and 1.9 GPa is thus responsible for prevent the full detachment of the flake even though a principle of wrinkle formation is observed. However, when paraffin oil and nitrogen PTMs are used no wrinkling is observed even if the former remains liquid throughout the studied pressure range and the latter solidifies only when 2.4 GPa is reached.

To understand our observations we have thus to consider the combination of several factors:

- the mismatch in the in-plane bulk modulus of the multi-layer graphite and the substrate leads to local buckling of the flake when increasing pressure;
- the wrinkles formed as such enlarge due to infiltration of certain PTMs making the wrinkles visible through optical microscopy observation of the sample.
- Finally, when the PTM is solid the wrinkling process is stopped but the liquid phase alone is not sufficient to completely describe the experimental evidences.

The unique behaviour of alcohol-PTM interaction at high pressure compared to other PTMs can be explained by the fact that methanol-graphene interaction is stronger than the intermolecular interaction between methanol molecules themself. This strong interaction leads to the preferential formation of a fully adsorbed methanol layer before the stacking of additional layers on the graphite surface[193, 194]. Methanol can infiltrate inside the wrinkles under the graphene flake, expanding the channels and eventually leading to complete detachment.

To test the hypothesis, an additional high-pressure experiment was performed by directly transferring the multilayer flake onto a diamond anvil using pure methanol as the PTM. The sample thickness was 16 ± 3 nm (48 ± 9 layers). Differently to the Si/SiO$_2$ substrate diamond has a linear bulk modulus of $\sim$1330 GPa which is considerably close to the in-plane bulk modulus of graphite[45]. Little to no wrinkling is thus expected in this case. Figure A.1(g) shows the sample evolution with pressure. We note how partial detachment of the sample is observed mostly on the sample edges appearing above 5.2 GPa. This experiment agrees with our hypothesis of a detachment mechanism mediated by the insertion of alcohol PTM beneath the flake.

To gain a deeper understanding of the physical processes involved, a quantitative analysis was performed. Wrinkles form to relieve stretching energy caused by the contraction of the substrate via a well-known scenario[195]. When the

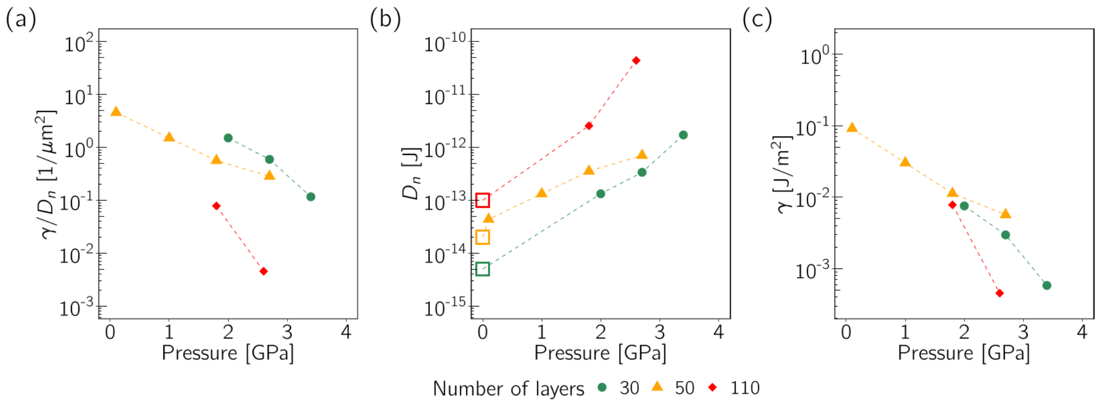

Figure A.8: Pressure evolution of the physical parameters obtain combining the experimental result and our modelling of the wrinkle formation. The $\frac{\gamma}{D_n}$ ratio as a function of the pressure P obtained from Equation A.3 is shown in (a). (b) Pressure evolution of the bending rigidity D_n when assuming a constant adhesion energy $\gamma = 0.2\ \mathrm{J\,m^{-2}}$. The empty symbols correspond to the expected zero-pressure D_0^n values[198]. (c) Pressure evolution of γ assuming an additive layer-dependent D_0^n[198]. Dashed lines are guides to the eye. Error bars were omitted due to the logarithmic scale.

stretching energy is relieved, the equilibrium shape of one wrinkle mainly results from a compromise between adhesion energy and bending energy. In addition, the network of wrinkles is connected and always reaches the flake's edges. Hence, we assume that the liquid PTM can freely move underneath graphene filling the wrinkles. Furthermore, from the observation that the wrinkle height is much lower that its width we worked in the small slope approximation for our model. The wrinkle profile $h(x)$ as a function of the x coordinate orthogonal to the wrinkle length can be obtained by a straightforward minimization of the adhesion and binding energy [196, 197]:

$$h(x) = \frac{H}{2}\left[1 + \cos\left(2\pi\frac{x}{L}\right)\right] \tag{A.2}$$

where H and L are the wrinkle height and width as shown in Figure A.6. The relation between L and H are also imposed by the energy minimization [197]:

$$\frac{\gamma}{D_n} = 2\pi^4\frac{H^2}{L^4} \tag{A.3}$$

where γ is the adhesion energy per unit area and D_n is the bending rigidity of n-layer graphene. As γ describes the interaction between the superficial graphene layer in contact with the substrate we do not expect it to depend on the number of layers in the flake. From the measurements shown in Figure A.6 using Equation A.3 we can derive the ratio $\frac{\gamma}{D_n}$ which is shown in Figure A.8(a) as a function of pressure and the number of layers. We can note a striking decrease in $\frac{\gamma}{D_n}$ greater then an order of magnitude when increasing pressure up to 3-4 GPa. This effect might be originated by both an increase of D_n, a decrease of γ or both effects combined.

The increase of D_n can be induced by a reduced sliding mobility of the individual graphene layers due to increase proximity. Supporting this hypothesis are evidences of stacking faults forming in multi-layer graphene strained nanocomposites[199] which could participate in inter-monolayer sliding. Such movement could be decreased under pressure due to the work required to separate the graphene layers during sliding in the presence of an atomic corrugation between the sheets. Since the energy of stacking faults per unit area in Bernal stacking[199] is similar to the energy per area to separate two graphene sheets by 1Å under a pressure of 1 GPa, the formation of dislocations can be strongly influenced by pressure.

The adhesion energy between a monolayer of graphene and a silicon oxide substrate in vacuum is approximately 0.45 $\mathrm{J\,m^{-2}}$[200]. For multi-layer graphene in a vacuum, the adhesion energy is lower at around 0.3 $\mathrm{J\,m^{-2}}$ due to partial detachment[200]. When immersed in a liquid medium, the adhesion energy of multi-layer graphene on a silicon oxide substrate is expected to decrease by about 40%[201] so a reasonable value for the adhesion energy in an ethanol medium at zero pressure is estimated to be 0.2 $\mathrm{J\,m^{-2}}$. Figure A.8(b) plots the change in bending rigidity D_n using this value for the adhesion energy γ and assuming it remains constant regardless of pressure or the number of graphene layers. The figure illustrates how the bending rigidity D_n increases with pressure and the number of layers. These values are compared with the expected bending rigidity at zero pressure, denoted as D_0^n, which was determined through AFM measurements on graphene bubbles of varying thickness[198]. The measured values for D_0^n are $D_0^{30} \approx 5 \cdot 10^{-14}$ J, $D_0^{50} \approx 2 \cdot 10^{-14}$ J and $D_0^{110} \approx 10^{-13}$ J (with $D_0^1 \approx 2.7 \cdot 10^{-19}$ J[43]). It's worth noting that there is a significant variation in proposed values for D_0^1[202, 203]. The observed evolution of $D_n(P)$, in Figure A.8(b), is in agreement with these extrapolated values (empty symbols). In summary, this first scenario suggests that an increase in bending modulus occurs due to a reduction in interlayer sliding (i.e., increased interlayer friction) as pressure increases.

The second scenario we can consider is that of a decrease in the adhesion energy, which is strongly supported by the fact that an increase in the wrinkle width eventually leads to complete detachment of graphene, without subsequent reattachment of the multi-layer graphene to the substrate. In this case, the evolution of the adhesion energy γ with pressure represents the effective macroscopic adhesion energy, which may account for the formation of non-visible wrinkles at the sub-micrometric scale under pressure.

If we assume D_n constant with its values at ambient pressure for a given thickness D_0^{30}, D_0^{50} and D_0^{110} we obtain the evolution shown in Figure A.8(c) for $\gamma(P)$. The figure shows a trend independent on the sample thickness for the three sample studied as well as a value in agreement with the expected 0.2 $\mathrm{J\,m^{-2}}$ for the extrapolation to zero pressure.

A more general view may consider that both D_n and γ are varying with pressure, each contributing to the observed multi-layer graphene behaviour. The results of this work can be extended considering different substrates using more compressible materials, such as polymers. A combination of mechanical and wetting methods could then appear as possible new paths for van der Waals 2D systems detachment and transfer to other substrates[204]. Our results may also contribute to better understand the response of graphene based coatings in different environments submitted to mechanical constraints as in their use in tribological contacts[205, 206].

A.3 Conclusions

The series of experiment we presented here demonstrated the possibility of detaching graphene multilayer flakes of thickness ranging from 9 to 110 layers from their substrate by applying pressure. Our results show that both the substrate and the PTM properties play a fundamental role in the phenomenon. In particular full detachment could only be achieved when the PTM was in liquid state at $\sim$ 4 GPa and using Si/SiO$_2$ substrates. A gradual delamination of the flake appeared in the form of wrinkling for which the total detached surface followed a behaviour independent on the sample thickness, evolving with pressure following a sigmoidal curve trend. The wrinkling was found to be favoured by the use of methanol, ethanol and their mixtures when the sample was supported on Si/SiO$_2$. The width of each individual wrinkle is found to increase with pressure and with the number of layers composing the sample. Our theoretical model describing the wrinkling showed that the ratio of the effective adhesive energy and the bending modulus γ/D_n decreases with pressure. The decrease of γ and the increase of D_n are both quantitatively consistent with our results. Finally, we have shown that the wrinkle area is a function of pressure, and that the wrinkle geometry at that pressure depends on the number of graphene layers. This offers opportunities to control the wrinkle average radius of curvature and its extension, which may impact optical [207] or chemical properties [208] to a great extent.

Bibliography

[1] K. S. Novoselov et al. "Electric Field Effect in Atomically Thin Carbon Films". In: *Science* 306.5696 (2004), pp. 666–669. DOI: `10.1126/science.1102896`.

[2] T. W. Ebbesen et al. "Electrical conductivity of individual carbon nanotubes". In: *Nature* 382.6586 (July 1996), pp. 54–56. DOI: `10.1038/382054a0`.

[3] A. Yu. Kasumov et al. "Supercurrents Through Single-Walled Carbon Nanotubes". In: *Science* 284.5419 (1999), pp. 1508–1511. DOI: `10.1126/science.284.5419.1508`.

[4] Yuanbo Zhang et al. "Experimental observation of the quantum Hall effect and Berry's phase in graphene". In: *Nature* 438.7065 (Nov. 2005), pp. 201–204. DOI: `10.1038/nature04235`.

[5] Jiong Yang et al. "Atomically thin optical lenses and gratings". In: *Light: Science & Applications* 5.3 (Mar. 2016), e16046–e16046. DOI: `10.1038/lsa.2016.46`.

[6] Feng Wang et al. "Gate-Variable Optical Transitions in Graphene". In: *Science* 320.5873 (2008), pp. 206–209. DOI: `10.1126/science.1152793`.

[7] H. Kataura et al. "Optical properties of single-wall carbon nanotubes". In: *Synthetic Metals* 103.1 (1999). International Conference on Science and Technology of Synthetic Metals, pp. 2555–2558. DOI: `https://doi.org/10.1016/S0379-6779(98)00278-1`.

[8] Jianwei Che, Tahir Çagin, and William A Goddard III. "Thermal conductivity of carbon nanotubes". In: *Nanotechnology* 11.2 (June 2000), p. 65. DOI: `10.1088/0957-4484/11/2/305`.

[9] Alexander A. Balandin et al. "Superior Thermal Conductivity of Single-Layer Graphene". In: *Nano Letters* 8.3 (2008). PMID: 18284217, pp. 902–907. DOI: `10.1021/nl0731872`.

[10] Changgu Lee et al. "Measurement of the Elastic Properties and Intrinsic Strength of Monolayer Graphene". In: *Science* 321.5887 (2008), pp. 385–388. DOI: `10.1126/science.1157996`.

[11] Min-Feng Yu et al. "Strength and Breaking Mechanism of Multiwalled Carbon Nanotubes Under Tensile Load". In: *Science* 287.5453 (2000), pp. 637–640. DOI: `10.1126/science.287.5453.637`.

[12] Min-Feng Yu et al. “Tensile Loading of Ropes of Single Wall Carbon Nanotubes and their Mechanical Properties”. In: *Phys. Rev. Lett.* 84 (24 June 2000), pp. 5552–5555. DOI: 10.1103/PhysRevLett.84.5552.

[13] K. I. Bolotin et al. “Temperature-Dependent Transport in Suspended Graphene”. In: *Phys. Rev. Lett.* 101 (9 Aug. 2008), p. 096802. DOI: 10.1103/PhysRevLett.101.096802.

[14] Andrzej Taube et al. “Temperature-Dependent Thermal Properties of Supported MoS2 Monolayers”. In: *ACS Applied Materials & Interfaces* 7.9 (2015). PMID: 25706435, pp. 5061–5065. DOI: 10.1021/acsami.5b00690.

[15] Kenneth S. Burch, David Mandrus, and Je-Geun Park. “Magnetism in two-dimensional van der Waals materials”. In: *Nature* 563.7729 (Nov. 2018), pp. 47–52. DOI: 10.1038/s41586-018-0631-z.

[16] Kin Fai Mak, Jie Shan, and Daniel C. Ralph. “Probing and controlling magnetic states in 2D layered magnetic materials”. In: *Nature Reviews Physics* 1.11 (Nov. 2019), pp. 646–661. DOI: 10.1038/s42254-019-0110-y.

[17] Yuanbo Zhang et al. “Direct observation of a widely tunable bandgap in bilayer graphene”. In: *Nature* 459.7248 (June 2009), pp. 820–823. DOI: 10.1038/nature08105.

[18] Luis A. Jauregui et al. “Electrical control of interlayer exciton dynamics in atomically thin heterostructures”. In: *Science* 366.6467 (2019), pp. 870–875. DOI: 10.1126/science.aaw4194.

[19] Anis Chiout et al. “Extreme mechanical tunability in suspended MoS2 resonator controlled by Joule heating”. In: *npj 2D Materials and Applications* 7.1 (Mar. 2023), p. 20. DOI: 10.1038/s41699-023-00383-3.

[20] Fabio Medeghini et al. “High-Pressure Effect on the Optical Extinction of a Single Gold Nanoparticle”. In: *ACS Nano* 12.10 (2018), pp. 10310–10316. DOI: 10.1021/acsnano.8b05539.

[21] R.S. Alencar et al. “Raman resonance tuning of quaterthiophene in filled carbon nanotubes at high pressures”. In: *Carbon* 173 (2021), pp. 163–173. DOI: https://doi.org/10.1016/j.carbon.2020.10.083.

[22] Denis Machon et al. “Perspective: High pressure transformations in nanomaterials and opportunities in material design”. In: *Journal of Applied Physics* 124.16 (Oct. 2018), p. 160902. DOI: 10.1063/1.5045563.

[23] Luiz Gustavo Pimenta Martins et al. “Raman evidence for pressure-induced formation of diamondene”. In: *Nature Communications* 8.1 (July 2017), p. 96. DOI: 10.1038/s41467-017-00149-8.

[24] Mário S. C. Mazzoni and H. Chacham. “Bandgap closure of a flattened semiconductor carbon nanotube: A first-principles study”. In: *Applied Physics Letters* 76.12 (Mar. 2000), pp. 1561–1563. DOI: 10.1063/1.126096.

[25] Paul E. Lammert, Peihong Zhang, and Vincent H. Crespi. "Gapping by Squashing: Metal-Insulator and Insulator-Metal Transitions in Collapsed Carbon Nanotubes". In: *Phys. Rev. Lett.* 84 (11 Mar. 2000), pp. 2453–2456. DOI: 10.1103/PhysRevLett.84.2453.

[26] M. Hanfland, H. Beister, and K. Syassen. "Graphite under pressure: Equation of state and first-order Raman modes". In: *Phys. Rev. B* 39 (17 June 1989), pp. 12598–12603. DOI: 10.1103/PhysRevB.39.12598.

[27] M. Chorro et al. "Structural properties of carbon peapods under extreme conditions studied using in situ x-ray diffraction". In: *Phys. Rev. B* 74 (20 Nov. 2006), p. 205425. DOI: 10.1103/PhysRevB.74.205425.

[28] N. Bendiab et al. "Structural determination of iodine localization in single-walled carbon nanotube bundles by diffraction methods". In: *Phys. Rev. B* 69 (19 May 2004), p. 195415. DOI: 10.1103/PhysRevB.69.195415.

[29] W.Q. Neves et al. "Effects of pressure on the structural and electronic properties of linear carbon chains encapsulated in double wall carbon nanotubes". In: *Carbon* 133 (2018), pp. 446–456. DOI: https://doi.org/10.1016/j.carbon.2018.01.084.

[30] Merijntje S. Bronsgeest et al. "Strain Relaxation in CVD Graphene: Wrinkling with Shear Lag". In: *Nano Letters* 15.8 (2015). PMID: 26171667, pp. 5098–5104. DOI: 10.1021/acs.nanolett.5b01246.

[31] Diedrich A. Schmidt, Taisuke Ohta, and Thomas E. Beechem. "Strain and charge carrier coupling in epitaxial graphene". In: *Phys. Rev. B* 84 (23 Dec. 2011), p. 235422. DOI: 10.1103/PhysRevB.84.235422.

[32] Xiaoyan Fan, Ryo Nouchi, and Katsumi Tanigaki. "Effect of Charge Puddles and Ripples on the Chemical Reactivity of Single Layer Graphene Supported by SiO2/Si Substrate". In: *The Journal of Physical Chemistry C* 115.26 (2011), pp. 12960–12964. DOI: 10.1021/jp202273a.

[33] Eunji Ji et al. "Substrate effect on doping and degradation of graphene". In: *Carbon* 184 (2021), pp. 651–658. DOI: https://doi.org/10.1016/j.carbon.2021.08.048.

[34] Alexis Forestier et al. "Strain and Piezo-Doping Mismatch between Graphene Layers". In: *The Journal of Physical Chemistry C* 124.20 (2020), pp. 11193–11199. DOI: 10.1021/acs.jpcc.0c01898.

[35] Abraao C. Torres-Dias et al. "Chirality-dependent mechanical response of empty and water-filled single-wall carbon nanotubes at high pressure". In: *Carbon* 95 (2015), pp. 442–451. DOI: https://doi.org/10.1016/j.carbon.2015.08.032.

[36] Denis Machon et al. "Raman scattering studies of graphene under high pressure". In: *Journal of Raman Spectroscopy* 49.1 (2018), pp. 121–129. DOI: https://doi.org/10.1002/jrs.5284.

[37] Rudolf Peierls. "Quelques propriétés typiques des corps solides". In: *Annales de l'institut Henri Poincaré*. Vol. 5. 3. 1935, pp. 177–222.

[38] Lev Davidovich Landau and Evgenii Mikhailovich Lifshitz. *Statistical Physics: Volume 5*. Vol. 5. Elsevier, 2013.

[39] Jannik C. Meyer et al. “The structure of suspended graphene sheets”. In: *Nature* 446.7131 (Mar. 2007), pp. 60–63. DOI: `10.1038/nature05545`.

[40] Sumio Iijima. “Helical microtubules of graphitic carbon”. In: *Nature* 354.6348 (Nov. 1991), pp. 56–58. DOI: `10.1038/354056a0`.

[41] R.S. Alencar et al. “Pressure-induced radial collapse in few-wall carbon nanotubes: A combined theoretical and experimental study”. In: *Carbon* 125 (2017), pp. 429–436. DOI: `https://doi.org/10.1016/j.carbon.2017.09.044`.

[42] Y. Magnin et al. “Collapse phase diagram of carbon nanotubes with arbitrary number of walls. Collapse modes and macroscopic analog”. In: *Carbon* 178 (2021), pp. 552–562. DOI: `https://doi.org/10.1016/j.carbon.2021.03.031`.

[43] Abraao C. Torres-Dias et al. “From mesoscale to nanoscale mechanics in single-wall carbon nanotubes”. In: *Carbon* 123 (2017), pp. 145–150. DOI: `https://doi.org/10.1016/j.carbon.2017.07.036`.

[44] Jimmy Nicolle et al. “Pressure-Mediated Doping in Graphene”. In: *Nano Letters* 11.9 (2011). PMID: 21805986, pp. 3564–3568. DOI: `10.1021/nl201243c`.

[45] C. Bousige et al. “Biaxial Strain Transfer in Supported Graphene”. In: *Nano Letters* 17.1 (2017). PMID: 28073255, pp. 21–27. DOI: `10.1021/acs.nanolett.6b02981`.

[46] Zhuchen Tao et al. “Raman spectroscopy study of sp2 to sp3 transition in bilayer graphene under high pressures”. In: *Applied Physics Letters* 116.13 (Apr. 2020). 133101. DOI: `10.1063/1.5135027`.

[47] Y. W. Sun et al. “3D Strain in 2D Materials: To What Extent is Monolayer Graphene Graphite?” In: *Phys. Rev. Lett.* 123 (13 Sept. 2019), p. 135501. DOI: `10.1103/PhysRevLett.123.135501`.

[48] John E. Proctor et al. “High-pressure Raman spectroscopy of graphene”. In: *Phys. Rev. B* 80 (7 Aug. 2009), p. 073408. DOI: `10.1103/PhysRevB.80.073408`.

[49] Paras et al. “A Review on Low-Dimensional Nanomaterials: Nanofabrication, Characterization and Applications”. In: *Nanomaterials* 13.1 (2023). DOI: `10.3390/nano13010160`.

[50] H. W. Kroto et al. “C60: Buckminsterfullerene”. In: *Nature* 318.6042 (Nov. 1985), pp. 162–163. DOI: `10.1038/318162a0`.

[51] D. S. Bethune et al. “Cobalt-catalysed growth of carbon nanotubes with single-atomic-layer walls”. In: *Nature* 363.6430 (June 1993), pp. 605–607. DOI: `10.1038/363605a0`.

[52] A. K. Geim and K. S. Novoselov. “The rise of graphene”. In: *Nature Materials* 6.3 (Mar. 2007), pp. 183–191. DOI: `10.1038/nmat1849`.

[53] Zhidong Han and Alberto Fina. "Thermal conductivity of carbon nanotubes and their polymer nanocomposites: A review". In: *Progress in Polymer Science* 36.7 (2011). Special Issue on Composites, pp. 914–944. DOI: `https://doi.org/10.1016/j.progpolymsci.2010.11.004`.

[54] Edward McCann and Mikito Koshino. "The electronic properties of bilayer graphene". In: *Reports on Progress in Physics* 76.5 (Apr. 2013), p. 056503. DOI: `10.1088/0034-4885/76/5/056503`.

[55] Yuan Cao et al. "Unconventional superconductivity in magic-angle graphene superlattices". In: *Nature* 556.7699 (Apr. 2018), pp. 43–50. DOI: `10.1038/nature26160`.

[56] M.S. Dresselhaus et al. "Raman spectroscopy of carbon nanotubes". In: *Physics Reports* 409.2 (2005), pp. 47–99. DOI: `https://doi.org/10.1016/j.physrep.2004.10.006`.

[57] Bing-Sui Lu. "The Casimir Effect in Topological Matter". In: *Universe* 7.7 (2021). DOI: `10.3390/universe7070237`.

[58] A. H. Castro Neto et al. "The electronic properties of graphene". In: *Rev. Mod. Phys.* 81 (1 Jan. 2009), pp. 109–162. DOI: `10.1103/RevModPhys.81.109`.

[59] R Saito, G Dresselhaus, and M S Dresselhaus. *Physical Properties of Carbon Nanotubes*. PUBLISHED BY IMPERIAL COLLEGE PRESS and DISTRIBUTED BY WORLD SCIENTIFIC PUBLISHING CO., 1998. DOI: `10.1142/p080`.

[60] Phaedon Avouris, Zhihong Chen, and Vasili Perebeinos. "Carbon-based electronics". In: *Nature Nanotechnology* 2.10 (Oct. 2007), pp. 605–615. DOI: `10.1038/nnano.2007.300`.

[61] Gao Yang et al. "Structure of graphene and its disorders: a review". en. In: *Sci Technol Adv Mater* 19.1 (Aug. 2018), pp. 613–648.

[62] Mauricio Terrones et al. "Graphene and graphite nanoribbons: Morphology, properties, synthesis, defects and applications". In: *Nano Today* 5.4 (2010), pp. 351–372. DOI: `https://doi.org/10.1016/j.nantod.2010.06.010`.

[63] Ernst Richter and K. R. Subbaswamy. "Theory of Size-Dependent Resonance Raman Scattering from Carbon Nanotubes". In: *Phys. Rev. Lett.* 79 (14 Oct. 1997), pp. 2738–2741. DOI: `10.1103/PhysRevLett.79.2738`.

[64] Andrea C. Ferrari and Denis M. Basko. "Raman spectroscopy as a versatile tool for studying the properties of graphene". In: *Nature Nanotechnology* 8.4 (Apr. 2013), pp. 235–246. DOI: `10.1038/nnano.2013.46`.

[65] Jiang-Bin Wu et al. "Raman spectroscopy of graphene-based materials and its applications in related devices". In: *Chem. Soc. Rev.* 47 (5 2018), pp. 1822–1873. DOI: `10.1039/C6CS00915H`.

[66] Ludger Wirtz and Angel Rubio. "The phonon dispersion of graphite revisited". In: *Solid State Communications* 131.3 (2004), pp. 141–152. DOI: `https://doi.org/10.1016/j.ssc.2004.04.042`.

[67] Peter Y. Yu and Manuel Cardona. *Fundamentals of Semiconductors Physics and Materials Properties.* 2010. DOI: https://doi.org/10.1007/978-3-642-00710-1.

[68] Dominik Metten et al. "All-Optical Blister Test of Suspended Graphene Using Micro-Raman Spectroscopy". In: *Phys. Rev. Appl.* 2 (5 Nov. 2014), p. 054008. DOI: 10.1103/PhysRevApplied.2.054008.

[69] Ji Eun Lee et al. "Optical separation of mechanical strain from charge doping in graphene". In: *Nature Communications* 3.1 (Aug. 2012), p. 1024. DOI: 10.1038/ncomms2022.

[70] Guillaume Froehlicher and Stéphane Berciaud. "Raman spectroscopy of electrochemically gated graphene transistors: Geometrical capacitance, electron-phonon, electron-electron, and electron-defect scattering". In: *Phys. Rev. B* 91 (20 May 2015), p. 205413. DOI: 10.1103/PhysRevB.91.205413.

[71] A. C. Ferrari and J. Robertson. "Resonant Raman spectroscopy of disordered, amorphous, and diamondlike carbon". In: *Phys. Rev. B* 64 (7 July 2001), p. 075414. DOI: 10.1103/PhysRevB.64.075414.

[72] Nicola Ferralis. "Probing mechanical properties of graphene with Raman spectroscopy". In: *Journal of Materials Science* 45.19 (Oct. 2010), pp. 5135–5149. DOI: 10.1007/s10853-010-4673-3.

[73] Nedjma Bendiab et al. "Unravelling external perturbation effects on the optical phonon response of graphene". In: *Journal of Raman Spectroscopy* 49.1 (2018), pp. 130–145. DOI: https://doi.org/10.1002/jrs.5267.

[74] The An Nguyen et al. "Excitation Energy Dependent Raman Signatures of ABA- and ABC-stacked Few-layer Graphene". In: *Scientific Reports* 4.1 (Apr. 2014), p. 4630. DOI: 10.1038/srep04630.

[75] P. H. Tan et al. "The shear mode of multilayer graphene". In: *Nature Materials* 11.4 (Apr. 2012), pp. 294–300. DOI: 10.1038/nmat3245.

[76] L.M. Malard et al. "Raman spectroscopy in graphene". In: *Physics Reports* 473.5 (2009), pp. 51–87. DOI: https://doi.org/10.1016/j.physrep.2009.02.003.

[77] A. Jorio et al. "G-band resonant Raman study of 62 isolated single-wall carbon nanotubes". In: *Phys. Rev. B* 65 (15 Mar. 2002), p. 155412. DOI: 10.1103/PhysRevB.65.155412.

[78] Michele Lazzeri et al. "Phonon linewidths and electron-phonon coupling in graphite and nanotubes". In: *Phys. Rev. B* 73 (15 Apr. 2006), p. 155426. DOI: 10.1103/PhysRevB.73.155426.

[79] H. Telg et al. "G– and G+ in the Raman spectrum of isolated nanotube: a study on resonance conditions and lineshape". In: *physica status solidi (b)* 245.10 (2008), pp. 2189–2192. DOI: https://doi.org/10.1002/pssb.200879658.

[80] P. T. Araujo et al. “Nature of the constant factor in the relation between radial breathing mode frequency and tube diameter for single-wall carbon nanotubes”. In: *Phys. Rev. B* 77 (24 June 2008), p. 241403. DOI: 10.1103/PhysRevB.77.241403.

[81] P. T. Araujo and A. Jorio. “The role of environmental effects on the optical transition energies and radial breathing mode frequency of single wall carbon nanotubes”. In: *physica status solidi (b)* 245.10 (2008), pp. 2201–2204. DOI: https://doi.org/10.1002/pssb.200879625.

[82] C. Fantini et al. “Optical Transition Energies for Carbon Nanotubes from Resonant Raman Spectroscopy: Environment and Temperature Effects”. In: *Phys. Rev. Lett.* 93 (14 Sept. 2004), p. 147406. DOI: 10.1103/PhysRevLett.93.147406.

[83] H. Telg et al. “Chirality Distribution and Transition Energies of Carbon Nanotubes”. In: *Phys. Rev. Lett.* 93 (17 Oct. 2004), p. 177401. DOI: 10.1103/PhysRevLett.93.177401.

[84] Kaihui Liu et al. “Intrinsic radial breathing oscillation in suspended single-walled carbon nanotubes”. In: *Phys. Rev. B* 83 (11 Mar. 2011), p. 113404. DOI: 10.1103/PhysRevB.83.113404.

[85] A. Jorio et al. “Structural (n, m) Determination of Isolated Single-Wall Carbon Nanotubes by Resonant Raman Scattering”. In: *Phys. Rev. Lett.* 86 (6 Feb. 2001), pp. 1118–1121. DOI: 10.1103/PhysRevLett.86.1118.

[86] A. G. Souza Filho et al. “Stokes and anti-Stokes Raman spectra of small-diameter isolated carbon nanotubes”. In: *Phys. Rev. B* 69 (11 Mar. 2004), p. 115428. DOI: 10.1103/PhysRevB.69.115428.

[87] M. Milnera et al. “Periodic Resonance Excitation and Intertube Interaction from Quasicontinuous Distributed Helicities in Single-Wall Carbon Nanotubes”. In: *Phys. Rev. Lett.* 84 (6 Feb. 2000), pp. 1324–1327. DOI: 10.1103/PhysRevLett.84.1324.

[88] Emmanuel Picheau et al. “Intense Raman D Band without Disorder in Flattened Carbon Nanotubes”. In: *ACS Nano* 15.1 (2021). PMID: 33444504, pp. 596–603. DOI: 10.1021/acsnano.0c06048.

[89] A. G. Souza Filho et al. “Effect of quantized electronic states on the dispersive Raman features in individual single-wall carbon nanotubes”. In: *Phys. Rev. B* 65 (3 Dec. 2001), p. 035404. DOI: 10.1103/PhysRevB.65.035404.

[90] A.G Souza Filho et al. “Probing the electronic trigonal warping effect in individual single-wall carbon nanotubes using phonon spectra”. In: *Chemical Physics Letters* 354.1 (2002), pp. 62–68. DOI: https://doi.org/10.1016/S0009-2614(02)00102-1.

[91] J. Kürti et al. “Double resonant Raman phenomena enhanced by van Hove singularities in single-wall carbon nanotubes”. In: *Phys. Rev. B* 65 (16 Apr. 2002), p. 165433. DOI: 10.1103/PhysRevB.65.165433.

[92] Duhee Yoon et al. “Interference effect on Raman spectrum of graphene on SiO_2/Si”. In: *Phys. Rev. B* 80 (12 Sept. 2009), p. 125422. DOI: 10.1103/PhysRevB.80.125422.

[93] Y. Y. Wang et al. “Interference enhancement of Raman signal of graphene”. In: *Applied Physics Letters* 92.4 (Jan. 2008). 043121. DOI: 10.1063/1.2838745.

[94] Jeroen W. G. Wilder et al. “Electronic structure of atomically resolved carbon nanotubes”. In: *Nature* 391.6662 (Jan. 1998), pp. 59–62. DOI: 10.1038/34139.

[95] E. H. Hwang, S. Adam, and S. Das Sarma. “Carrier Transport in Two-Dimensional Graphene Layers”. In: *Phys. Rev. Lett.* 98 (18 May 2007), p. 186806. DOI: 10.1103/PhysRevLett.98.186806.

[96] A. Hassanien and M. Tokumoto. “The electronic properties of suspended single wall carbon nanotubes”. In: *Carbon* 42.12 (2004), pp. 2649–2653. DOI: https://doi.org/10.1016/j.carbon.2004.06.009.

[97] Tae-Youl Choi et al. “Measurement of the Thermal Conductivity of Individual Carbon Nanotubes by the Four-Point Three-ω Method”. In: *Nano Letters* 6.8 (2006). PMID: 16895340, pp. 1589–1593. DOI: 10.1021/nl060331v.

[98] Jien Cao, Qian Wang, and Hongjie Dai. “Electron transport in very clean, as-grown suspended carbon nanotubes”. In: *Nature Materials* 4.10 (Oct. 2005), pp. 745–749. DOI: 10.1038/nmat1478.

[99] C. R. Dean et al. “Boron nitride substrates for high-quality graphene electronics”. In: *Nature Nanotechnology* 5.10 (Oct. 2010), pp. 722–726. DOI: 10.1038/nnano.2010.172.

[100] Alexander S. Mayorov et al. “Micrometer-Scale Ballistic Transport in Encapsulated Graphene at Room Temperature”. In: *Nano Letters* 11.6 (2011). PMID: 21574627, pp. 2396–2399. DOI: 10.1021/nl200758b.

[101] Kang Hyuck Lee et al. “Large-Scale Synthesis of High-Quality Hexagonal Boron Nitride Nanosheets for Large-Area Graphene Electronics”. In: *Nano Letters* 12.2 (2012). PMID: 22220633, pp. 714–718. DOI: 10.1021/nl203635v.

[102] Régis Decker et al. “Local Electronic Properties of Graphene on a BN Substrate via Scanning Tunneling Microscopy”. In: *Nano Letters* 11.6 (2011). PMID: 21553853, pp. 2291–2295. DOI: 10.1021/nl2005115.

[103] Mingyuan Huang et al. “Phonon softening and crystallographic orientation of strained graphene studied by Raman spectroscopy”. In: *Proceedings of the National Academy of Sciences* 106.18 (2009), pp. 7304–7308. DOI: 10.1073/pnas.0811754106.

[104] Bernard A. Weinstein and Richard Zallen. “Pressure-Raman effects in covalent and molecular solids”. In: *Light Scattering in Solids IV: Electronics Scattering, Spin Effects, SERS, and Morphic Effects*. Ed. by Manuel Cardona and Gernot Güntherodt. Berlin, Heidelberg: Springer Berlin Heidelberg, 1984, pp. 463–527. DOI: 10.1007/3-540-11942-6_26.

[105] Georgia Tsoukleri et al. "Subjecting a Graphene Monolayer to Tension and Compression". In: *Small* 5.21 (2009), pp. 2397–2402. DOI: https://doi.org/10.1002/smll.200900802.

[106] T. M. G. Mohiuddin et al. "Uniaxial strain in graphene by Raman spectroscopy: G peak splitting, Grüneisen parameters, and sample orientation". In: *Phys. Rev. B* 79 (20 May 2009), p. 205433. DOI: 10.1103/PhysRevB.79.205433.

[107] Haider I. Rasool et al. "Measurement of the intrinsic strength of crystalline and polycrystalline graphene". In: *Nature Communications* 4.1 (Nov. 2013), p. 2811. DOI: 10.1038/ncomms3811.

[108] J. Scott Bunch et al. "Impermeable Atomic Membranes from Graphene Sheets". In: *Nano Letters* 8.8 (2008). PMID: 18630972, pp. 2458–2462. DOI: 10.1021/nl801457b.

[109] Niklas Lindahl et al. "Determination of the Bending Rigidity of Graphene via Electrostatic Actuation of Buckled Membranes". In: *Nano Letters* 12.7 (2012). PMID: 22708530, pp. 3526–3531. DOI: 10.1021/nl301080v.

[110] A. Das et al. "Monitoring dopants by Raman scattering in an electrochemically top-gated graphene transistor". In: *Nature Nanotechnology* 3.4 (Apr. 2008), pp. 210–215. DOI: 10.1038/nnano.2008.67.

[111] S. Heinze et al. "Carbon Nanotubes as Schottky Barrier Transistors". In: *Phys. Rev. Lett.* 89 (10 Aug. 2002), p. 106801. DOI: 10.1103/PhysRevLett.89.106801.

[112] Max C Lemme et al. "A graphene field-effect device". In: *IEEE Electron Device Letters* 28.4 (2007), pp. 282–284.

[113] Yu-Ming Lin et al. "Operation of graphene transistors at gigahertz frequencies". In: *Nano letters* 9.1 (2009), pp. 422–426.

[114] Jun Yan et al. "Electric Field Effect Tuning of Electron-Phonon Coupling in Graphene". In: *Phys. Rev. Lett.* 98 (16 Apr. 2007), p. 166802. DOI: 10.1103/PhysRevLett.98.166802.

[115] Simone Pisana et al. "Breakdown of the adiabatic Born–Oppenheimer approximation in graphene". In: *Nature Materials* 6.3 (Mar. 2007), pp. 198–201. DOI: 10.1038/nmat1846.

[116] D. M. Basko, S. Piscanec, and A. C. Ferrari. "Electron-electron interactions and doping dependence of the two-phonon Raman intensity in graphene". In: *Phys. Rev. B* 80 (16 Oct. 2009), p. 165413. DOI: 10.1103/PhysRevB.80.165413.

[117] WeiJie Zhao et al. "Charge transfer and optical phonon mixing in few-layer graphene chemically doped with sulfuric acid". In: *Phys. Rev. B* 82 (24 Dec. 2010), p. 245423. DOI: 10.1103/PhysRevB.82.245423.

[118] C. A. Howard, M. P. M. Dean, and F. Withers. "Phonons in potassium-doped graphene: The effects of electron-phonon interactions, dimensionality, and adatom ordering". In: *Phys. Rev. B* 84 (24 Dec. 2011), p. 241404. DOI: 10.1103/PhysRevB.84.241404.

[119] Sunmin Ryu et al. "Atmospheric Oxygen Binding and Hole Doping in Deformed Graphene on a SiO2 Substrate". In: *Nano Letters* 10.12 (2010). PMID: 21069971, pp. 4944–4951. DOI: 10.1021/nl1029607.

[120] Jun Yan et al. "Observation of Anomalous Phonon Softening in Bilayer Graphene". In: *Phys. Rev. Lett.* 101 (13 Sept. 2008), p. 136804. DOI: 10.1103/PhysRevLett.101.136804.

[121] Michele Lazzeri and Francesco Mauri. "Nonadiabatic Kohn Anomaly in a Doped Graphene Monolayer". In: *Phys. Rev. Lett.* 97 (26 Dec. 2006), p. 266407. DOI: 10.1103/PhysRevLett.97.266407.

[122] Liu Zhenxian et al. "High-pressure Raman studies of graphite and ferric chloride-graphite". In: *Journal of Physics: Condensed Matter* 2.40 (Oct. 1990), p. 8083. DOI: 10.1088/0953-8984/2/40/008.

[123] K. Filintoglou et al. "Raman spectroscopy of graphene at high pressure: Effects of the substrate and the pressure transmitting media". In: *Phys. Rev. B* 88 (4 July 2013), p. 045418. DOI: 10.1103/PhysRevB.88.045418.

[124] Félix Balima. "Structure et porosité de systèmes lamellaires sous haute pression : cas du graphite et de la vermiculite". In: 2012.

[125] Feng Ke et al. "Synthesis of Atomically Thin Hexagonal Diamond with Compression". In: *Nano Letters* 20.8 (2020). PMID: 32578991, pp. 5916–5921. DOI: 10.1021/acs.nanolett.0c01872.

[126] Luiz G. Pimenta Martins et al. "Hard, transparent, sp3-containing 2D phase formed from few-layer graphene under compression". In: *Carbon* 173 (2021), pp. 744–757. DOI: https://doi.org/10.1016/j.carbon.2020.11.038.

[127] Paul Loubeyre, Florent Occelli, and René LeToullec. "Optical studies of solid hydrogen to 320 GPa and evidence for black hydrogen". In: *Nature* 416.6881 (Apr. 2002), pp. 613–617. DOI: 10.1038/416613a.

[128] Ranga P. Dias and Isaac F. Silvera. "Observation of the Wigner-Huntington transition to metallic hydrogen". In: *Science* 355.6326 (2017), pp. 715–718. DOI: 10.1126/science.aal1579.

[129] Zs. Jenei et al. "Single crystal toroidal diamond anvils for high pressure experiments beyond 5 megabar". In: *Nature Communications* 9.1 (Sept. 2018), p. 3563. DOI: 10.1038/s41467-018-06071-x.

[130] D. J. Dunstan. "Theory of the gasket in diamond anvil high-pressure cells". In: *Review of Scientific Instruments* 60.12 (Dec. 1989), pp. 3789–3795. DOI: 10.1063/1.1140442.

[131] Akobuije D. Chijioke et al. "The ruby pressure standard to 150GPa". In: *Journal of Applied Physics* 98.11 (Dec. 2005). 114905. DOI: 10.1063/1.2135877.

[132] Robert F Cook and Chris A Michaels. "Review: Coefficients for Stress, Temperature, and Composition Effects in Fluorescence Measurements of Alumina". en. In: *J Res Natl Inst Stand Technol* 122 (Dec. 2017), pp. 1–26.

[133] S Klotz et al. "Hydrostatic limits of 11 pressure transmitting media". In: *Journal of Physics D: Applied Physics* 42.7 (Mar. 2009), p. 075413. DOI: `10.1088/0022-3727/42/7/075413`.

[134] GJ Piermarini, S Block, and JD Barnett. "Hydrostatic limits in liquids and solids to 100 kbar". In: *Journal of Applied Physics* 44.12 (1973), pp. 5377–5382.

[135] Charles Kittel. *Introduction to Solid State Physics*. 8th ed. Wiley, 2004.

[136] Ji-an Xu and Eugene Huang. "Graphite-diamond transition in gem anvil cells". In: *Review of Scientific Instruments* 65.1 (Jan. 1994), pp. 204–207. DOI: `10.1063/1.1144779`.

[137] Katsuhisa Furuno, Akifumi Onodera, and Shoichi Kume. "Sapphire-Anvil Cell for High Pressure Research". In: *Japanese Journal of Applied Physics* 25.8A (Aug. 1986), p. L646. DOI: `10.1143/JJAP.25.L646`.

[138] Ji-an Xu, Ho-kwang Mao, and Russell J Hemley. "The gem anvil cell: high-pressure behaviour of diamond and related materials". In: *Journal of Physics: Condensed Matter* 14.44 (Oct. 2002), p. 11549. DOI: `10.1088/0953-8984/14/44/514`.

[139] Ji-An Xu et al. "Ultrahigh pressures in gem anvil cells". In: *High Pressure Research* 15.2 (1996), pp. 127–134. DOI: `10.1080/08957959608240466`.

[140] Ian L. Spain and David J. Dunstan. "The technology of diamond anvil high-pressure cells. II: Operation and use". In: *Journal of Physics E: Scientific Instruments* 22 (1989), pp. 923–933.

[141] R. Bouaita et al. "Seed orientation and pulling rate effects on bubbles and strain distribution on a sapphire crystal grown by the micro-pulling down method". In: *CrystEngComm* 21 (28 2019), pp. 4200–4211. DOI: `10.1039/C9CE00510B`.

[142] A. Jafari et al. "Rocking curve imaging of high quality sapphire crystals in backscattering geometry". In: *Journal of Applied Physics* 121.4 (Jan. 2017). 044901. DOI: `10.1063/1.4974106`.

[143] Linlin Cao et al. "Study on the Influence of Sapphire Crystal Orientation on Its Chemical Mechanical Polishing". In: *Applied Sciences* 10.22 (2020). DOI: `10.3390/app10228065`.

[144] Douglas Murphy et al. "Principles of Birefringence". In: ().

[145] I. A. Cherepanov, A. S. Savinykh, and S. V. Razorenov. "Spalling in Sapphire in Different Crystallographic Directions under Shock Compression". In: *Technical Physics* 65.6 (June 2020), pp. 921–924. DOI: `10.1134/S1063784220060067`.

[146] WD Nesse. "Introduction to Optical Mineralogy, OUP". In: (1991).

[147] Masahiro Nakajima, Pou Liu, and Toshio Fukuda. "Nanomanipulation and Nanoassembly of Carbon Nanotubes Inside Electron Microscopes". In: *IFAC Proceedings Volumes* 41.2 (2008). 17th IFAC World Congress, pp. 13743–13748. DOI: `https://doi.org/10.3182/20080706-5-KR-1001.02327`.

[148] Daisuke Takagi, Yoshikazu Homma, and Yoshihiro Kobayashi. "Selective growth of individual single-walled carbon nanotubes suspended between pillar structures". In: *Physica E: Low-dimensional Systems and Nanostructures* 24.1 (2004). Proceedings of the International Symposium on Functional Semicond uctor Nanostructures 2003, pp. 1–5. DOI: `https://doi.org/10.1016/j.physe.2004.04.013`.

[149] Rajdip Bandyopadhyaya et al. "Stabilization of Individual Carbon Nanotubes in Aqueous Solutions". In: *Nano Letters* 2.1 (2002), pp. 25–28. DOI: `10.1021/nl010065f`.

[150] Andres Castellanos-Gomez et al. "Deterministic transfer of two-dimensional materials by all-dry viscoelastic stamping". In: *2D Materials* 1.1 (Apr. 2014), p. 011002. DOI: `10.1088/2053-1583/1/1/011002`.

[151] Filippo Pizzocchero et al. "The hot pick-up technique for batch assembly of van der Waals heterostructures". In: *Nature Communications* 7.1 (June 2016), p. 11894. DOI: `10.1038/ncomms11894`.

[152] Alexis Forestier. "Physical Response of Graphene Layers at Extreme Pressure". Theses. Université de Lyon, Dec. 2020.

[153] Thomas W. Tombler et al. "Gating individual nanotubes and crosses with scanning probes". In: *Applied Physics Letters* 76.17 (Apr. 2000), pp. 2412–2414. DOI: `10.1063/1.125611`.

[154] Awnish K Gupta et al. "Curvature-induced D-band Raman scattering in folded graphene*". In: *Journal of Physics: Condensed Matter* 22.33 (Aug. 2010), p. 334205. DOI: `10.1088/0953-8984/22/33/334205`.

[155] A. Picard et al. "In situ monitoring by quantitative Raman spectroscopy of alcoholic fermentation by Saccharomyces cerevisiae under high pressure". In: *Extremophiles* 11.3 (May 2007), pp. 445–452. DOI: `10.1007/s00792-006-0054-x`.

[156] M. A. Pimenta et al. "Diameter dependence of the Raman D-band in isolated single-wall carbon nanotubes". In: *Phys. Rev. B* 64 (4 June 2001), p. 041401. DOI: `10.1103/PhysRevB.64.041401`.

[157] Chandrani Pramanik et al. "Carbon Nanotube Dispersion in Solvents and Polymer Solutions: Mechanisms, Assembly, and Preferences". In: *ACS Nano* 11.12 (2017). PMID: 29179536, pp. 12805–12816. DOI: `10.1021/acsnano.7b07684`.

[158] Liu Yang and Jie Han. "Electronic Structure of Deformed Carbon Nanotubes". In: *Phys. Rev. Lett.* 85 (1 July 2000), pp. 154–157. DOI: `10.1103/PhysRevLett.85.154`.

[159] James A. Elliott et al. “Collapse of Single-Wall Carbon Nanotubes is Diameter Dependent”. In: *Phys. Rev. Lett.* 92 (9 Mar. 2004), p. 095501. DOI: `10.1103/PhysRevLett.92.095501`.

[160] J. -C. Charlier, Ph. Lambin, and T. W. Ebbesen. “Electronic properties of carbon nanotubes with polygonized cross sections”. In: *Phys. Rev. B* 54 (12 Sept. 1996), R8377–R8380. DOI: `10.1103/PhysRevB.54.R8377`.

[161] Ado Jorio and Luiz Gustavo Cançado. “Raman spectroscopy of twisted bilayer graphene”. In: *Solid State Communications* 175-176 (2013). Special Issue: Graphene V: Recent Advances in Studies of Graphene and Graphene analogues, pp. 3–12. DOI: `https://doi.org/10.1016/j.ssc.2013.08.008`.

[162] Jing-Yin Chen et al. “Time-resolved x-ray diffraction across water-ice-VI/VII transformations using the dynamic-DAC”. In: *Journal of Physics: Conference Series* 500.14 (May 2014), p. 142006. DOI: `10.1088/1742-6596/500/14/142006`.

[163] Zachary M. Grande et al. “Pressure-driven symmetry transitions in dense H_2O ice”. In: *Phys. Rev. B* 105 (10 Mar. 2022), p. 104109. DOI: `10.1103/PhysRevB.105.104109`.

[164] Yang Gao et al. “Ultrahard carbon film from epitaxial two-layer graphene”. In: *Nature Nanotechnology* 13.2 (Feb. 2018), pp. 133–138. DOI: `10.1038/s41565-017-0023-9`.

[165] Leonid A. Chernozatonskii et al. “Influence of Size Effect on the Electronic and Elastic Properties of Diamond Films with Nanometer Thickness”. In: *The Journal of Physical Chemistry C* 115.1 (2011), pp. 132–136. DOI: `10.1021/jp1080687`.

[166] Ana P. M. Barboza et al. “Room-Temperature Compression-Induced Diamondization of Few-Layer Graphene”. In: *Advanced Materials* 23.27 (2011), pp. 3014–3017. DOI: `https://doi.org/10.1002/adma.201101061`.

[167] O. Leenaerts, B. Partoens, and F. M. Peeters. “Hydrogenation of bilayer graphene and the formation of bilayer graphane from first principles”. In: *Phys. Rev. B* 80 (24 Dec. 2009), p. 245422. DOI: `10.1103/PhysRevB.80.245422`.

[168] A. G. Kvashnin et al. “Features of Electronic, Mechanical, and Electromechanical Properties of Fluorinated Diamond Films of Nanometer Thickness”. In: *The Journal of Physical Chemistry C* 121.51 (2017), pp. 28484–28489. DOI: `10.1021/acs.jpcc.7b07946`.

[169] Maximilian Amsler et al. “Crystal Structure of Cold Compressed Graphite”. In: *Phys. Rev. Lett.* 108 (6 Feb. 2012), p. 065501. DOI: `10.1103/PhysRevLett.108.065501`.

[170] AF Goncharov, IN Makarenko, and SM Stishov. “Graphite at pressure up to 55 GPa: optical properties and Raman scattering-amorphous carbon”. In: *Sov. Phys. JETP* 69.2 (1989), pp. 380–381.

[171] Wataru Utsumi and Takehiko Yagi. “Light-Transparent Phase Formed by Room-Temperature Compression of Graphite”. In: *Science* 252.5012 (1991), pp. 1542–1544. DOI: `10.1126/science.252.5012.1542`.

[172] John Taylor. *Introduction to error analysis, the study of uncertainties in physical measurements*. 1997.

[173] Liubov Yu. Antipina and Pavel B. Sorokin. “Converting Chemically Functionalized Few-Layer Graphene to Diamond Films: A Computational Study”. In: *The Journal of Physical Chemistry C* 119.5 (2015), pp. 2828–2836. DOI: `10.1021/jp510390b`.

[174] Yevhen Horbatenko et al. “Synergetic interplay between pressure and surface chemistry for the conversion of sp2-bonded carbon layers into sp3-bonded carbon films”. In: *Carbon* 106 (2016), pp. 158–163. DOI: `https://doi.org/10.1016/j.carbon.2016.05.012`.

[175] Masakazu Matsumoto, Takuma Yagasaki, and Hideki Tanaka. “GenIce: Hydrogen-Disordered Ice Generator”. In: *Journal of Computational Chemistry* 39.1 (2018), pp. 61–64. DOI: `https://doi.org/10.1002/jcc.25077`.

[176] G. E. Walrafen et al. “Raman and x-ray investigations of ice VII to 36.0 GPa”. In: *The Journal of Chemical Physics* 77.4 (Aug. 1982), pp. 2166–2174. DOI: `10.1063/1.444023`.

[177] Ph Pruzan, J. C. Chervin, and M. Gauthier. “Raman Spectroscopy Investigation of Ice VII and Deuterated Ice VII to 40 GPa. Disorder in Ice VII”. In: *Europhysics Letters* 13.1 (Sept. 1990), p. 81. DOI: `10.1209/0295-5075/13/1/014`.

[178] Romain Chambard et al. “Tuning of photoluminescence intensity and Fermi level position of individual single-walled carbon nanotubes by molecule confinement”. In: *Carbon* 186 (2022), pp. 423–430. DOI: `https://doi.org/10.1016/j.carbon.2021.09.072`.

[179] Hyeon Jun Hwang et al. “Large scale graphene thermoelectric device with high power factor using gradient doping profile”. In: *Carbon* 201 (2023), pp. 467–472. DOI: `https://doi.org/10.1016/j.carbon.2022.09.048`.

[180] A Gumprich et al. “Buried graphene heterostructures for electrostatic doping of low-dimensional materials”. In: *Nanotechnology* 34.26 (Apr. 2023), p. 265203. DOI: `10.1088/1361-6528/acbaa2`.

[181] Zegao Wang et al. “Investigating the stability of molecule doped graphene field effect transistors”. In: *New J. Chem.* 43 (38 2019), pp. 15275–15279. DOI: `10.1039/C9NJ03537K`.

[182] Filippo Cellini et al. “Pressure-Induced Formation and Mechanical Properties of 2D Diamond Boron Nitride”. In: *Advanced Science* 8.2 (2021), p. 2002541. DOI: `https://doi.org/10.1002/advs.202002541`.

[183] Ana P. M. Barboza et al. “Compression-Induced Modification of Boron Nitride Layers: A Conductive Two-Dimensional BN Compound”. In: *ACS Nano* 12.6 (2018). PMID: 29787237, pp. 5866–5872. DOI: `10.1021/acsnano.8b01911`.

[184] Zhen-Hua Chi et al. "Pressure-Induced Metallization of Molybdenum Disulfide". In: *Phys. Rev. Lett.* 113 (3 July 2014), p. 036802. DOI: 10.1103/PhysRevLett.113.036802.

[185] Ana P.M. Barboza et al. "Graphene/h-BN heterostructures under pressure: From van der Waals to covalent". In: *Carbon* 155 (2019), pp. 108–113. DOI: https://doi.org/10.1016/j.carbon.2019.08.054.

[186] Samar Layek et al. "Possible high temperature superconducting transitions in disordered graphite obtained from room temperature deintercalated KC8". In: *Carbon* 201 (2023), pp. 667–678. DOI: https://doi.org/10.1016/j.carbon.2022.09.041.

[187] Chao Zhang et al. "Stable and Metastable Structures in Compressed LiC6: Dimensional Diversity". In: *The Journal of Physical Chemistry C* 120.19 (2016), pp. 10137–10145. DOI: 10.1021/acs.jpcc.6b01206.

[188] Jon H. Eggert et al. "High pressure refractive index measurements of 4:1 methanol:ethanol". In: *Journal of Applied Physics* 72.6 (Sept. 1992), pp. 2453–2461. DOI: 10.1063/1.351591.

[189] F. Decremps et al. "Equation of state, stability, anisotropy and nonlinear elasticity of diamond-cubic (ZB) silicon by phonon imaging at high pressure". In: *Phys. Rev. B* 82 (10 Sept. 2010), p. 104119. DOI: 10.1103/PhysRevB.82.104119.

[190] Duhee Yoon, Young-Woo Son, and Hyeonsik Cheong. "Negative Thermal Expansion Coefficient of Graphene Measured by Raman Spectroscopy". In: *Nano Letters* 11.8 (2011). PMID: 21728349, pp. 3227–3231. DOI: 10.1021/nl201488g.

[191] Tao Jiang et al. "Equi-biaxial compressive strain in graphene: Grüneisen parameter and buckling ridges". In: *2D Materials* 6.1 (Dec. 2018), p. 015026. DOI: 10.1088/2053-1583/aaf20a.

[192] Charalampos Androulidakis et al. "Failure Processes in Embedded Monolayer Graphene under Axial Compression". In: *Scientific Reports* 4.1 (June 2014), p. 5271. DOI: 10.1038/srep05271.

[193] Elsebeth Schröder. "Methanol Adsorption on Graphene". In: *Journal of Nanomaterials* 2013 (Sept. 2013), p. 871706. DOI: 10.1155/2013/871706.

[194] A. S. Bolina, A. J. Wolff, and W. A. Brown. "Reflection absorption infrared spectroscopy and temperature programmed desorption investigations of the interaction of methanol with a graphite surface". In: *The Journal of Chemical Physics* 122.4 (Jan. 2005). 044713. DOI: 10.1063/1.1839554.

[195] K. Zhang and M. Arroyo. "Adhesion and friction control localized folding in supported graphene". In: *Journal of Applied Physics* 113.19 (May 2013). 193501. DOI: 10.1063/1.4804265.

[196] Basile Audoly. "Stability of Straight Delamination Blisters". In: *Phys. Rev. Lett.* 83 (20 Nov. 1999), pp. 4124–4127. DOI: 10.1103/PhysRevLett.83.4124.

[197] Dominic Vella et al. “The macroscopic delamination of thin films from elastic substrates”. In: *Proceedings of the National Academy of Sciences* 106.27 (2009), pp. 10901–10906. DOI: 10.1073/pnas.0902160106.

[198] Guorui Wang et al. “Bending of Multilayer van der Waals Materials”. In: *Phys. Rev. Lett.* 123 (11 Sept. 2019), p. 116101. DOI: 10.1103/PhysRevLett.123.116101.

[199] Lei Gong et al. “Reversible Loss of Bernal Stacking during the Deformation of Few-Layer Graphene in Nanocomposites”. In: *ACS Nano* 7.8 (2013). PMID: 23899378, pp. 7287–7294. DOI: 10.1021/nn402830f.

[200] Steven P. Koenig et al. “Ultrastrong adhesion of graphene membranes”. In: *Nature Nanotechnology* 6.9 (Sept. 2011), pp. 543–546. DOI: 10.1038/nnano.2011.123.

[201] Sumin Kang et al. “Liquid-assisted adhesion control of graphene–copper interface for damage-free mechanical transfer”. In: *Applied Surface Science* 551 (2021), p. 149229. DOI: https://doi.org/10.1016/j.apsusc.2021.149229.

[202] Philippe Lambin. “Elastic Properties and Stability of Physisorbed Graphene”. In: *Applied Sciences* 4.2 (2014), pp. 282–304. DOI: 10.3390/app4020282.

[203] Banafsheh Sajadi et al. “Size- and temperature-dependent bending rigidity of graphene using modal analysis”. In: *Carbon* 139 (2018), pp. 334–341. DOI: https://doi.org/10.1016/j.carbon.2018.06.066.

[204] Guilhermino J.M. Fechine et al. “Direct dry transfer of chemical vapor deposition graphene to polymeric substrates”. In: *Carbon* 83 (2015), pp. 224–231. DOI: https://doi.org/10.1016/j.carbon.2014.11.038.

[205] Wenzheng Zhai et al. “Carbon nanomaterials in tribology”. In: *Carbon* 119 (2017), pp. 150–171. DOI: https://doi.org/10.1016/j.carbon.2017.04.027.

[206] Florian Pape and Gerhard Poll. “Investigations on Graphene Platelets as Dry Lubricant and as Grease Additive for Sliding Contacts and Rolling Bearing Application”. In: *Lubricants* 8.1 (2020). DOI: 10.3390/lubricants8010003.

[207] O. V. Sedelnikova, L. G. Bulusheva, and A. V. Okotrub. “Curvature-Induced Optical Transitions in Graphene”. In: *Fullerenes, Nanotubes and Carbon Nanostructures* 20.4-7 (2012), pp. 558–562. DOI: 10.1080/1536383X.2012.656486.

[208] Julia Sabalot-Cuzzubbo et al. “Relating the molecular topology and local geometry: Haddon’s pyramidalization angle and the Gaussian curvature”. In: *The Journal of Chemical Physics* 152.24 (June 2020). 244310. DOI: 10.1063/5.0008368.

Abstract: The extraordinary properties of low dimensional systems opened up opportunities for the development of novel technologies due to their excellent mechanical, electrical and optical properties. Moreover, their low-dimensional nature intrinsically connects them to the surrounding environment which can be used to tune their properties.

In the present work we investigated the role of pressure as a thermodynamic tuning variable for enhancing sample-environment interaction. We focussed principally on graphene and its stacking, and carbon nanotubes. Several instrumental developments have been necessary for those studies which resulted in the improvement of a transfer system for 2D materials, in the development of a spectroscopic mapping system and an upgraded system for high pressure application using sapphire anvils.

Using those technologies we studied, in an initial part of this work, new pathways to detect and characterize the collapse of carbon nanotubes at high pressure. We used the Raman D-band of carbon nanotubes as a novel spectroscopic signature of their collapse to a flattened shape, allowing us to detect their geometrical changes when surrounded by different environments. Furthermore, we focussed on the study of individualized tubes and follow the evolution of an individualized 1.68 nm diameter tube, characterizing the signatures of its collapse by its optical and vibrational properties.

In a second part of the work we focussed on the study of graphene and few-layer graphene by investigating the role of the environment surrounding two-dimensional systems in high pressure experiments. The interaction with the underlying substrate was thoroughly explored by fabricating suspending structures for two-dimensional systems adapted for high pressure. We found excellent mechanical strain and charge carrier transmission between the supported and suspended regions of the sample in bilayer graphene. Using thin graphites our results show that the pressure response of the sample is affected by the geometry of the suspension and an improved chemical interaction with the environment in the suspended region. Additionally, we studied the effects of water on the high pressure transition of few-layer graphene to diamondene by creating a heterostructure graphene/hBN as well as by interchanging different substrates. We found that, together with the chemical interaction with water, the biaxial strain induced by the substrate on the sample is an essential tuning parameter for the transition, opening up opportunities for novel ways of fabricating diamondene at high pressure.

Keywords: Graphene, nanotubes, high pressure, environment, Raman spectroscopy